Measurement Notes
Note 48
December 1996

Measurement Methods and the Characterization of the Electromagnetic Properties of Materials

Clifton Courtney and William Motil
Voss Scientific

Tracey Bowen and Sydney Blocher
Phillips Laboratory

Abstract

Accurate knowledge of material complex relative permittivity ($\varepsilon_r = \varepsilon_r' + j\varepsilon_r''$) and permeability ($\mu_r = \mu_r' + j\mu_r''$) is required for many applications including the design of radar-absorbing material and RAM geometries, design of transmission line circuits on microwave substrates, and simulation and analysis of the propagation of electromagnetic waves in and through complex media. The measurement of material relative permittivity (ε_r) and permeability (μ_r) can be accomplished in a number of ways. These include balanced bridge methods at low frequencies, transmission line and resonant cavity methods for high frequencies, and optical techniques. These approaches typically are conducted at low voltage and electric field strengths, and assume that the materials are homogeneous and their properties are independent of the field strength.

This subtask has explored several methods to determine the electromagnetic properties of materials, and in particular, the properties of slightly non-homogeneous materials, and materials with large cross sections. This report recounts the progress made, and the measurement techniques investigated under this effort. These include: (1) time domain; (2) frequency domain; and (3) in-situ material characterization methods. In this report, we first review the need for this effort, present some basic background theory on electromagnetic wave propagation

in media, then describe the manner in which material parameters can be determined from physical measurements. Next we discuss the time domain measurement technique, then describe frequency domain methods. The frequency domain methods to determine permittivity and permeability include: transmission and reflection measurements; reflection measurements only (with a short circuit terminating the line); and a description of an "in-situ" measurement technique to find dielectric properties of materials in-place. Also included is a discussion of the hardware and measurement procedures utilized in this effort, and a presentation of the results of material electromagnetic properties determined using the techniques discussed previously.

To summarize the results, we note the following. The ability to measure both homogeneous and non-homogeneous materials, in large cross-sectional geometries has been demonstrated using several methods. The time domain method yields good results even out to 8 GHz. However, the sample sizes need to be large enough to provide the required time isolation. The short-circuit frequency-domain method also gave good results - above 100 MHz out to about 5 GHz. The low frequency results were limited by the sample size (E-field must be zero at the short). The transmission-reflection measurements had no low-frequency limitation, and worked better for smaller samples. But the need to carefully relate the transmission and reflection measurements to each other limited the usefulness of this method. Finally, the in-situ technique was only explored in a limited way. Preliminary measurements indicate that the reflection (or admittance) measurement is extremely sensitive, and may prove tenuous.

Table of Contents

I. Introduction

Accurate knowledge of material complex relative permittivity ($\varepsilon_r = \varepsilon_r' + j\varepsilon_r''$) and permeability ($\mu_r = \mu_r' + j\mu_r''$) is required for just about any application utilizing the electromagnetic properties of materials. Applications that need precise information of the frequency dependence of ε_r and μ_r include design of radar absorbing material and RAM geometry, design of transmission line circuits on microwave substrates, and simulation and analysis of the propagation of electromagnetic waves in and through complex media. Frequency domain measurement of material properties are well known, and can be accomplished in a number of ways. These include lumped circuit and balanced bridge methods at low frequencies, and waveguide, TEM transmission line and resonant cavity methods for high frequencies [Ref. 1, 2], and optical techniques. A comprehensive overview of material electromagnetic properties measurement techniques can be found in the paper of Afsar, et al. [Ref. 3]. These techniques typically are conducted at low voltage and low electric field strengths, and assume the material properties are independent of the field strength.

However, many the techniques utilized prior have assumed the material under test is homogeneous, and can be fabricated in a small cross section. Recently, the need has arose to characterize materials that are slightly non-homogeneous, and impossible to fabricate into small samples. These include: concrete, mixed media such as found in walls, soil, liquids, and other building supplies. This effort has explored measurement techniques suitable for these types of materials. These techniques include time domain, frequency domain, and in-situ methods.

In the late 60's and early 70's, before the advent of the automatic network analyzer, time domain methods became popular [Ref. 4, 5]. These techniques utilized the spectral content of a fast rise time pulse to determine the frequency dependence of the complex ε_r and μ_r of materials. However, the method described in Ref. 4 relied on approximations, which may not be valid for some cases of interest. The time domain measurement procedure discussed here is unique in two ways. First, though the time domain scheme employed here is based on previously described methods, the hardware design and data reduction techniques used eliminate some of the approximations and sources of potential error of the earlier work.

Next, we describe several frequency domain measurement methods that make use of the power of a network analyzer. First, a technique that uses both transmission and reflection measurements is described. Next, the determination of dielectric material constant from just a reflection measurement is derived.

The report is organized as follows. In the next section the theory of TEM propagation in a transmission line is given, and an introduction of the terminology and notation used in this work. Next, we discuss the time domain measurement technique, and how we determine the frequency dependent material properties from time domain

measurements. Data reduction methods are described, and the reduction of measurements to material parameters is given. Next, frequency domain methods to determine permittivity and permeability are described. These include: transmission and reflection measurements; and reflection measurements only (with a short circuit terminating the line). Following is a description of the hardware set, and a discussion of timing considerations important to the design. In the subsequent section is found the results of measurements taken to characterize the frequency dependence of the complex ε_r and μ_r. This includes the results of both time and frequency domain measurements. Finally, we describe an "in-situ" measurement technique to find dielectric properties of materials in-place.

II. Background: Theory and Reduction of Measured Parameters to Material Electromagnetic Parameters

This section presents a brief review of the theory of TEM propagation in region with two materials, derives the relationship between the time harmonic transmission and reflection coefficients (or scattering parameters s_{21} and s_{11}) and measured transient waveforms, and describes the extraction of the complex ε_r and μ_r material parameters from these same measured transient waveforms.

II.1. Time Harmonic TEM Propagation in a Two-Media Region

Consider the situation depicted in Figure 1a. There, a TEM wave is shown incident on an interface between Region 1 characterized by (ε_0, μ_0) and Region 2 characterized by (ε_2, μ_2). The normal to the interface between semi-infinite Regions 1 and 2 is opposite to the direction of the incident wave, and the thickness of Region 2 is l; the coordinate convention is also indicated in the figure. A second interface between Regions 2 and 3, characterized as well by (ε_0, μ_0), is also indicated. The wave interactions of the coaxial transmission line shown in Figure 1b can model the characteristics of the geometry of Figure 1a. Note the transit times and observation positions indicated. For observation locations in Regions 1 and 3 the waveforms of interest include $\mathbf{E}^{\mathbf{inc}}$ (assumed known), $\mathbf{E}^{\mathbf{ref}}$ = the total reflected waveform in Region 1, and $\mathbf{E}^{\mathbf{tran}}$ = the total transmitted waveform in Region 3. The usual microwave s-parameters can be written for time-harmonic excitation as

$$s_{11}(\omega) = \frac{\mathbf{E}^{\mathbf{ref}}}{\mathbf{E}^{\mathbf{inc}}}, \quad \text{and} \quad s_{21}(\omega) = \frac{\mathbf{E}^{\mathbf{tran}}}{\mathbf{E}^{\mathbf{inc}}}. \tag{II.1}$$

In terms of the wave impedances of each region the above can be written as

$$s_{11}(\omega) = \frac{\left(Z_2^2 - Z_0^2\right)\cdot\left(1 - e^{-j2\beta_2 l}\right)}{\left(Z_2 + Z_0\right)^2 - \left(Z_2 - Z_0\right)^2 \cdot e^{-j2\beta_2 l}}, \tag{II.2a}$$

and

$$s_{21}(\omega) = \frac{4\left(Z_0 Z_2\right)\cdot e^{-j\beta_2 l}}{\left(Z_2 + Z_0\right)^2 - \left(Z_2 - Z_0\right)^2 \cdot e^{-j2\beta_2 l}}. \tag{II.3b}$$

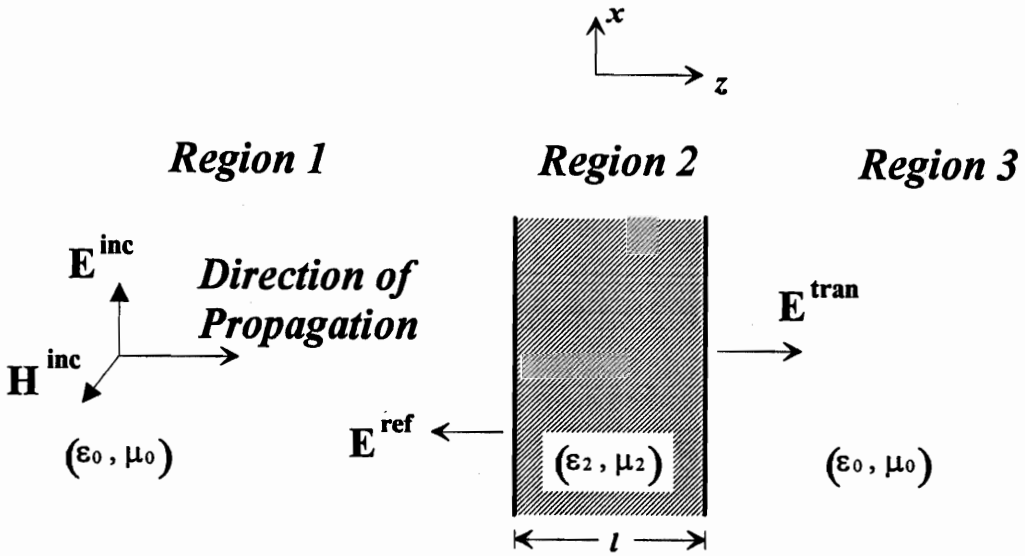

(a)

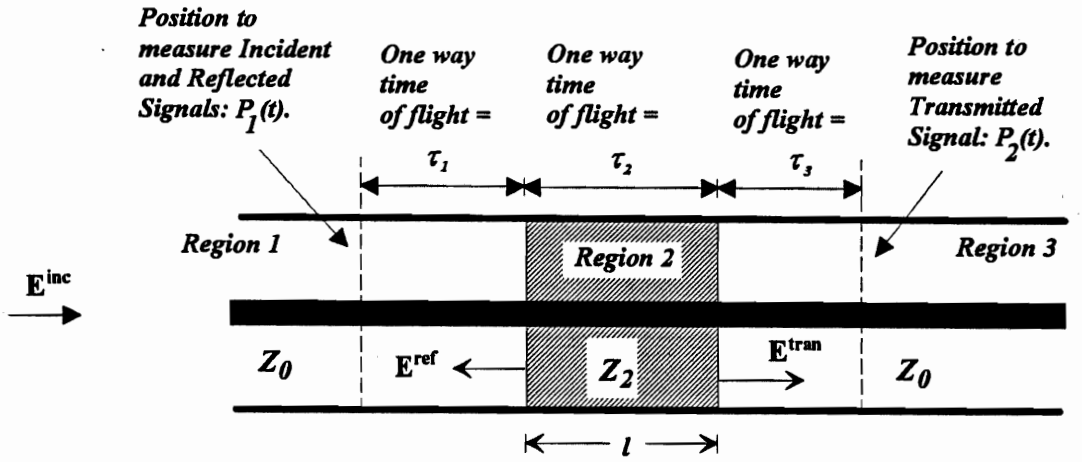

(b)

Figure 1. **Geometry of interest: (a) a TEM wave is incident on the interface of Region 1 characterized by (ε_0, μ_0) and Region 2 characterized by (ε_2, μ_2); and (b) a coaxial transmission line can be used to model the geometry of (a).**

In the above [Ref. 6]: $\varepsilon_2 = \varepsilon_0 \cdot (\varepsilon'_{r2} + j\varepsilon''_{r2})$; $\mu_2 = \mu_0 \cdot (\mu'_{r2} + j\mu''_{r2})$; $Z_0 = \sqrt{\mu_0 / \varepsilon_0}$;

$Z_2 = \sqrt{\mu_2 / \varepsilon_2}$; and $\beta_2 = \dfrac{\omega\sqrt{\varepsilon_{r2} \cdot \mu_{r2}}}{c_0}$, where c_0 = speed of light in vacuum. Note that II.2a and II.2b assume the evaluation is at the interface between Regions 1 and 2, and 2 and 3 respectively. Evaluation positions at other locations in Regions 1 and 3 require modification of the expressions by an appropriate amount of phase shift corresponding to propagation in Regions 1 and 3.

II.2. Frequency Dependent Material Properties from Knowledge of s_{11} and s_{12}

Given knowledge of the s-parameters s_{11} and s_{12} associated with a specific material, measured in a coaxial fixture similar to that shown in Figure 1b, then the material properties ε_r and μ_r can be determined. A procedure for extracting the values is given below, it follows the algorithm presented by Nicolson and Ross [Ref. 4], and summarized by Lederer [Ref. 7].

Eqns. II.2a and II.2b can be rewritten in more compact and convenient forms as

$$s_{11}(\omega) = \frac{(1 - z^2) \cdot \Gamma_{12}}{1 - \Gamma_{12}^2 \cdot z^2}, \tag{II.3a}$$

and

$$s_{21}(\omega) = \frac{(1 - \Gamma_{12}^2) \cdot z}{1 - \Gamma_{12}^2 \cdot z^2}; \tag{II.3b}$$

where $\Gamma_{ab} = \dfrac{Z_b - Z_a}{Z_b + Z_a}$ = the reflection coefficient for a wave passing from the semi-infinite Region a into the semi-infinite Region b, and $z = e^{-j\beta_2 l}$. Then, it can be shown that the following relations hold

$$\Gamma_{12} = X \pm \sqrt{X^2 - 1}. \tag{II.4a}$$

and

$$z = \frac{s_{11} + s_{21} - \Gamma_{12}}{1 - (s_{11} + s_{21}) \cdot \Gamma_{12}} \tag{II.4b}$$

where X is expressed in terms of the scattering parameters as

$$X = \frac{1-(s_{21}^2 - s_{11}^2)}{2s_{11}} \pm \sqrt{\left[\frac{1-(s_{21}^2 - s_{11}^2)}{2s_{11}}\right]^2 - 1}\,. \qquad \text{(II.4c)}$$

Now recall from above $z = e^{-j\beta_2 l} = e^{-j(\omega/c_0)\cdot\sqrt{\mu_{r2}\varepsilon_{r2}}}$; taking logarithms of both sides yields [Ref. 8]

$$\begin{aligned} \ln(z) &= \mathrm{Ln}|z| + j\arg(z) \\ &= \mathrm{Ln}\left|e^{-j(\omega/c_0)\cdot\sqrt{\mu_{r2}\varepsilon_{r2}}}\right| + j\arg\left(e^{-j(\omega/c_0)\cdot\sqrt{\mu_{r2}\varepsilon_{r2}}}\right). \end{aligned} \qquad \text{(II.5)}$$

If we assume that Region 2 is not too lossy, then

$$|z| = \left|e^{-j(\omega/c_0)\cdot\sqrt{\mu_{r2}\varepsilon_{r2}}}\right| \approx 1, \qquad \text{(II.6)}$$

and

$$\ln(z) = 0 - j(\omega/c_0)\cdot\sqrt{\mu_{r2}\varepsilon_{r2}}\,. \qquad \text{(II.7)}$$

The product of the material parameters then is

$$\mu_{r2}\varepsilon_{r2} = -\left\{\left(\frac{c_0}{l\cdot\omega}\right)\cdot\ln(z)\right\}^2 = C_1\,. \qquad \text{(II.8)}$$

Furthermore, $\Gamma_{12} = \dfrac{Z_2 - Z_1}{Z_2 + Z_1} = \dfrac{\sqrt{\mu_{r2}/\varepsilon_{r2}} - 1}{\sqrt{\mu_{r2}/\varepsilon_{r2}} + 1}$, and solving for the ratio of $\mu_{r2}/\varepsilon_{r2}$ yields

$$\frac{\mu_{r2}}{\varepsilon_{r2}} = \left(\frac{1+\Gamma_{12}}{1-\Gamma_{12}}\right)^2 = C_2\,. \qquad \text{(II.9)}$$

With the relations expressed in Eqns. II.8 and II.9, the material parameters can be separated as

$$\mu_{r2} = \sqrt{C_1\cdot C_2}\,, \qquad \text{(II.10a)}$$

and

$$\varepsilon_{r2} = \sqrt{C_1/C_2}\,. \qquad \text{(II.10b)}$$

The parameters C_1 and C_2 are then defined completely in terms of the *s*-parameters, and the material constants ε_{r2} and μ_{r2} are likewise determined.

III. Time Domain Measurements: Derivation of s_{11} and s_{12}, and Conversion to Material Parameters

The previous section demonstrated that the material parameters ε_{r2} and μ_{r2} could be determined from the time-harmonic *s*-parameters. In this section we will show how the required *s*-parameters can be expressed in terms of a transient, time-domain measurement.

Consider the bounce diagram [Ref. 9] shown in Figure 2. The diagram represents the geometry of Figure 1, and depicts the transient wave behavior one would observe if a wave $e^{inc}(t) = e_0(t - \tau_1)$ were incident on the Region 1 - Region 2 interface from the left. Note that the reference is the waveform at position P_1 (see Figure 1b), but the waveform incident on the interface is $e^{inc}(t)$. In the figure

$$\Gamma_{12} = \frac{Z_2 - Z_0}{Z_2 + Z_0} = \text{reflection coefficient at Region 1/2 interface,} \qquad \text{(III.1a)}$$

$$\Gamma_{21} = \frac{Z_0 - Z_2}{Z_2 + Z_0} = -\Gamma_{12} = \text{reflection coefficient at Region 2 / 1 interface,} \qquad \text{(III.1b)}$$

$$T_{12} = 1 + \Gamma_{12} = \text{transmission coefficient at Region 1/2 interface, and} \qquad \text{(III.1c)}$$

$$T_{21} = 1 + \Gamma_{21} = \text{transmission coefficient at Region 2/1 interface.} \qquad \text{(III.1d)}$$

Also, τ_1 = propagation time from the point of observation in Region 1 to the Region 1/2 interface, τ_2 = propagation time across Region 2, and τ_3 = propagation time from the point of observation in Region 3 to the Region 2/3 interface (see Figure 1b).

In general, the reflected (transmitted) wave is given by the convolution of the incident wave with the time domain reflection (transmission) coefficient, or

$$e^{ref}(t) = e^{inc}(t) * s_{11}(t) = \int_0^\infty e^{inc}(\lambda) s_{11}(t - \lambda)\, d\lambda, \qquad \text{(III.2)}$$

where $e^{ref}(t)$ is the reflected waveform at the interface in Region 1, $e^{inc}(t) = e_0(t - \tau_1)$ is the waveform incident on the interface, and $e^{inc}(t) = 0$ for $t < 0$. In the frequency domain this relationship becomes simple multiplication

$$E^{ref}(\omega) = E^{inc}(\omega) \cdot s_{11}(\omega) \cdot e^{-j\omega\tau_1} = E_0(\omega) \cdot s_{11}(\omega) \cdot e^{-j2\omega\tau_1}, \qquad \text{(III.3)}$$

where we have now let the reference location be position P_1 as shown in Figure 1b (characterized by the multiplying term $e^{-j2\omega\tau_1}$, where τ_1 is the one-way transit time from position P_1 to the Region 1-2 interface). Other ways to view the time domain interaction

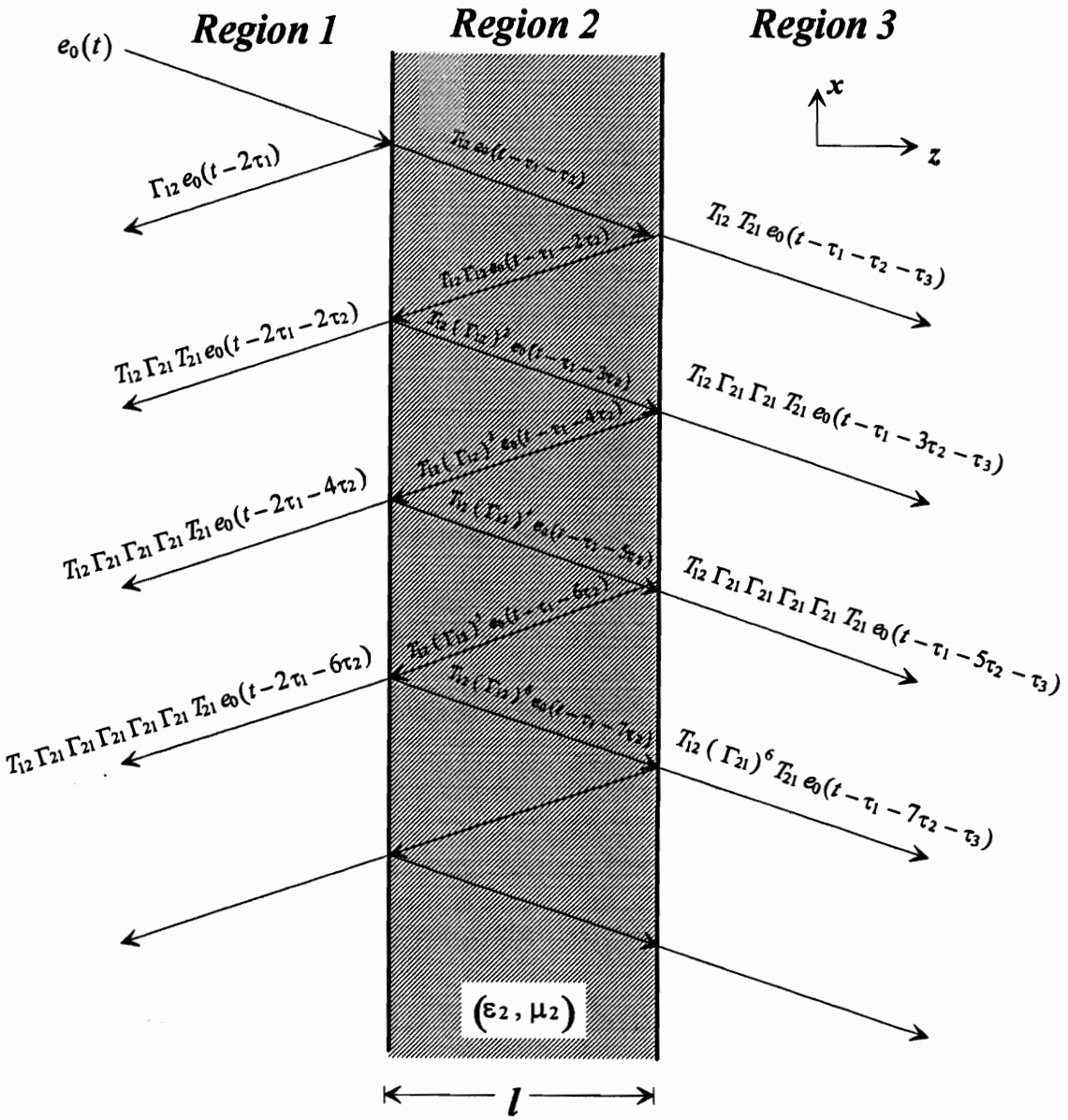

Figure 2. **Bounce diagram for the geometry depicted in Figure 1; a transient wave under goes an infinite number of transmissions and reflections at the Region 1-2 / 2-1 and Region 2-3 interfaces.**

of the electromagnetic field with the dielectric have been presented [Ref. 10, 11, 12]. Note that though the convolution operation is implied in Figure 2, it is not explicitly shown. Examination of Figure 2 reveals that the reflected and transmitted waves can be written as

$$e^{ref}(t) = e_0(t-2\tau_1) * \Gamma_{12} + \sum_{n=0}^{\infty} T_{21}(t) * \left\{ (\Gamma_{21} *)^{2n+1} \left\{ T_{12} * e_0(t-2\tau_1-2(n+1)\tau_2) \right\} \right\}, \quad \text{(III.4a)}$$

and,

$$e^{tran}(t) = \left\{ e_0(t-\tau_1-\tau_2-\tau_3) * T_{12} \right\} * T_{21} + \sum_{n=0}^{\infty} T_{21} * \left\{ (\Gamma_{21} *)^{2(n+)1} \left\{ T_{12} * e_0(t-\tau_1-(3+2n)\tau_2-\tau_3) \right\} \right\}. \quad \text{(III.4b)}$$

The notation $(\Gamma_{21} *)^m$ means that the expression to the right of this term is to undergo m convolutions with Γ_{21}, and the explicit time dependence is not shown. Also, for convenience and notational simplicity the time lag in the right hand side has been grouped together in the term $e_0(\cdot)$. Fourier transforms of both sides of Eqns. III.4a and b then give an equivalent frequency domain description. That is

$$E^{ref}(\omega) = E_0(\omega) \cdot \Gamma_{12}(\omega) \cdot e^{-j2\omega\tau_1} + \sum_{n=0}^{\infty} T_{21}(\omega) \cdot T_{12}(\omega) \cdot (\Gamma_{21}(\omega))^{2n+1} E_0(\omega) e^{-j2\omega(\tau_1+(n+1)\tau_2)}, \quad \text{(III.5a)}$$

and,

$$E^{tran}(\omega) = E_0(\omega) \cdot T_{12}(\omega) \cdot T_{21}(\omega) \cdot e^{-j\omega(\tau_1+\tau_2+\tau_3)} + \sum_{n=0}^{\infty} T_{12}(\omega) \cdot T_{21}(\omega) \cdot \left(\Gamma_{21}(\omega) \right)^{2(n+1)} \cdot E_0(\omega) \cdot e^{-j\omega(\tau_1+(3+2n)\tau_2+\tau_3)}. \quad \text{(III.5b)}$$

The scattering coefficients s_{11} and s_{21} can be expressed in the frequency domain as

$$s_{11}(\omega) = \frac{E^{ref}(\omega)}{E_0(\omega)} = e^{-j2\omega\tau_1}\Gamma_{12}(\omega) + \sum_{n=0}^{\infty} T_{21}(\omega) \cdot T_{12}(\omega) \cdot \left(\Gamma_{21}(\omega) \right)^{2n+1} \cdot e^{-j2\omega(\tau_1+(n+1)\tau_2)}, \quad \text{(III.6a)}$$

and,

$$s_{21}(\omega)=\frac{E^{tran}(\omega)}{E_0(\omega)}=T_{12}(\omega)\cdot T_{21}(\omega)\cdot e^{-j\omega(\tau_1+\tau_2+\tau_3)}$$
$$+\sum_{n=0}^{\infty}T_{12}(\omega)\cdot T_{21}(\omega)\cdot\left(\Gamma_{21}(\omega)\right)^{2(n+1)}\cdot e^{-j\omega(\tau_1+(3+2n)\tau_2+\tau_3)}. \qquad \text{(III.6b)}$$

The important point to note about Eqns. III.6 a and b is that they can be completely determined in terms of $\Gamma_{12}(\omega)$ and $T_{12}(\omega)\cdot T_{21}(\omega)$ ($\Gamma_{21}(\omega)$ can be defined in terms of $\Gamma_{12}(\omega)$ through III.1b).

Referring back to the bounce diagram, Figure 2, one notes that in the time domain the first component observed in Region 1 of the (total) reflected waveform is

$$p_1(t)=\Gamma_{12}*e_0(t-2\tau_1), \qquad \text{(III.7)}$$

then the time domain reflection coefficient Γ_{12} (= the reflection coefficient at the Region 1/2 interface when the width of Region 2, $t\rightarrow\infty$) can be determined directly from a measurement of $p_1(t)$. Similarly, the first transmitted component observed in Region 3 is

$$p_2(t)=T_{12}*T_{21}*e_0(t-\tau_1-\tau_2-\tau_3), \qquad \text{(III.8)}$$

and the time domain product of the transmission coefficients $T_{ab}\cdot T_{ba}$ (where T_{ab} = the transmission coefficient from Region a to Region b when the width of Region b, $t\rightarrow\infty$) can be determined directly from a measurement of $p_2(t)$.

The values of $\Gamma_{12}(\omega)$ and $T_{12}(\omega)\cdot T_{21}(\omega)$ will be found from Fourier transforms of the measured quantities $p_1(t)$ and $p_2(t)$ (Eqns. III.7 and III.8), and division by the incident waveform. The scattering coefficients s_{11} and s_{21} can next be determined from Eqns. III.6a and III.6b, and finally, values of material ε_2 and μ_2 can be extracted in the manner described in Section II.2.

III.1. Extraction of Material Properties from Time Domain Measurements

Here, a description of algorithmic process used to determine the material properties ε_2 and μ_2 of the sample held in Region 2 is presented. The procedure is as follows. A voltage pulse is introduced in the coaxial test fixture (described in Section IV) and measured at Position P_1. To allow uncorrupted measurement of the incident, reflected and transmitted pulses, the incident pulse width must not exceed a maximum value (discussion of allowable pulse width given in Section IV.2), for this work τ_W = incident pulse width = 1 ns. The incident pulse, $e_0(t)$, is measured at location P_1. Then, the first

component of the reflected pulse, $p_1(t)$ is also measured at P_1, but with additional time delay $(2\tau_1)$ corresponding to the round-trip time from the measurement (or reference position) to the interface of Regions 1 and 2. Next, the first component of the transmitted pulse, $p_2(t)$, is measured at position P_2 in the coaxial test fixture. Again, time delay $(\tau_1+\tau_2+\tau_3)$ corresponding to the one-way trip time from the reference position to the measurement location in Region 3 must be accounted for. Note that values of τ_1, τ_2, and τ_3 will also need to be determined. This can be done in a number of ways; for example direct measurement on the scope, or TDR-type measurements (see Section IV.5.5).

Once the raw data has been collected, form the transforms of $p_1(t)$ and $p_2(t)$ in the usual way with the Fourier transform pair

$$F(\omega)=\Im\{f(t)\}=\int_{-\infty}^{\infty} f(t)\cdot e^{-j\omega t}dt, \text{ and}$$
$$f(t)=\Im^{-1}\{F(\omega)\}=\frac{1}{2\pi}\int_{-\infty}^{\infty} F(\omega)\cdot e^{+j\omega t}d\omega, \tag{III.9}$$

and evaluate $\Gamma_{12}(\omega)$ and $T_{12}(\omega)\cdot T_{21}(\omega)$ via Eqns. III.7 and III.8. Next form the quantities s_{11} and s_{21} (Eqns. III.6a and III.6b). Though originally written in terms of an infinite series, there is an easier way to evaluate the quantities s_{11} and s_{21}. Consider the well-known infinite series [Ref. 13]

$$\sum_{n=0}^{\infty} x^n=\frac{1}{1-x}, \quad |x|<1. \tag{III.10}$$

Then Eqn. III.10 can be used to express Eqns. III.8a and b in forms more easily evaluated numerically. Equation III.8a becomes

$$\begin{aligned} s_{11}(\omega) &= e^{-j2\omega\tau_1}\Gamma_{12}(\omega)+\sum_{n=0}^{\infty} T_{21}(\omega)\cdot T_{12}(\omega)\cdot\left(\Gamma_{21}(\omega)\right)^{2n+1}\cdot e^{-j2\omega(\tau_1+(n+1)\tau_2)} \\ &= e^{-j2\omega\tau_1}\Gamma_{12}(\omega)+T_{21}(\omega)\cdot T_{12}(\omega)\cdot\Gamma_{21}(\omega)\cdot e^{-j2\omega(\tau_1+\tau_2)}\sum_{n=0}^{\infty}\left(\Gamma_{21}(\omega)\right)^{2n}\cdot e^{-j2\omega n\tau_2} \\ &= e^{-j2\omega\tau_1}\Gamma_{12}(\omega)+\frac{T_{21}(\omega)\cdot T_{12}(\omega)\cdot\Gamma_{21}(\omega)\cdot e^{-j2\omega(\tau_1+\tau_2)}}{1-\Gamma_{21}(\omega)^2\cdot e^{-j2\omega\tau_2}} \end{aligned} \tag{III.11a}$$

and III.8b becomes,

$$
\begin{aligned}
s_{21}(\omega) &= T_{12}(\omega)\cdot T_{21}(\omega)\cdot e^{-j\omega(\tau_1+\tau_2+\tau_3)} + \sum_{n=0}^{\infty} T_{12}(\omega)\cdot T_{21}(\omega)\cdot\left(\Gamma_{21}(\omega)\right)^{2(n+1)}\cdot e^{-j\omega\left(\tau_1+(3+2n)\tau_2+\tau_3\right)} \\
&= T_{12}(\omega)\cdot T_{21}(\omega)\cdot e^{-j\omega\left(\tau_1+\tau_2+\tau_3\right)} \\
&\quad + T_{12}(\omega)\cdot T_{21}(\omega)\cdot\Gamma_{21}(\omega)^2\cdot e^{-j\omega\left(\tau_1+3\tau_2+\tau_3\right)}\sum_{n=0}^{\infty}\left(\Gamma_{21}(\omega)\right)^{2n}\cdot e^{-j\omega 2n\tau_2} \\
&= T_{12}(\omega)\cdot T_{21}(\omega)\cdot e^{-j\omega\left(\tau_1+\tau_2+\tau_3\right)} + \frac{T_{12}(\omega)\cdot T_{21}(\omega)\cdot\Gamma_{21}(\omega)^2\cdot e^{-j\omega\left(\tau_1+3\tau_2+\tau_3\right)}}{1-\Gamma_{21}(\omega)^2\cdot e^{-j\omega 2\tau_2}}
\end{aligned}
\qquad \text{(III.11b)}
$$

The expressions for the scattering coefficients given in Eqns. III.11a and b then are easily evaluated from knowledge of $\Gamma_{12}(\omega)$ and $T_{12}(\omega)\cdot T_{21}(\omega)$, determined from measurements, Fourier transforms of $p_1(t)$ and $p_2(t)$, and simple mathematical manipulation as described above.

IV. Description of Measurement Hardware and Measurement Procedure

This section describes the physical hardware of the measurement test fixture, the electrical sensors and their characteristics, the pulse generator employed, and data acquisition equipment and data reduction. Also presented is a discussion of clear time considerations that drove the design of the axial dimensions of the coaxial test fixture.

IV.1. Coaxial Test Fixture

The coaxial test fixture houses the sample material, provides for a "clean" transition of the small coaxial geometry of the source to the larger dimensions of the sample, and provides mounting for the sensors that measure the incident, reflected and transmitted waveforms. An annotated photograph and drawing of the measurement hardware is shown in Figures 3a and 3b below. The fixture itself is comprised of three sections. The line is fabricated from aluminum with stainless steel inserts where mounting screws are used. Note the use of the flanges to firmly attach the sections to one another. The **Input Section** is 7 inches in length and transitions from the SMA (small) geometry to the larger geometry of the main section of the line. To do this the input section tapers, in a constant 50-Ω impedance fashion, to the dimensions of the main part of the line. The inner and outer dimensions of the larger portion of the line are $a = 1.1734$ and $b = 2.7000$ inches respectively. This results in a transmission line characteristic impedance of

$$Z_0 = 60\ln\left(b/a\right) = 60\cdot\ln\left(2.75/1.195\right) = 50\ \Omega \qquad \text{(IV.1)}$$

for a free space filled transmission line. Two input sections are used, one for the input transition and the second for the output transition.

The **Sensor Section** of the transmission line follows. This section is long enough to provide the required clear time between the incident and reflected waveforms, and provides support, a location and hardware for the sensor mounts. The present sections are 14 inches in length (round trip clear time ≈ 2.37 ns), but because of the modular nature of the hardware a longer section could be fabricated if the test conditions require. A sensor mount with a differentiating electric field sensor is shown and indicated in the figure below.

The **Sample Section** is the third piece of the transmission line hardware. This section is meant to hold snugly the material under test. It is present 9 inches in length, but can be made to any length required. This section is long enough to provide the required clear time between the incident and reflected waveforms, and provides support, a location and hardware for the sensor mounts. All sections are held together with six socket head cap screws, size ¼-20, which are 0.75 inches long. These screws are placed symmetrically around the flanges of each section, and thread into the stainless steel inserts to firmly mate the sections together. The sensor mounts are held in place with two 6-32 socket head cap screws, which are ¼ inch in length. Again, the screws thread into stainless steel inserts.

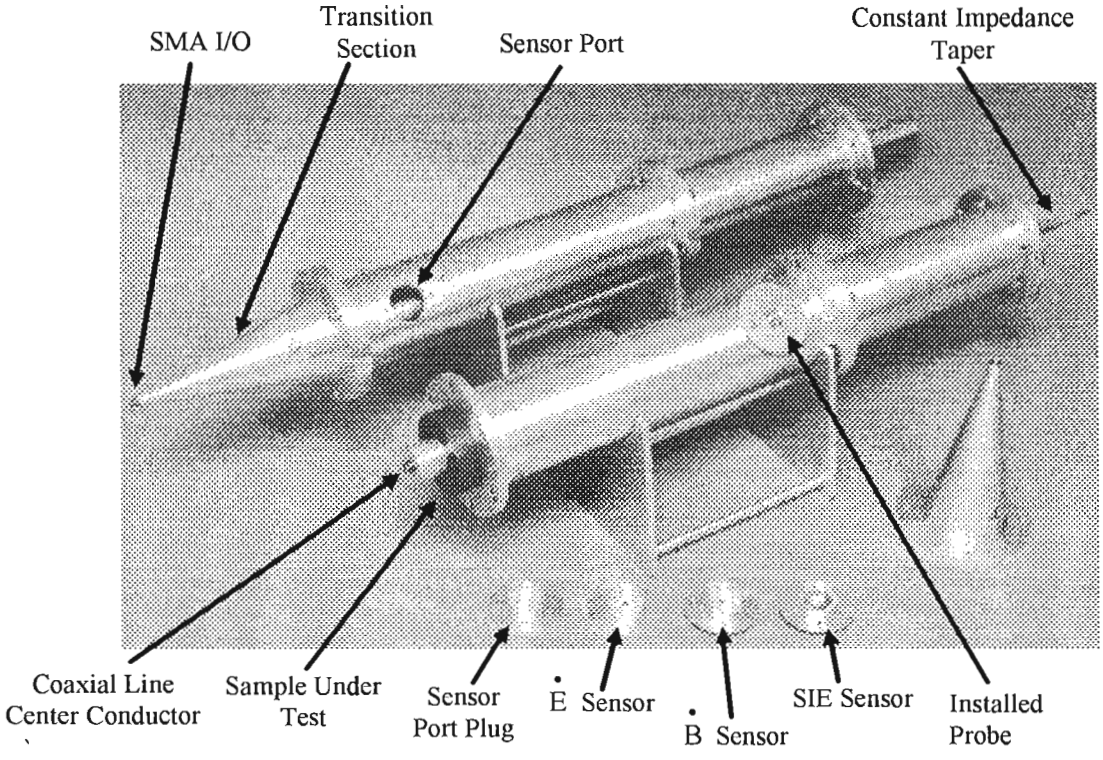

(a)

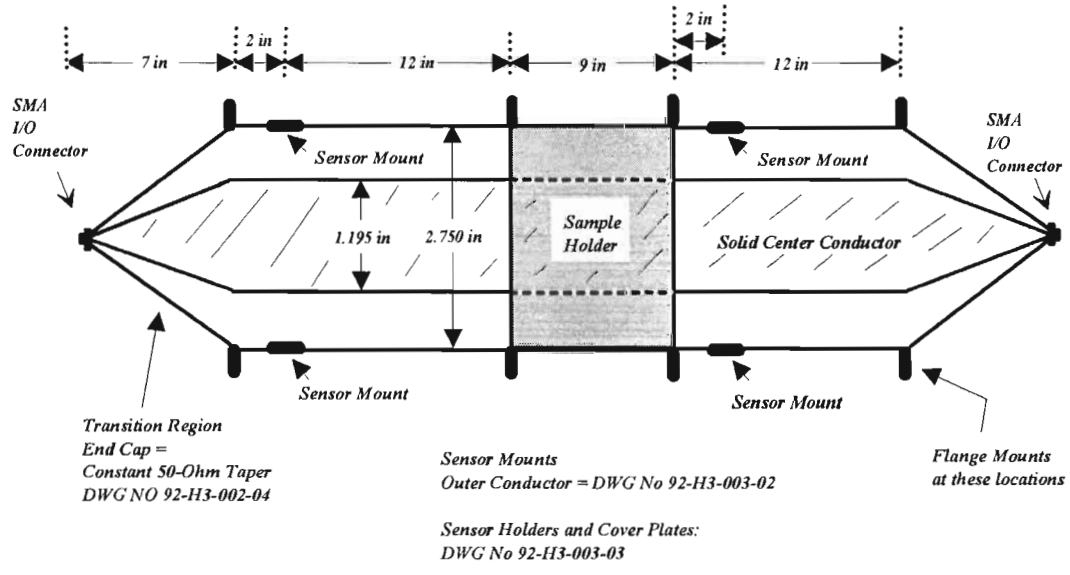

(b)

Figure 3. Coaxial fixture of the Time Domain Measurement Hardware Set: (a) annotated photograph of the coaxial test fixture; and (b) functional drawing.

IV.2. Timing or Clear-Time Considerations

As described, the reduction to material electrical characteristics requires the time domain measurement of the incident waveforms, the first reflected component of the reflected waveform, and the first transmitted component of the transmitted waveform. There are two sensor locations in the measurement hardware (described below). The sensor in the first position measures the incident and reflected waveforms, while the sensor when in the second measurement position measures the components of the transmitted waveform.

Due to the nature of the sensor (described below) it is responsive to a waveform traveling both ways on the line, and consequently responds to both the incident and reflected signals on the transmission line. In order to separate the waveforms, time isolation between each waveforms arrival at the location of the sensor must be provided. This requirement for time isolation dictates the maximum pulse width usable, the sample length, and the length of the measurement transmission line between the first sensor position and the sample front interface. Consider again Figure 1. There, the one way travel time from the sensor position to the front face of the sample is indicated as τ_1. Then, given that the input pulse width is τ_W, the length of transmission line required to provide time isolation between the input and reflected pulses is

$$l_1 > \frac{\tau_W}{2} \cdot c_1 \qquad \text{(IV.2)}$$

where l_1 = length of transmission line between the sensor position and the front face of the sample, and c_1 = propagation speed in the line (free space velocity for an empty line. The minimum pulse width attainable with the present hardware is $\tau_W \approx 1$ ns. Then

$$l_1 > \frac{1 \times 10^{-9}}{2} \cdot 3 \times 10^8 = 0.150 \text{ m} = 5.91 \text{ inches} \qquad \text{(IV.3)}$$

at a minimum for the length of the first section. We have found that the value used for the pulse width should exceed by 50% the nominal value of incident waveform pulse width. This allows enough time for the slow tailing part of the waveform to decay before the first portion of the reflected pulse to appear at the sensor position.

The second clear time consideration concerns the multiple reflections of the excitation waveform that off the interior surfaces of the sample. As illustrated in the bounce diagram shown in Figure 2, a portion of the incident pulse passes through the front interface of the sample and travels to the rear interface. There, part is transmitted and part is reflected. A portion of the reflected component will eventually arrive at the location of the input sensor. If the round trip travel time through the sample is less than the input pulse width, then the components of the reflected waveform will overlap, making a clean measurement of just the first component difficult or impossible. Therefore, in order to

allow time separation between the different components of the reflected waveform, the sample length must be at least

$$l_2 > \frac{\tau_W}{2} \cdot \frac{c_0}{\sqrt{\varepsilon_{r2}}} \qquad \text{(IV.4)}$$

where ε_{r2} = magnitude of the complex dielectric constant of the material in the second region (the material under measurement). For common plastics we can estimate $\varepsilon_{r2} \approx 2.2$, and for a pulse width $\tau_W \approx 1$ ns, the sample length must be

$$l_2 > \frac{1 \times 10^{-9}}{2} \cdot \frac{3 \times 10^8}{\sqrt{2.2}} = 0.101 \text{ m} = 3.98 \text{ inches.} \qquad \text{(IV.5)}$$

As before, we found that the sample length should be approximately 50% greater to account for the slow trailing edge of the excitation. Similar consideration apply to the components of the transmitted waveform. But satisfaction of the first two criteria given above insures the transmitted components will be sufficiently separated in time.

IV.3. Pulse Generator, Sampling Scope and Data Acquisition Software

This section briefly describes the associated hardware and software required to measure material permittivity and permeability using the coaxial line and data reduction scheme described previously. Below are given short descriptions of the Pulse Generator used to provide the incident waveform, the digital sampling oscilloscope employed to record the required waveforms, and the data acquisition software used to control the instrumentation, acquire the waveforms, and perform the data reduction algorithm.

IV.3.1. Pulse Generator

The pulse generator is a model number PSPL 4050B from Picosecond Pulse Labs, Boulder CO, 80301. This generator can produce 10 V amplitude pulses with 45 ps risetimes with as little as 1 ns pulse widths. The output of the pulse unit drives the input to the coaxial measurement hardware through a pulse sharpening head (Model No. 4050 RPH) and DC block. The characteristics of the output waveform of the pulse generator (configured for a 1 ns pulse width) are shown in Figure 4a. The pulse waveform is shown in Figure 4a, and the graph of its spectrum is given in Figure 4b.

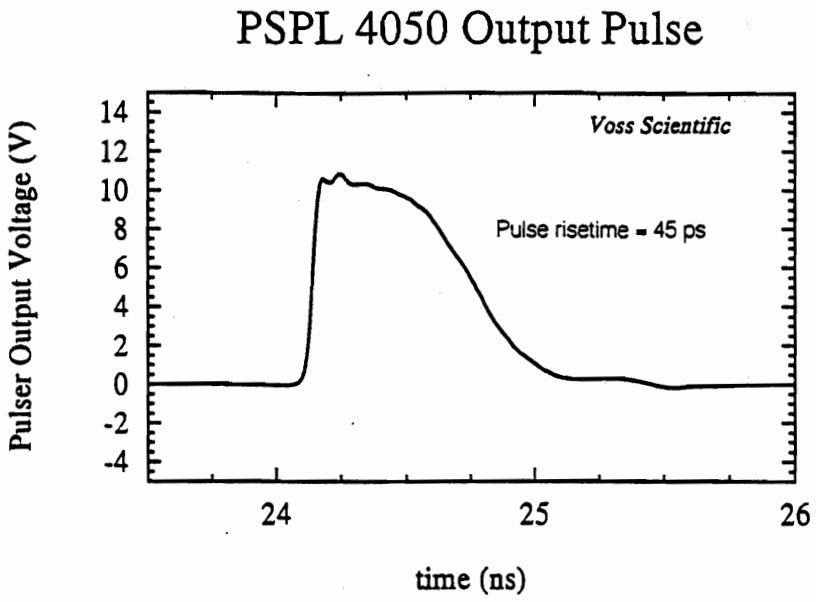

(a)

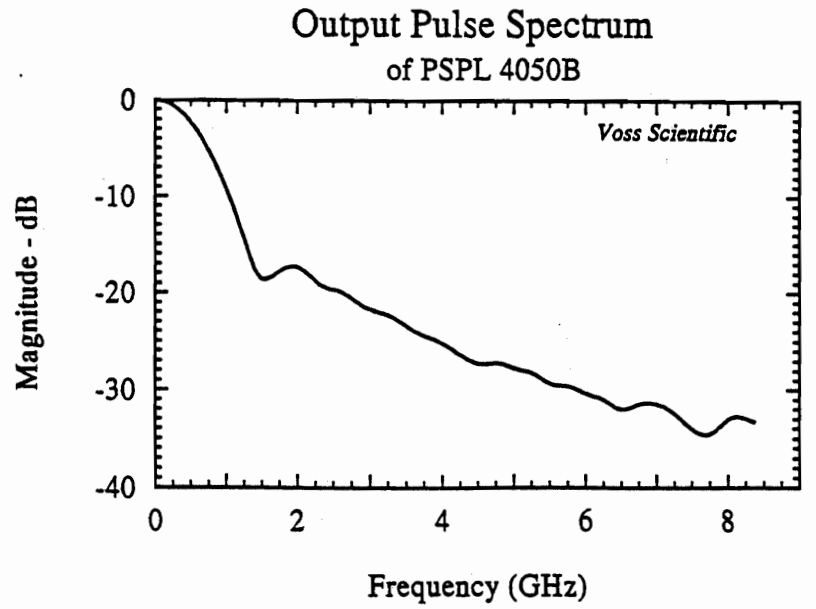

(b)

Figure 4. **The characteristics of the output waveform of the pulse generator: (a) 1 ns pulse waveform; and (b) pulse spectrum.**

IV.3.2. Digital Sampling Oscilloscope

The fast risetime, low amplitude characteristics of the input pulse waveform require the use of a high bandwidth sampling oscilloscope (fastest direct write scope available is the SCD5000, 4.5 GHz bandwidth). The Tektronix Model No. 11801A (Tektronix, Beaverton, OR) Sampling Oscilloscope with the Tektronix SD 24 sampling head, and 2 meter sampling head extender are employed for the measurement of the incident, direct, and transmitted waveforms. This combination of hardware is capable of recording 15 ps pulse risetimes (> 23 GHz equivalent bandwidth), and the use of the sampling head extender removes the influences of the cable between the sensor to sampling head on the measurement.

IV.3.3. Data Acquisition, Analysis, Archival and Control Software

The material characterization algorithm described in this paper is implemented as a custom module extension of the Voss Scientific, Inc. DA^3C software system. The DA^3C software is a fully integrated data acquisition system which includes automated instrument control, data archival, data analysis and data reduction capabilities. The system is composed of five executables which utilize Dynamic Data Exchange (DDE) communications to operate as a single, fully integrated package under Microsoft Windows.

The materials characterization waveforms are acquired with the standard DA^3C Acquisition module. Thus, the resulting waveforms are automatically stored into the database for later retrieval, and no modification to this subsystem was required. The user later retrieves and displays these waveforms from the data base with the Analyze module. A category called "Materials Characterization" was added to the "Analysis" section that requests that the user select, and thus identify, the incident, transient and reflected waveforms. Once the last waveform has been selected, the remaining data processing occurs automatically, utilizing some of the pre-existing functionality of this module and integrating other, totally custom code. The results (complex material permittivity and permeability as a function of frequency) are displayed using the standard analysis module interface.

This integration of the materials characterization code with the Voss Scientific, Inc. DA3C system results in a much friendlier, better behaved system with greatly increased analysis options than would have otherwise been feasible given the time and support available.

IV.4. Sensors and Sensor Characteristics

There are particular and demanding requirements on the sensors used to measure the incident, reflected and transmitted waveforms. These include:

1. **Non-Perturbing** - The size of the coaxial line permits propagation of higher order modes at frequencies above approximately 2 GHz, and the presence of any structure which is not part of, or conformal with the coaxial transmission line geometry can promote higher order modes. Since the reduction algorithm assumes TEM mode propagation, the generation of other modes by the presence of the probe would lead to erroneous results and limit the usable bandwidth of the measurement hardware. What is required then, is a sensor that does not perturb the waveform, or generate higher order modes.

2. **Sensitivity** - The PSPL pulse source provides a 10 V output pulse. The sensor must have sufficient sensitivity and signal-to-noise ratio to enable measurement of the waveforms. Typically the measurement of the transmitted and reflected waveforms present the greatest challenge. For materials with high dielectric constants, the mismatch means small amplitude signals are transmitted through the material sample. For materials with low dielectric constants, the reflected waveform will be small.

3. **Bandwidth** - A measurement system with 10 GHz bandwidth is one of the goals of this effort. Consequently, the sensor must exhibit comparable capability. To realize the required bandwidth means the sensor must be capable of resolving 35 ps risetimes.

4. **Fidelity** - The data reduction technique employed to derive material electrical properties from measurements means that accurate sensing of the waveforms is critically important. No dependence on orientation can be tolerated (for example, the output of a B-dot probe is proportional to its orientation to the incident field), and the probe must not exhibit resonances in the bandwidth of interest.

With the above considerations in mind, we considered the use of three types of sensors: (1) Self-Integrating Electric Field Sensors; (2) Zero Area B-dot Sensors; and (3) E-dot Sensors. A brief discussion of the characteristics is given below.

IV.4.1. Self-Integrating E-Field Sensors

The most popular electric field sensors, which operate in the frequency regimes of interest - 0.050 - 5 GHz, are differentiating-type sensors. These sensors, though well characterized, can be difficult or impossible to use in coaxial environments, and require integration of the raw waveform to realize the form of the desired signal. Voss Scientific has patented the Self Integrating Electric Field Sensor (SIE Sensor), and has adapted it for use as an internal diagnostic in the coaxial geometry of the H-series sources. The sensor has exhibited risetimes < 60 ps, and is conformal and non-perturbing to the field environment of the source. The electrical performance of the sensor is described in a Voss

Scientific Technical Note[1] available from Voss Scientific. However, these sensors exhibit circuit-type behavior (exponential decay) which makes differentiation of the individual components difficult. The signal-to-noise ratio also is unacceptably large for this application (sensor sensitivity is very low). Consequently, though the sensors provide a signal which is directly proportional to the measured waveforms, the sensors fidelity and sensitivity are not adequate for this task.

IV.4.2. Zero Area B-dot Sensors

Often, one wishes to measure current of magnetic field directly (rather than infer its value form the electric field or voltage and relate current through transmission line relations). Voss Scientific has developed a line of Zero Area B-dot sensors that perform with < 50 ps risetime (> 7 GHz BW). The sensors are compact, conformal, robust and quite suitable for use in coaxial geometries. The sensitivity of the sensor can also be adjusted over a wide range of values. However, the output of the sensor is sensitive to its orientation relative to the incident waveform. Also, the sensor bandwidth is not quite sufficient (though it can be improved utilizing careful fabrication techniques). For these reasons the Zero Area B-dot sensor was not chosen for this application.

IV.4.3. E-dot Sensors

The E-dot sensor (basically just a type of SMA connector) was chosen as the sensor for this application. Given the requirements of the application, and the limitations of the sensors just described, this was the only sensor that provided satisfactory performance. It also has the advantages of being cheap and commercially available. The sensor is an Omni-Spectra SMA bulkhead feed-through connector (the same type used to fabricate the Zero Area B-dot sensor), Omni-Spectra Part No. 2052-3123-00. It mates directly with the sensor B-dot mounts, and is secured to the mount with 4, 2-56 × ¼ inch socket head cap screws. The center conductor of the connector extends just 2 mm into the coaxial line, so it is very non-perturbing. The sensing element is axially symmetric (just a wire) and is insensitive to rotational orientation in the mount. It is just a fraction of a wavelength long at the highest frequency of interest, hence it is electrically short with commensurate bandwidth. The sensitivity of the probe is also quite good, but the output is proportional to the time derivative of the measured waveform. Normally, the fact that the sensor outputs a derivative-type signal would be a liability, but as discussed below, we have found it advantageous to work directly with the differential signal.

Consider the pulser output time derivative shown in Figure 5a. This is the form of the E-dot sensor output signal. The spectrum of this signal is shown in Figure 5b. One notes the broader spectrum compared to the spectrum of the waveforms shown in Figure 4b. This is a consequence of the differentiation (in the frequency domain equivalent to

---

[1] "Reduction Formulas for Self-Integrating E-field Sensors," TN002, C. Courtney, Voss Scientific, 8 June 1995.

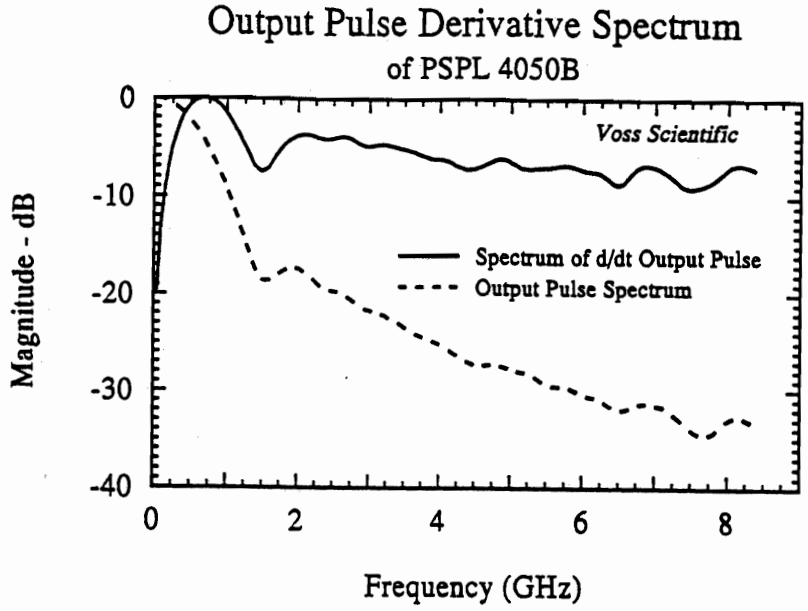

(a)

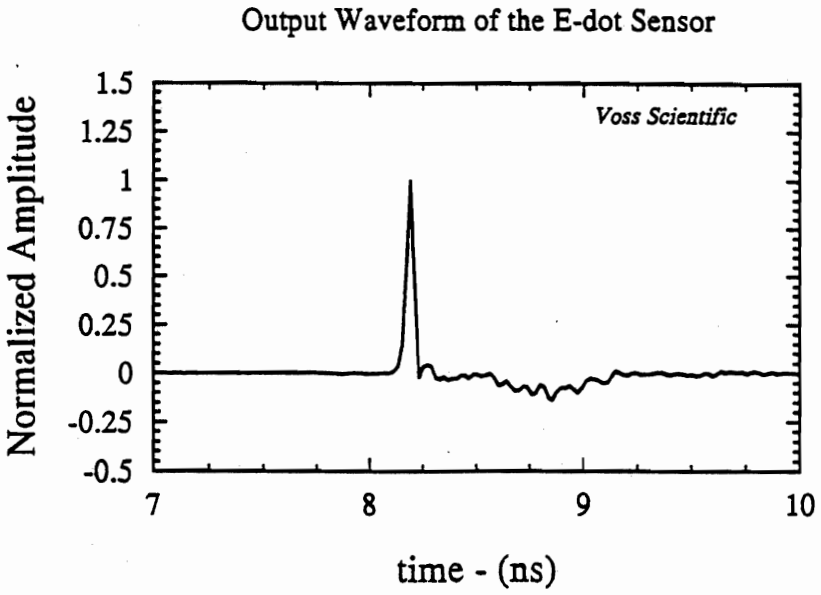

(b)

Figure 5. **The characteristic form of the E-dot sensor output waveform: (a) time domain record of the derivative of a pulse; and (b) spectrum of the time derivative.**

multiplication by jω). The wider spectral content of the differentiated waveform can be used to advantage. It results in a greater signal-to-noise ratio at the higher frequencies. Furthermore, since the data reduction algorithm operates on ratios of the spectrums of the incident, reflected and transmitted waveforms, the derivative nature does not affect the results (it is a common multiplicative operator to all of the data that factors out). Consequently the E-dot sensor characteristics satisfy all of the requirements given above and is the sensor chosen for this application.

IV.5. Measurement Procedure

This section provides a clear description of the measurement procedure required to measure the permittivity and permeability of a sample material with the Time Domain Metrology Hardware and Software. Given will be the techniques used to determine all constants needed to execute the data reduction (samples lengths, transit time determinations, etc.), measurement procedure, pre-processing of the raw data, and data post-processing methodology.

IV.5.1. Sample Preparation and Placement in the Fixture

The sample should be prepared to fit snugly inside the coaxial line, the inner and outer dimensions should be accurate to within a couple of mils ($\pm 5 \times 10^{-3}$ cm). This tolerance will result in a tight fit of the sample in the line; no gaps will exist that will allow alternative propagation paths which could result in a pre-pulse in the transmitted portion of the waveform. The length of the sample should be consistent with the clear time requirements discussed earlier. This will often require some initial estimate of the material permittivity, although assuming that $\varepsilon_r = 2$ should result in sample size sufficiently long to meet the clear time needs. The sample then should be placed approximately in the center of the fixture, ensuring that the first component of the reflected wave is separated in time from the incident waveform. The sample can be moved further from the input port of the line if more time isolation is needed. The second sensor position can be located just after the rear sample interface. There is no clear time requirement for this measurement.

IV.5.2. Hardware and Probe Setup

The hardware used to make the physical measurements has been described. Their connection is straightforward. The Tektronix SD 24 sampling head of the 11801 Sampling Scope is connected to the E-dot sensor via the 2-meter sampling head extension. The PSPL pulse generator drives the input port of the coaxial test fixture (either port can serve as the input port), and the self trigger of the pulse generator is used to trigger the oscilloscope. The output end of the coaxial hardware would normally need to be terminated, especially for a frequency domain measurement. However, since the hardware set has been designed to provide ample clear time, the output transition section can be left off. This section can be tedious to put on and is not needed to acquire the measurements.

IV.5.3. Oscilloscope Trigger and Trigger Level

As mentioned, the PSPL pulse generator supplies the trigger waveform to the oscilloscope. A convenient feature of the PSPL 4050B is the ability to set pre-trigger via the front panel. This allows one to pre-trigger the scope such that the actual waveform can be recorded properly. We have found that 40 ns of pre-trigger (selectable on the front panel of the pulse generator) is usually sufficient. The output trigger level of the pulse generator is 10 V. The maximum allowable amplitude at the scopes trigger input is 5 V RMS. Therefore one must ensure that the trigger line has the proper amount of attenuation. The oscilloscope has an internal, user selectable 10 dB attenuator that can be used, but this is not enough. At least an additional 6 dB should be used. The trigger output connector on the Pulse Generator is a BNC-type connector. However, due to the way of the sampling scope operates, the fidelity of the trigger pulse must be maintained. We recommend the use of BNC to SMA adapters and high-quality coaxial cable (RG-142 or better) to carry the trigger line to the scope trigger input.

Finally, the trigger level of the scope can dramatically affect the signal-to-noise ratio of the measured waveform. Consider the waveforms shown in Figure 6. Both waveforms were acquired under identical conditions, except that the trigger level for Figure 6a was 1.0 V, and the trigger level for Figure 6b was 0.4 V. The waveform acquired with the higher trigger level is "cleaner" and exhibits a faster risetime. The trigger level of the scope should be set to coincide with the fastest portion of the pulse generator's trigger. Insure that the trigger level for the scope is set the same for all acquisitions, the waveforms in Figure 6 indicate that the acquired waveforms can exhibit a shift in the baseline otherwise.

IV.5.4. Waveform Acquisition

At least two measurements are required, one that is indicative of the incident and reflected waveforms, which are obtained from a sensor placed some distance in front of the material sample interface, between the input port and the front sample interface. A second measurement of the transmitted waveform is also required. This is taken from a sensor placed behind the rear interface of the sample. The same sensor should be used to make both measurements. Simply make the first measurement, turn the pulser to standby and move the sensor, then turn the pulser back to free run and acquire the second waveform. Again, ensure that the trigger levels for both acquisitions are the same. Of course, one uses the DA^3C system to directly control all of the sampling oscilloscope, acquire the raw waveforms and store the measurements for later recall and processing.

The normal instrument set up for this measurement is to use a 5 - 10 ns window, with the vertical amplitude set to 5 - 10 mV/div, and the pulse generator should be set at 10 - 100 kHz rep rate. Remember to turn the pulse generator output off when not in use. It has a limited lifetime and should be on only when making a measurement. It is a good

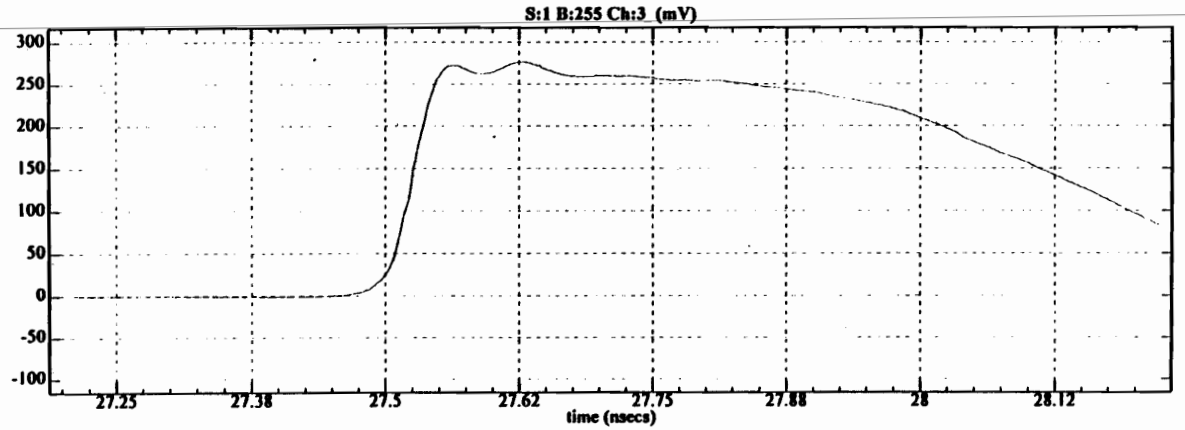

(a)

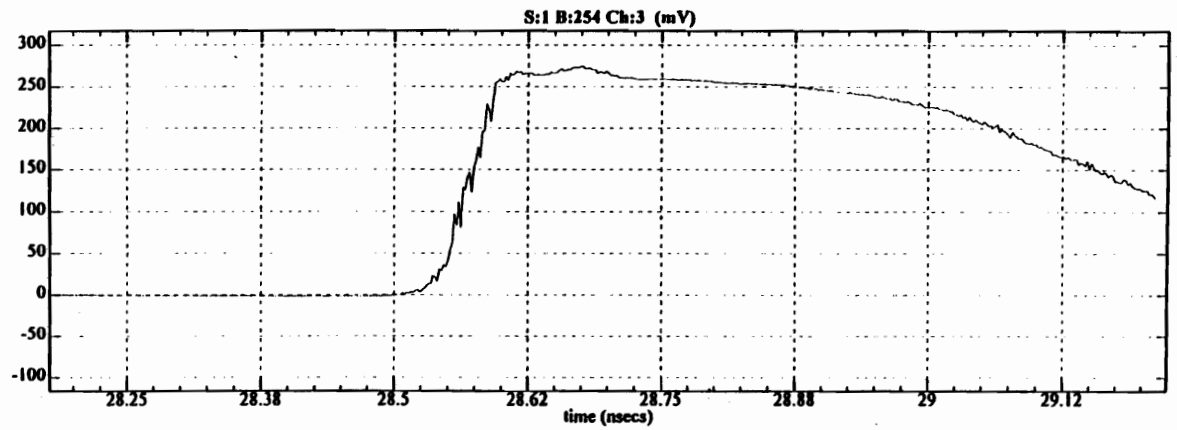

(b)

Figure 6. **The dependence of the recorded waveform on the trigger level: (a) 1 V trigger level; and (b) 0.4 V trigger level.**

idea to leave the unit powered up, thermal stabilization seems to help the performance. The sampling heads also should be left powered up between measurements. Try and acquire the measurements with as little elapsed time between measurements as possible. We have noticed a drift of a few 10's of picoseconds in the recorded output waveform over the course of 10 minutes. This drift should be minimized as much as possible.

IV.5.5. Determination of Time Constants

The user needs to enter four constants to the Time Domain Materials Characterization data reduction module. These constants (particular to each sample material, and each measurement setup) are:

1. l = total length of the sample cylinder;
2. τ_1 = propagation time from the first sensor to the front face of the sample;
3. τ_2 = one way propagation time through the sample; and
4. τ_3 = propagation time from the rear face of the sample to the second sensor.

See Figure 1b. The length of the sample is easy to determine, one measures it with high-quality calipers. The measurement should be made with sub-millimeter accuracy. The determination of the propagation times requires a bit more analysis. To determine τ_1 (propagation time from the first sensor to the front face of the sample), make a copy of the raw waveform associated with the measurement of the incident and reflected waveforms. Overlay the two waveforms using the Adjustable Overlay capability of the DA^{3}C Analysis software. Then use the controls to line up the peaks of the waveforms associated with the incident and reflected waveforms. The one way transit time, τ_1, is then half of the indicated offset.

The sample transit time, τ_2, is determined by measuring the time lag between the first and second echoes of the reflected waveform. The first echo is associated with the initial reflection from the front interface. The second echo is associated with the component that is transmitted through the front interface, travels to the rear interface, returns to the front interface and is transmitted through. This transit time is found by recording a sufficiently long time record from the sensor at the first position. One may get better resolution if the oscilloscope gain is increased, the first and second reflections. Then repeating the above procedure, and aligning the first and second echoes. The one way transit time, τ_2, is then half of the indicated offset.

The final transit time required by the Time Domain Materials Characterization module is the time of flight from the rear interface to the sensor in the second position, τ_3. This time is found by aligning the waveforms associated with the incident and transmitted waveforms. This yields the total transit time between the sensor locations, T. Then

$$T = \tau_1 + \tau_2 + \tau_3 \qquad \text{(IV.6)}$$

or, solving for τ_3

$$\tau_3 = T - \tau_1 + \tau_2 . \qquad \text{(IV.7)}$$

All of the information to determine this value has been collected.

IV.5.6. Data Pre-Processing

The timing and physical length constants have been determined using the procedure described in the previous section. What is left is to prepare the raw data associated with the incident, reflected and transmitted waveforms for submission to the reduction routine. Briefly, each of the three waveform records submitted must contain just information associated with that particular waveform. For example, we described how both the incident and reflected waveforms are recorded onto a single record using the same sensor. These waveforms must now be segregated and placed in their own file. We will illustrate for the case of the incident waveform.

Figure 7a is the raw data record associated with the incident and reflected waveform recorded at Sensor Position No. 1. Figure 7b retains the portion of the raw data associated just with the incident waveform. Note the need for time isolation between the different waveforms. The remainder of the record has been set to zero using the tools of the analyze package. Next, end points are added to extend the total record to 20 ns, the number of points in the window set to 512, and the data is re-interpolated. This is done for two reasons. The first is to have a time window long enough to contain the incident, and first components of the reflected and transmitted waveforms. The second is to have data suitably conditioned to yield the desired resolution in the frequency domain. For the combination of a 20 ns window and 512 sample points, the frequency results will extend to 25 GHz, with a resolution of 100 MHz. Of course the results obtained are valid only to about 8 GHz (see results below). One may alter these numbers if desired to obtain different frequency domain characteristics if desired. The other two waveforms must be similarly processed. Be sure that the three waveforms have the same number of points, with the same time window.

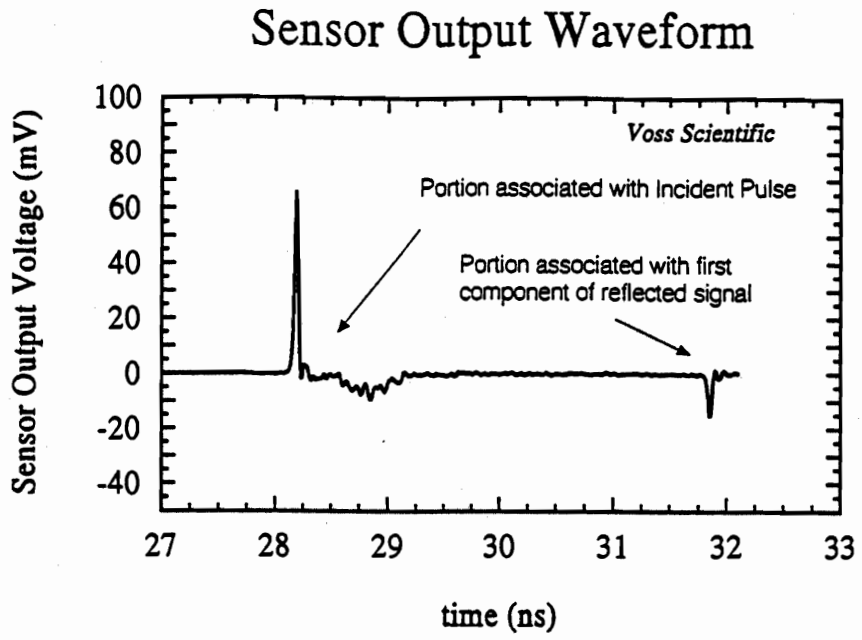

(a)

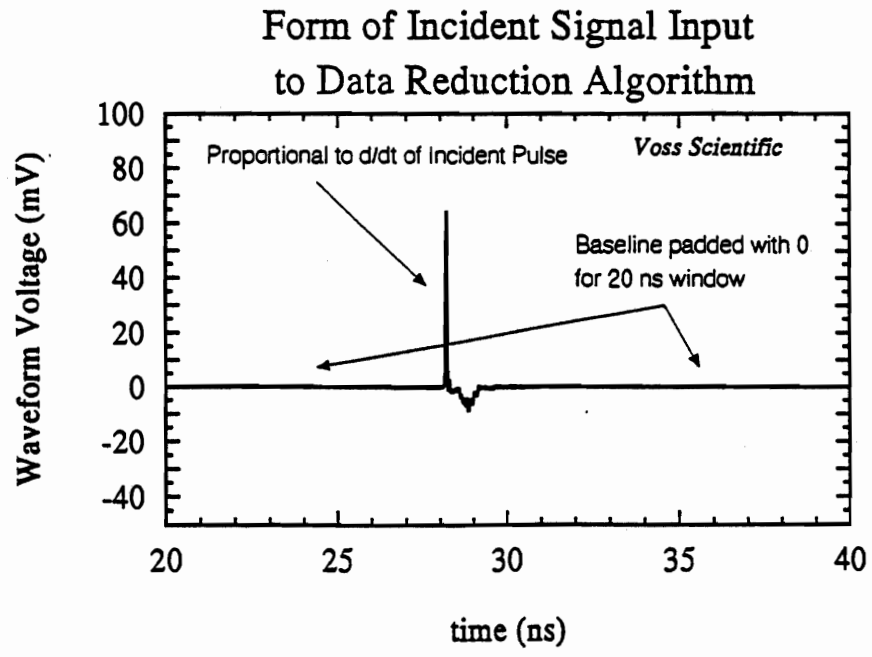

(b)

Figure 7. **Preprocessing of raw data: (a) raw data record associated with the incident and reflected waveforms recorded at sensor location No. 1; and (b) processed data which contains only information about the incident pulse, all other data associated with other components has been set to zero.**

IV.5.7. Data Post-Processing

When the pre-processing of the waveforms is complete, and the correct associated time and length constants have been entered, one calls the Materials Characterization algorithm from the Analysis module. The software will prompt the user to click on the waveform that represents the Incident, Reflected and Transmitted data. These windows must be "OPEN" in the Analyze module. After the waveform data is submitted, the data reduction algorithm is started. At the conclusion of the processing, the time domain waveform data windows will become icons, and graphs of the frequency dependence of the material permeability and permittivity will be displayed. These windows hold complex quantities, the real components are displayed initially and the imaginary portion is accessed via the F2 key. Note that each portion (real and imaginary) of these waveforms must be stored as the data base does not accommodate complex numbers. The user may wish to crop the data before it is stored or printed. The values associated with DC, and above 8 GHz may be of little value. Using the "cursors" feature of Analysis one may edit these results in any fashion desired.

V. Time Domain Measured Properties of Three Materials

This section presents the results of the time domain measurement of three materials using the methods described earlier. The materials that were measured are: Polyvinyl Chloride (PVC), Noryl EN265 (Polyphenylene Oxide)[2], and Concrete. Each sample was machined to fit inside the coaxial line with 1 mil of tolerance, and with a length of no less than six inches.

V.1. Measurement of Noryl

A bulk sample of Noryl EN265 was machined to a length of 6.000 ± 0.001 inches, and with cross sectional dimensions compatible with the coaxial line. The differentiating E-field probe was used to measure the time derivative of the incident, reflected and transmitted waveforms. These waveforms are shown in Figure 6. Note that just the first component of the reflected and transmitted waveforms is measured (and shown in the figure). The reduction algorithm forms the complete response from just these partial components. These waveforms are then analyzed to yield the required values of propagation times. To recall, τ_1 = propagation time from the first sensor to the front face of the sample, τ_2 = one way propagation time through the sample, and τ_3 = propagation time from the rear face of the sample to the second sensor. From the data shown in Figure 6 these values were found to be: $\tau_1 = 1.828$ ns; $\tau_2 = 0.8825$ ns; and $\tau_3 = 0.381$ ns. The physical length of the sample, the time of flight values, and the waveforms of Figure 8 were submitted to the data reduction software described earlier. The reduced values of relative permittivity and permeability for Noryl EN265 are given in Figures 9a-d for the frequency range 50 MHz - 8 GHz, greater than $7\frac{1}{2}$ octaves. Note that both the raw measured data and a linear interpolation are given in each graph. One sees that the real part of the relative dielectric constant is essentially constant over the band ($\varepsilon_r' \approx 2.7$), while the imaginary (loss) component varies from $-0.06 < \varepsilon_r'' < 0$ over the frequency band. Figures 9c,d show the Noryl is a non-magnetic material with $\mu_r' \approx 1.0$ and $\mu_r'' \approx 0.0$. GE data sheets[3] give the relative dielectric constant of Noryl EN265 as 2.69 and dissipation factor (loss tangent) as 0.0007, both at 60 Hz. These figures are consistent with the results reported here.

Note that both the raw measured data and a linear interpolation are given in each graph. One sees that the real part of the relative dielectric constant is essentially constant over the band ($\varepsilon_r' \approx 2.6$), while the imaginary (loss) component varies from $-0.06 < \varepsilon_r'' < 0$ over the frequency band. Figures 9c,d show the Noryl is a non-magnetic material with $\mu_r' \approx 1.0$ and $\mu_r'' \approx 0.0$.

---

[2] Noryl EN265 manufactured by General Electric Corp.

[3] http://www.ge.com/datasheets/NORYLEN265.html

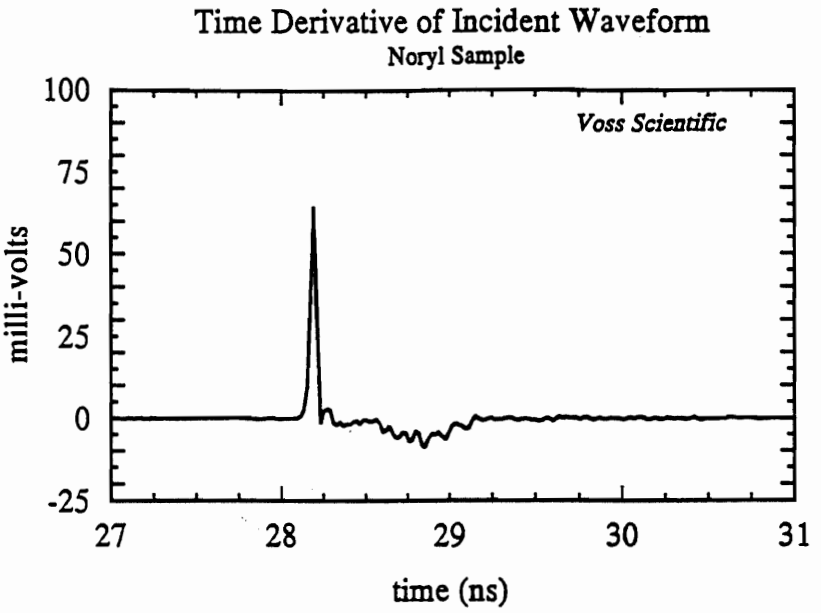

(a)

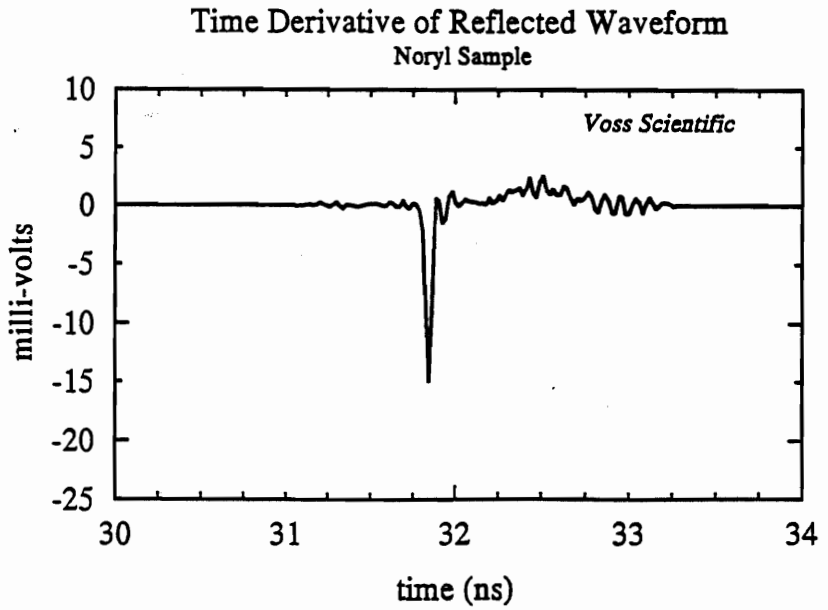

(b)

Figure 8. **The waveforms submitted to the Materials Characterization Data Reduction Module: (a) time derivative of the incident; (b) first component of the reflected;**

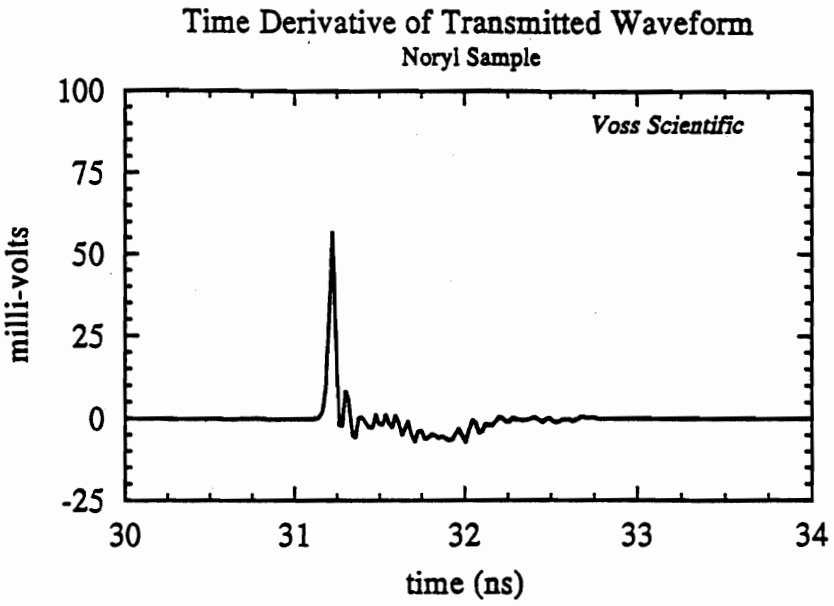

(c)

Figure 8. **The waveforms submitted to the Materials Characterization Data Reduction Module: and (c) first component of the transmitted waveforms associated with the Noryl sample.**

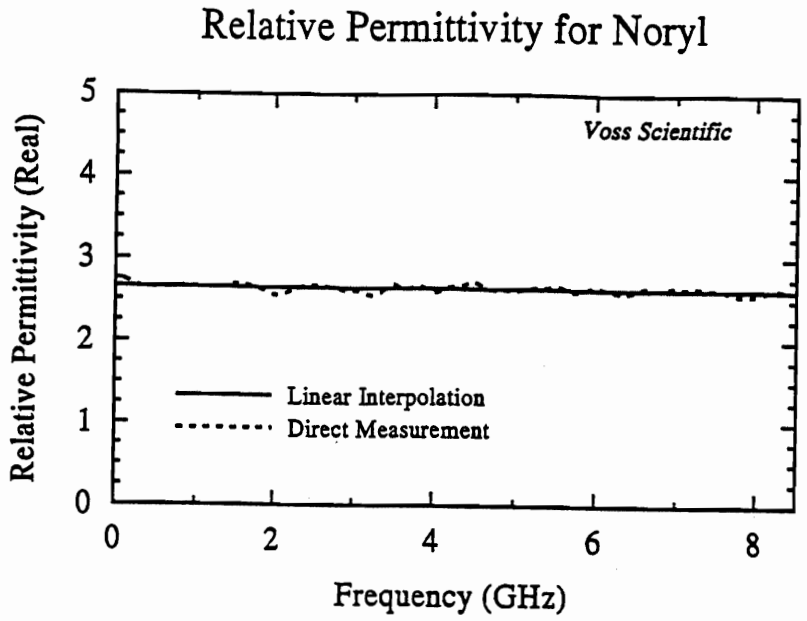

(a)

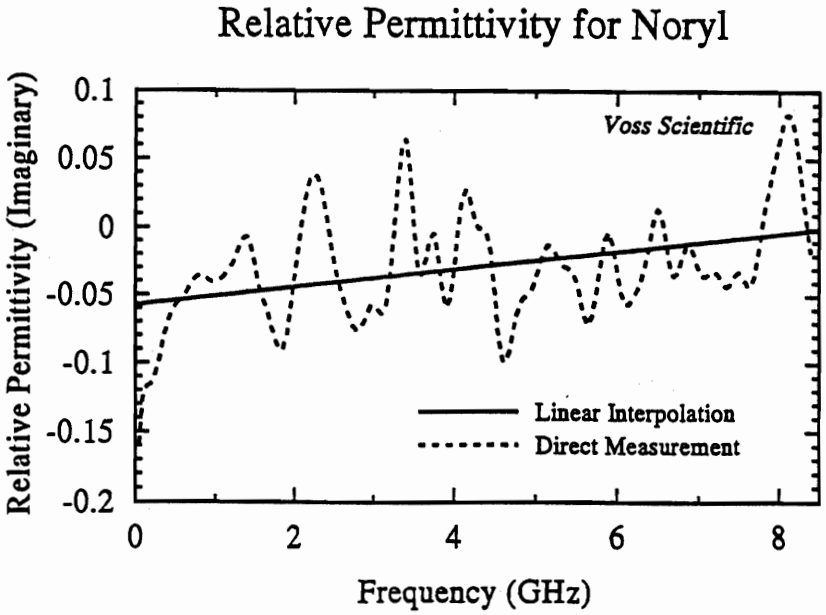

(b)

Figure 9. **Reduced values of relative permittivity and permeability for Noryl (GE EN265): (a) real component of the relative permittivity; (b) imaginary component of the relative permittivity;**

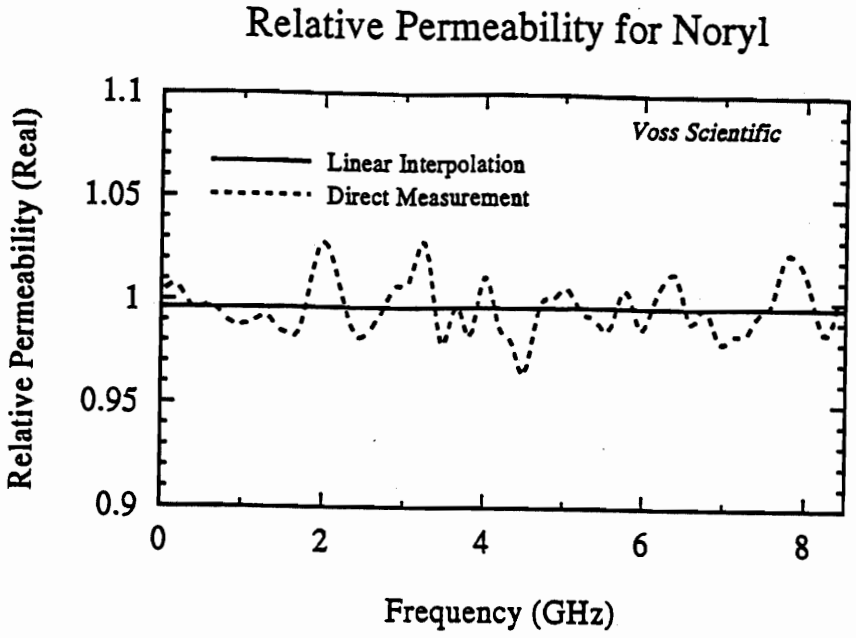

(c)

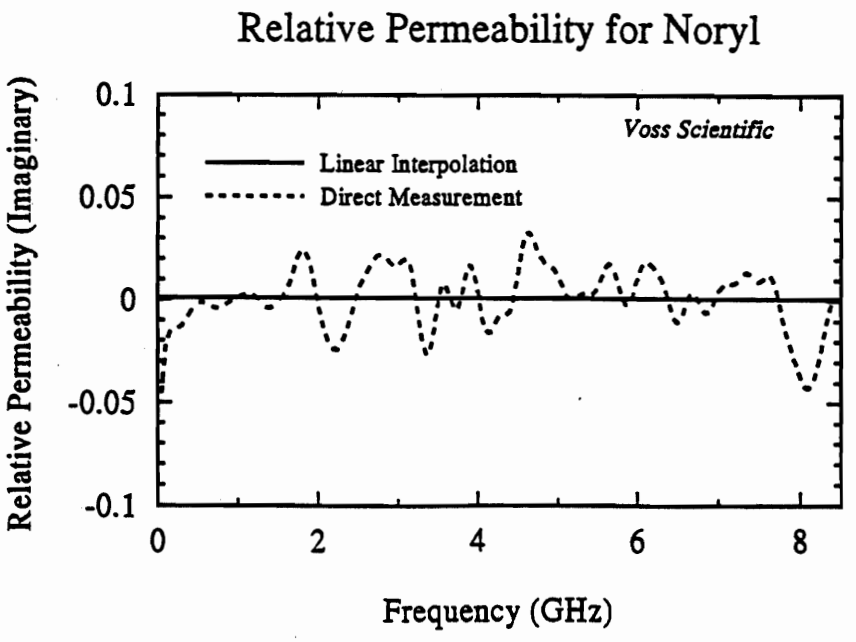

(d)

Figure 9. **Reduced values of relative permittivity and permeability for Noryl (GE EN265): (c) real component of the relative permeability; and (d) imaginary component of the relative permeability.**

V.2. Measurement of Two Concrete Samples

Two concrete samples cut from a poured concrete slab and fabricated to the proper dimensions. The lengths of the two samples were $L_1 = 6.000$ and $L_2 = 6.003$ inches. In the same manner as described earlier, the time derivatives of the incident, reflected and transmitted waveforms were measured. The incident, and first components of the transmitted and reflected waveforms associated with Concrete Sample No. 1 are shown in Figure 10. The samples lengths, transit times, and measured waveforms were submitted to the reduction software. The reduced values of relative permittivity and permeability for the two concrete samples are given in Figures 11a-d and 12a-d for the frequency range 50 MHz - 8 GHz.

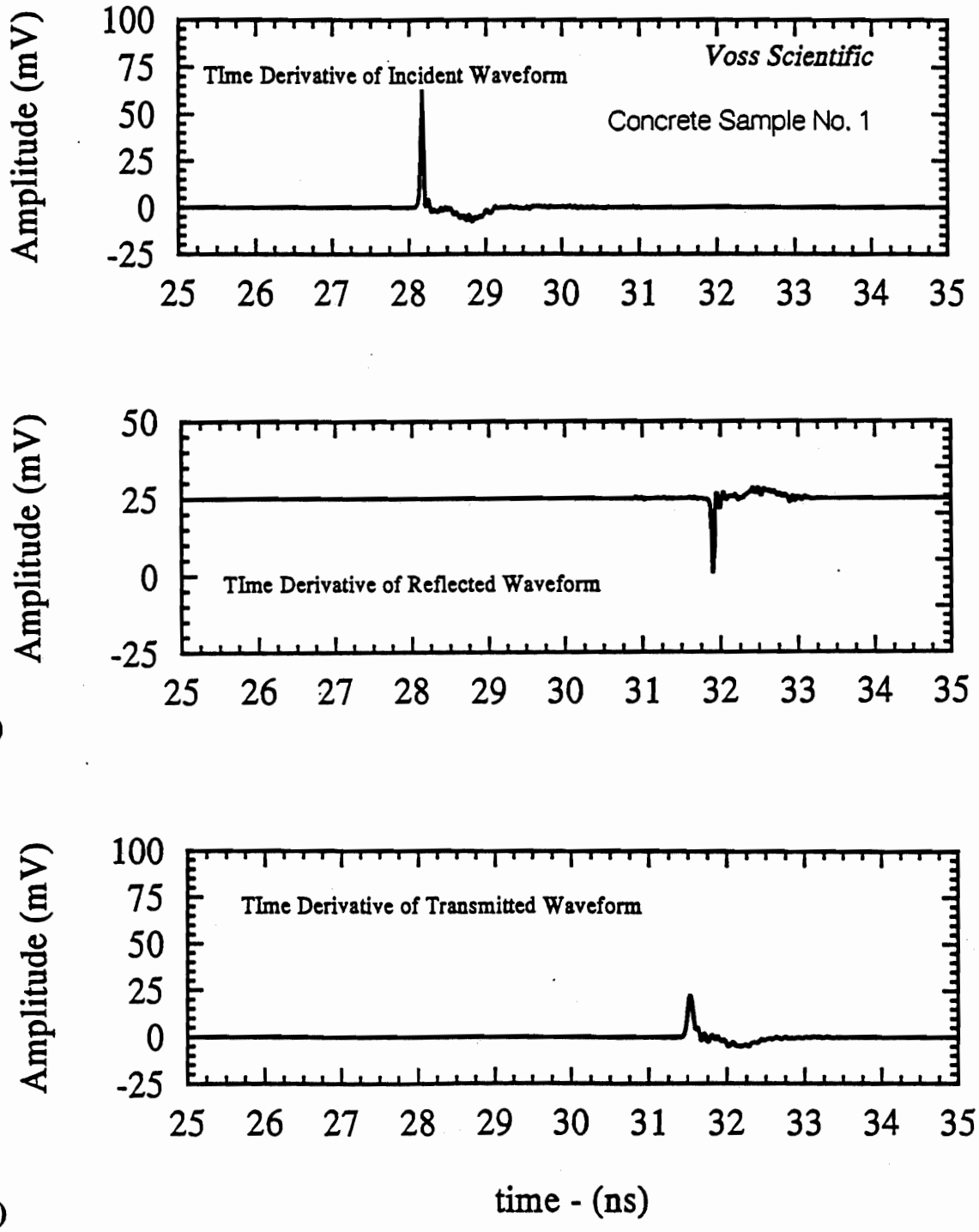

Figure 10. **The waveforms submitted to the Materials Characterization Data Reduction Module: (a) time derivative of the incident; (b) first component of the reflected; and (c) and first component of the transmitted waveforms associated with Concrete Sample No. 1.**

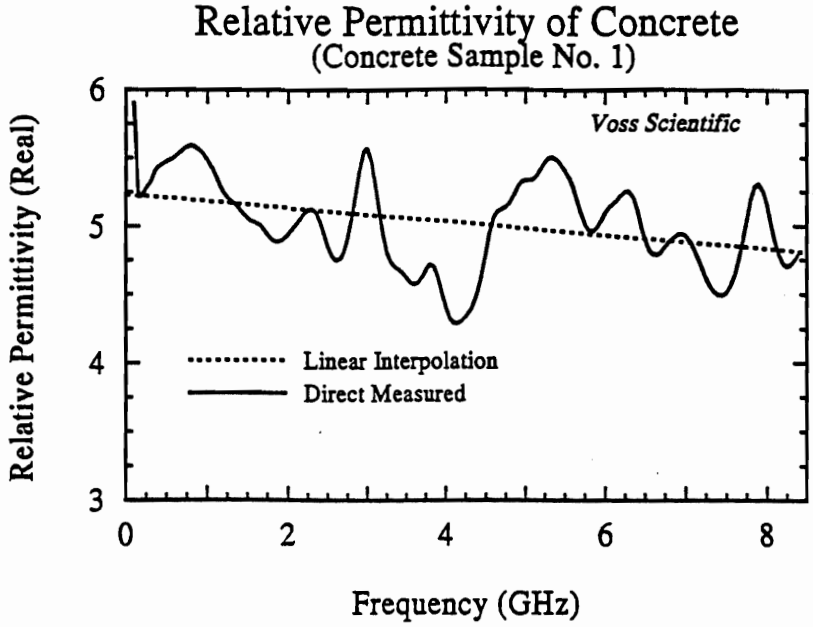

(a)

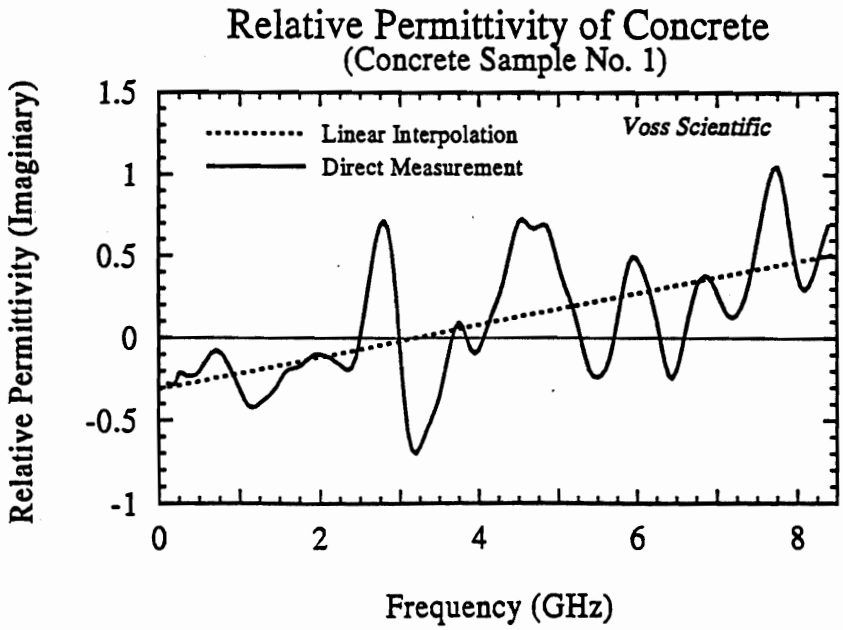

(b)

Figure 11. Reduced values of relative permittivity and permeability for Concrete Sample No. 1: (a) real component of the relative permittivity; (b) imaginary component of the relative permittivity;

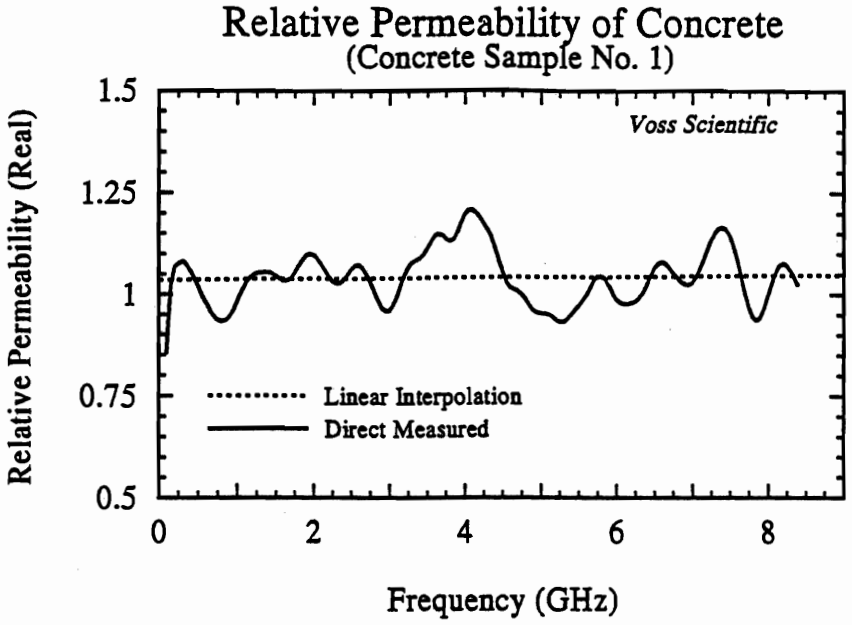

(c)

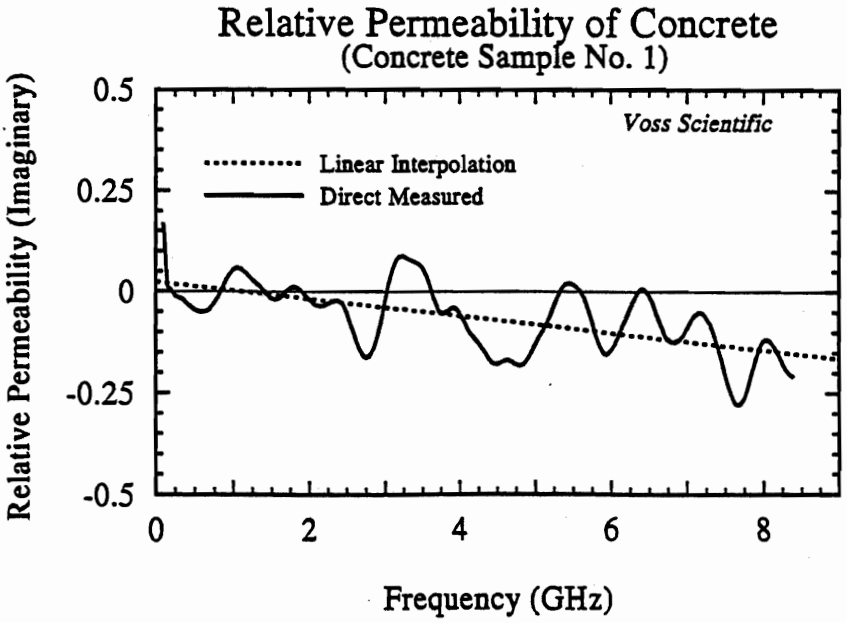

(d)

Figure 11. **Reduced values of relative permittivity and permeability for Concrete Sample No. 1: (c) real component of the relative permeability; and (d) imaginary component of the relative permeability.**

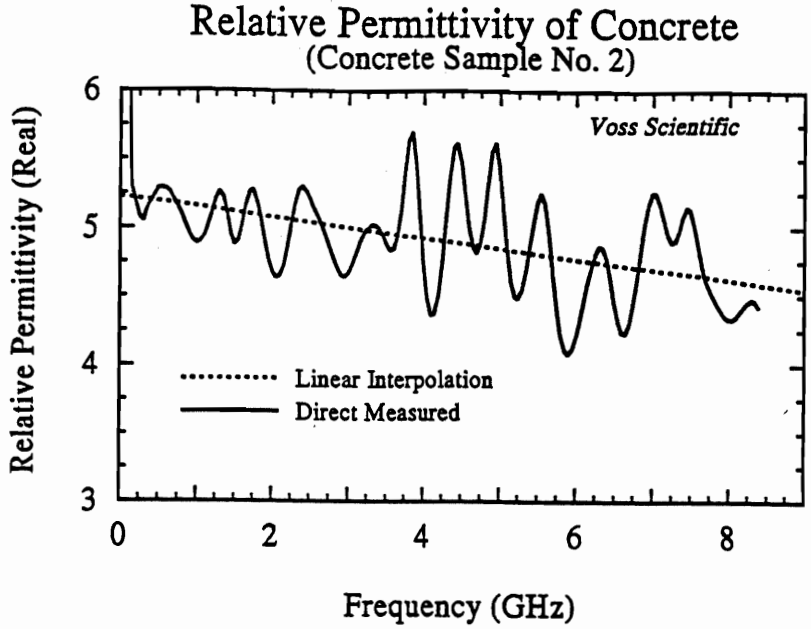

(a)

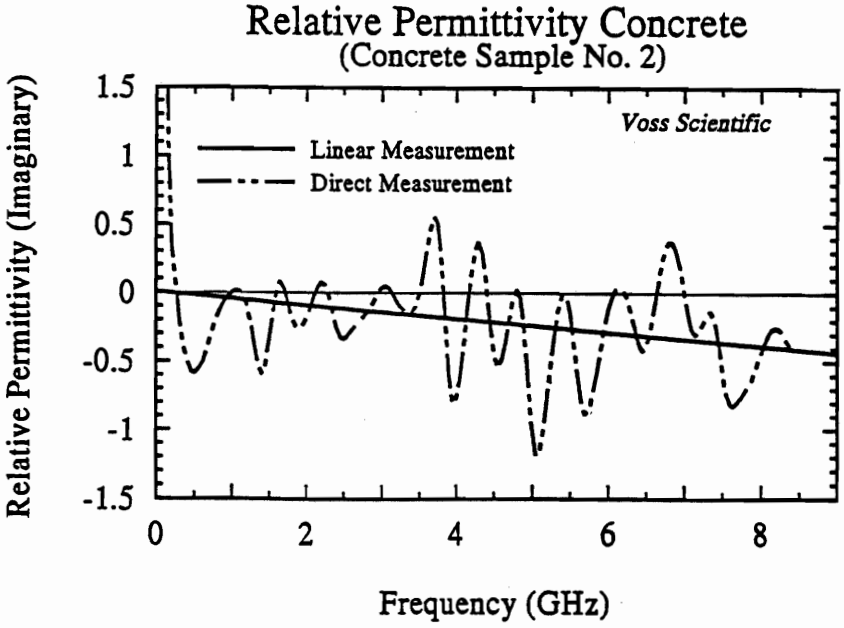

(b)

Figure 12. Reduced values of relative permittivity and permeability for Concrete Sample No. 2: (a) real component of the relative permittivity; (b) imaginary component of the relative permittivity;

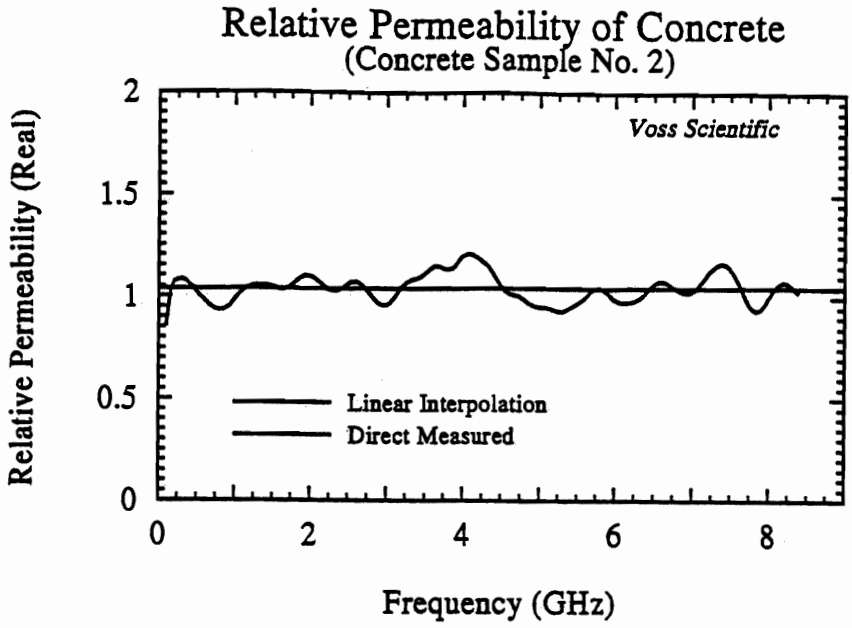

(c)

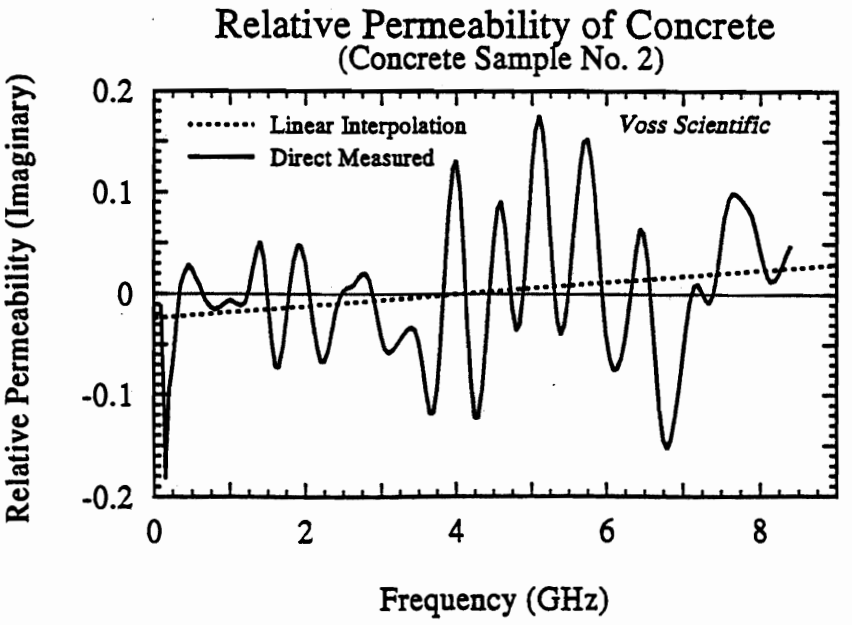

(d)

Figure 12. **Reduced values of relative permittivity and permeability for Concrete Sample No. 2: (c) real component of the relative permeability; and (d) imaginary component of the relative permeability.**

V.3. Measurement of Polyvinyl Chloride (PVC)

Polyvinyl chloride (PVC) is a common plastic with many uses and its electrical properties are well known (in certain frequency regimes). A PVC sample (exact variety unknown) was made, and its electrical characteristics measured. The reduced values of relative permittivity and permeability for the PVC material are given in Figures 13a-d for the frequency range 50 MHz - 8 GHz. Again, both the raw measured data and a linear interpolation are given on each graph. One sees that the real part of the relative dielectric constant is essentially constant over the band ($\varepsilon_r' \approx 2.75$), while the imaginary (loss) component varies from $-0.20 < \varepsilon_r'' < 0$ over the frequency band. Figures 11c and d show the PVC is a non-magnetic material with $\mu_r' \approx 1.0$ and $\mu_r'' \approx 0.0$. The fact that the graph shows $\mu_r'' > 0.0$ is non-physical.

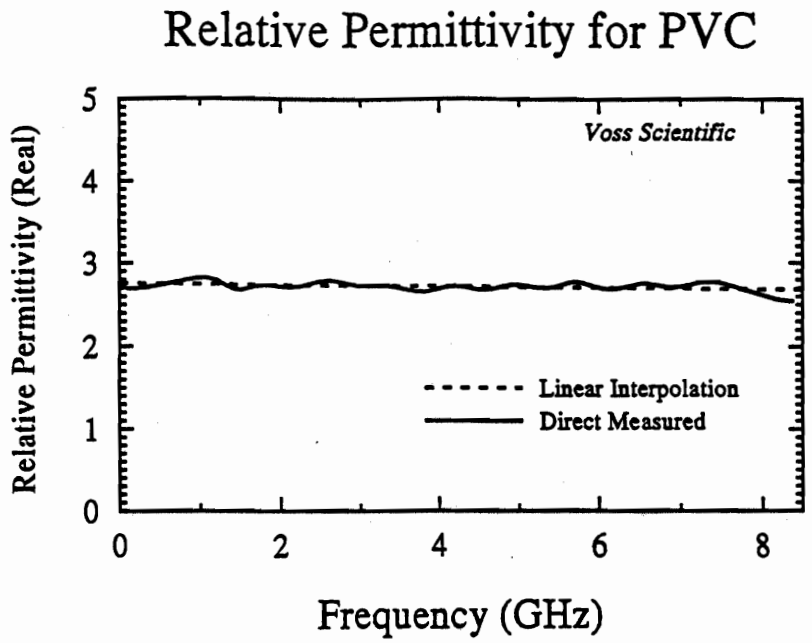

(a)

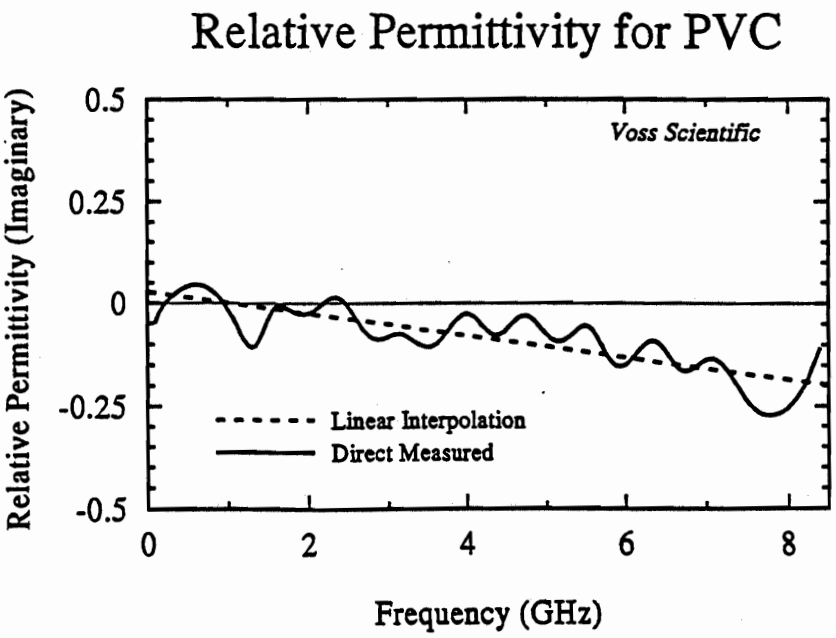

(b)

Figure 13. Reduced values of relative permittivity and permeability for Polyvinyl Chloride (PVC): (a) real component of the relative permittivity; (b) imaginary component of the relative permittivity;

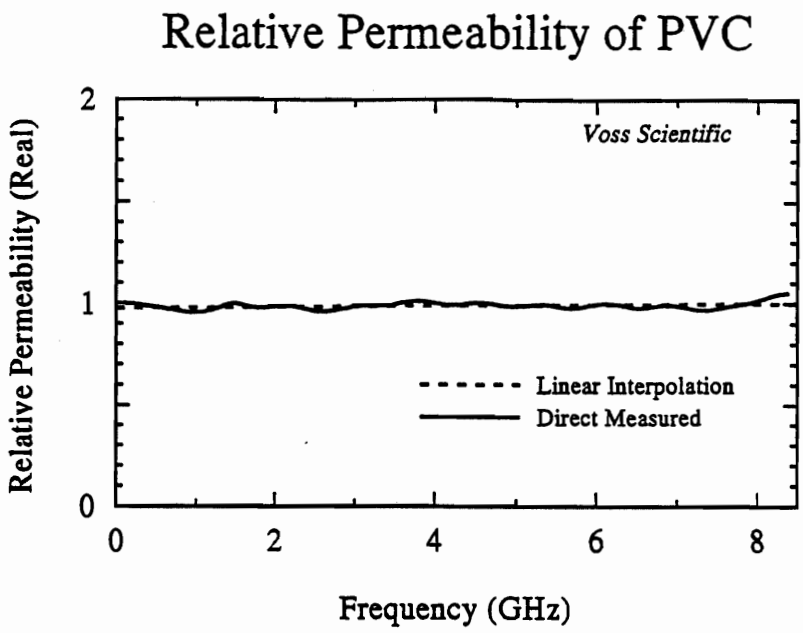

(c)

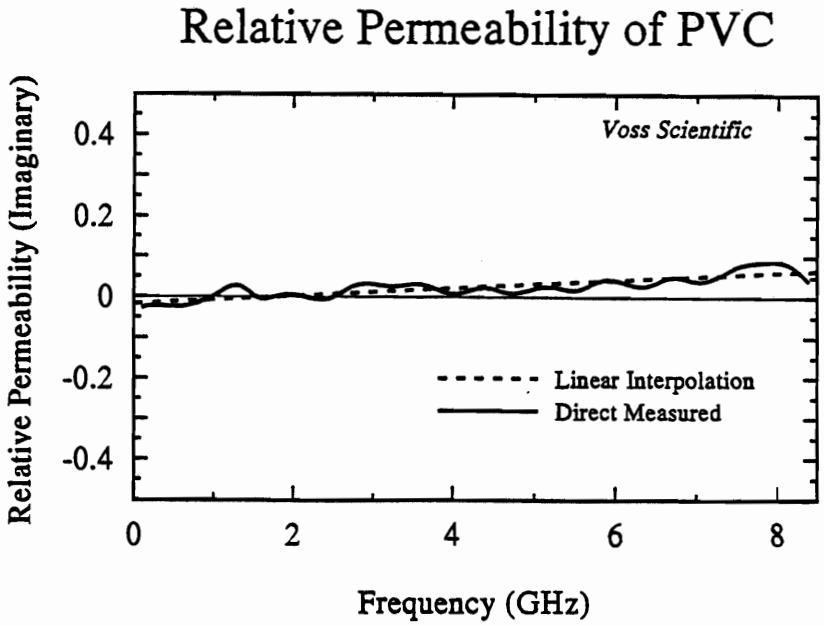

(d)

Figure 13. Reduced values of relative permittivity and permeability for Polyvinyl Chloride (PVC): (c) real component of the relative permeability; and (d) imaginary component of the relative permeability.

VI. Frequency-Domain Measurement of the Properties of Materials

Time domain measurements, as described in the previous sections, have many advantages. First, the incident, reflected and transmitted signals are measured directly. Direct knowledge of their characteristics are measured. This eliminates the need to assume the transmission line behaves in a certain manner (loss, electrical length, etc.), and requires no calibration procedure, but there are disadvantages as well. For one, the sample length must be large to ensure time isolation of the different signal components. Furthermore, several measurements must be made (waveform measurements, timing and/or distance measurements), and parts of the waveform processing are arbitrary. Frequency domain measurement techniques overcome some of these disadvantages. The sample sizes are not governed by clear time considerations, and in theory calibration procedures can provide extremely accurate measurements. This section describes the coaxial line frequency domain measurement and data reduction techniques explored in this effort.

VI.1. Transmission and Reflection Frequency-Domain Measurements, and the Determination of the Properties of Materials

In general, two independent measurements are required to determine both complex permittivity and permeability of a material. These independent measurements can be simply the transmission (s_{21}) and reflection (s_{11}) scattering parameters one obtains from a vector network analyzer-based frequency domain measurement. Once one has the scattering parameter values, the reduction to the material properties is accomplished in the same manner detailed in Section II.2.

VI.1.1. Calibration and Measurement Procedure

The calibration of the vector network analyzer (VNA), typically an HP8510 or equivalent, typically would be conducted at the connector interfaces (AA and DD as shown in Figure 14 below).

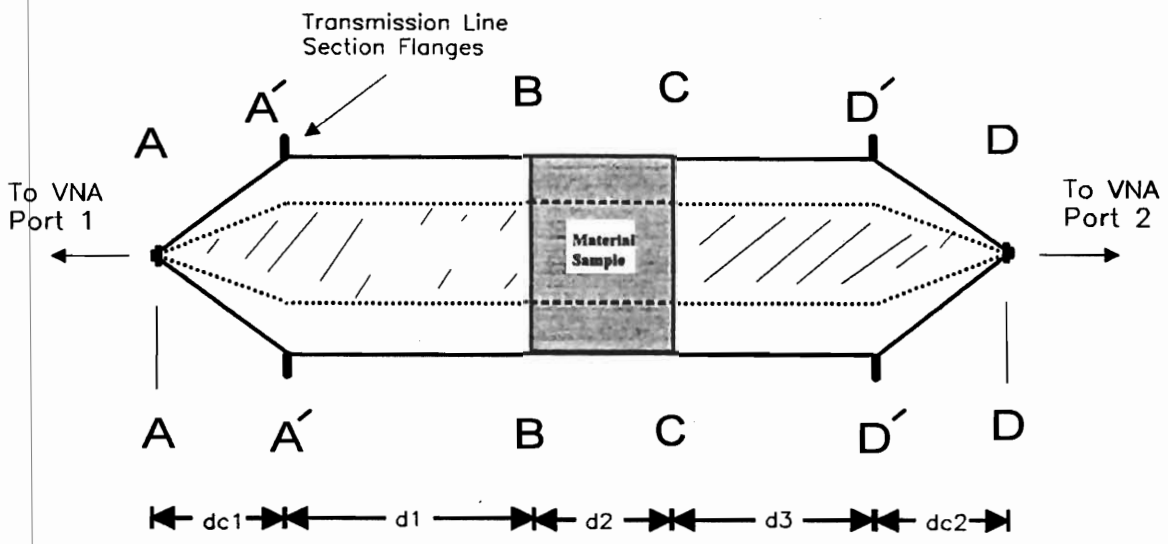

Figure 14. The measurement and calibration interfaces of the coaxial transmission line are shown.

However, if one wished to rigorously account for the dispersive effects of the cones (transition sections between the small diameter of the coaxial cable and the large diameter cross section of the test fixture), then the calibration planes should be moved forward to A' and D'. Unfortunately, the termination standards needed to perform the calibration at this plane do not exist. We could do a simple reflection calibration (using a short circuit plane), but this will not yield the required accuracy. Consequently, a full 2-port calibration is performed at the planes A and D.

With the calibration made, the sample is placed in the sample holder. Record is made of the distances d_1, d_2, and d_3, and the scattering parameters s_{21} and s_{11} are recorded. To determine the material properties, these values next need to be transformed to the sample interfaces. The relations governing this transformation are

$$s_{11}(\omega)|_{A'A'} = s_{11}(\omega)|_{AA}\, e^{+j2\beta_1(d_{c1}+d_1)}, \qquad \text{(VI.1a)}$$

and

$$s_{21}(\omega)|_{D'D'} = s_{21}(\omega)|_{DD}\, e^{+j\beta_1(d_{c1}+d_1+d_3+d_{c2})}. \qquad \text{(VI.1b)}$$

These transformed values of the scattering parameters are then reduced to material characteristics in the manner described in Section II.2.

VI.1.2. Measurement Calibration and Measurement Procedure

To demonstrate the frequency domain measurements and data reduction techniques described above, a 1.02 inch Nylon sample was placed in the line and the scattering parameters measured. The real, imaginary and complex values of the scattering parameters, referenced planes A and D are shown in Figures 15a and b. The index j is the sample number, the relation between the sample number and the frequency is:

$$f_j = \frac{(5-.045)}{800} j + .045\ GHz\ . \qquad \text{(VI.2)}$$

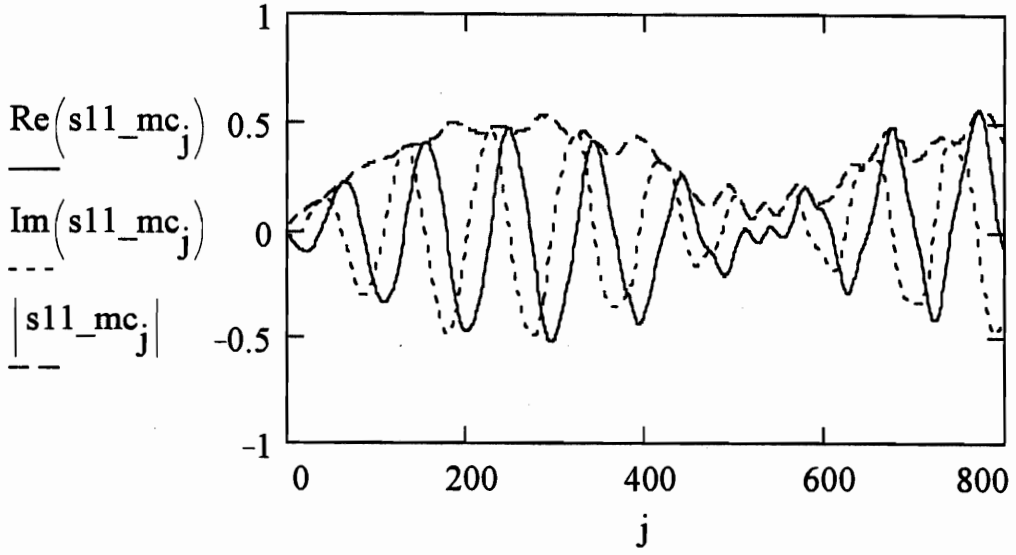

(a)

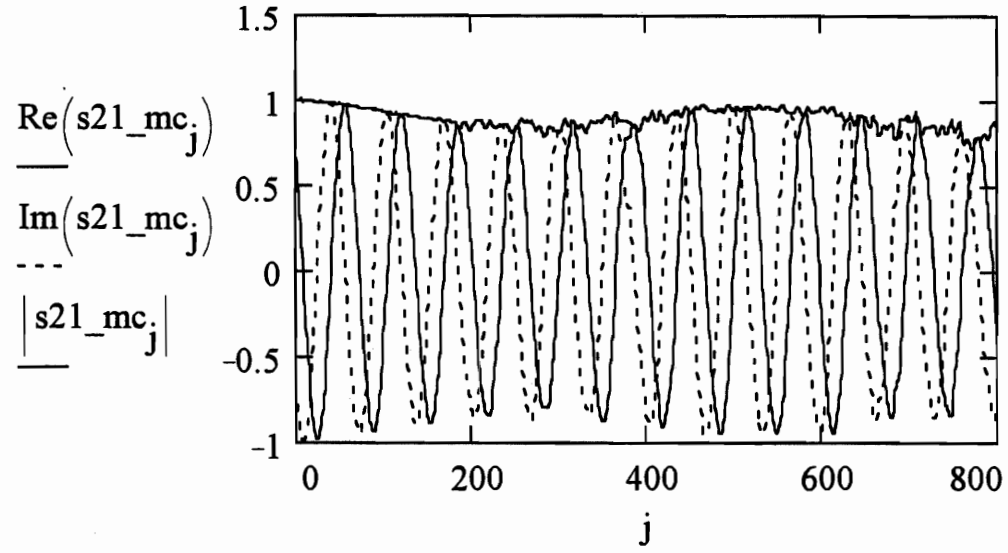

(b)

Figure 15. Measured scattering parameters referenced to planes A and D: (a) real and imaginary components, and magnitude of the s_{11} scattering parameter; and (b) real and imaginary components, and magnitude of the s_{21} scattering parameter.

Transformed in the manner described by Eqn VI.1, these values become as shown in Figure 16 below.

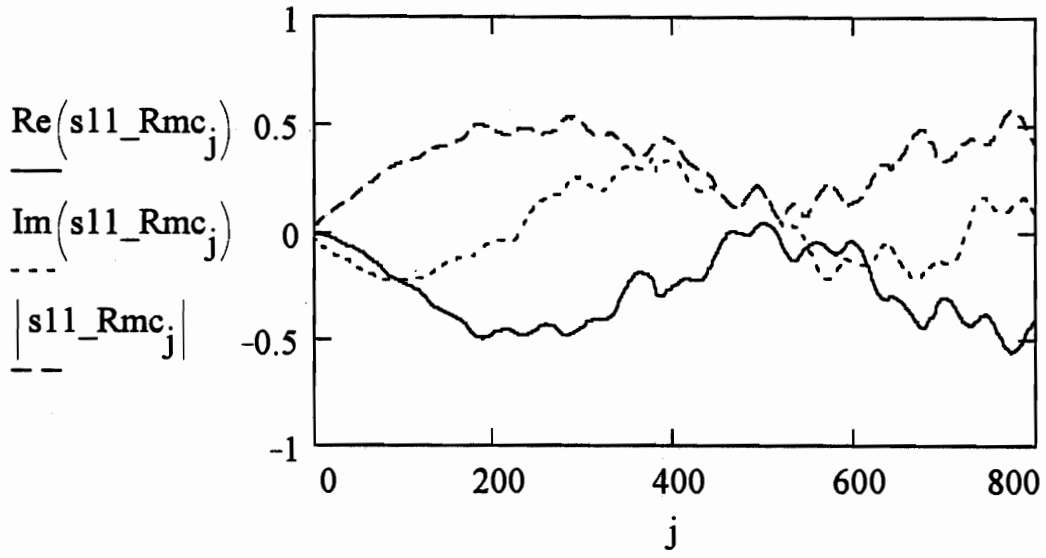

(a)

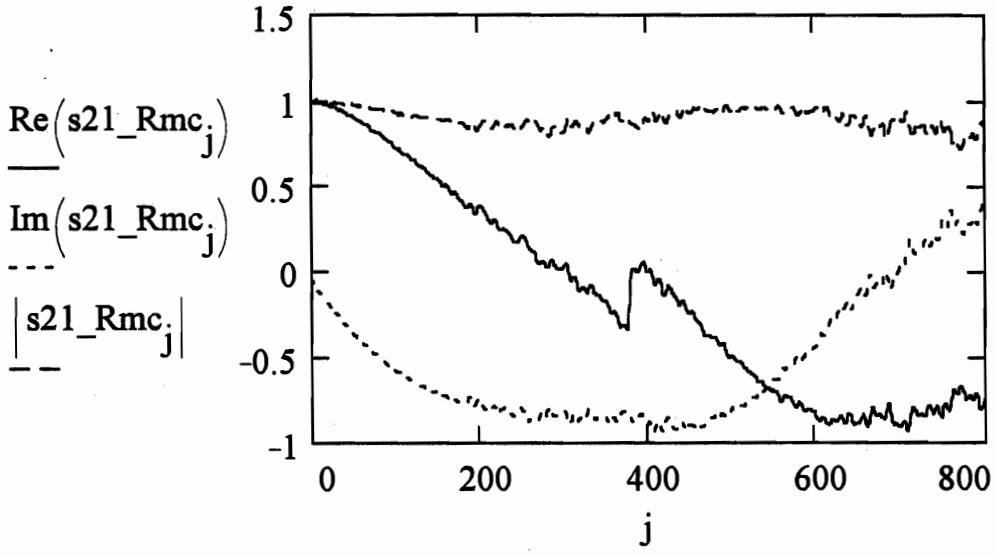

(b)

Figure 16. Measured scattering parameters referenced to planes A' and D': (a) real and imaginary components, and magnitude of the s_{11} scattering parameter; and (b) real and imaginary components, and magnitude of the s_{21} scattering parameter.

These values of the scattering parameters were reduced in the manner described in Section II.2. The material characteristics derived are as shown in Figure 17.

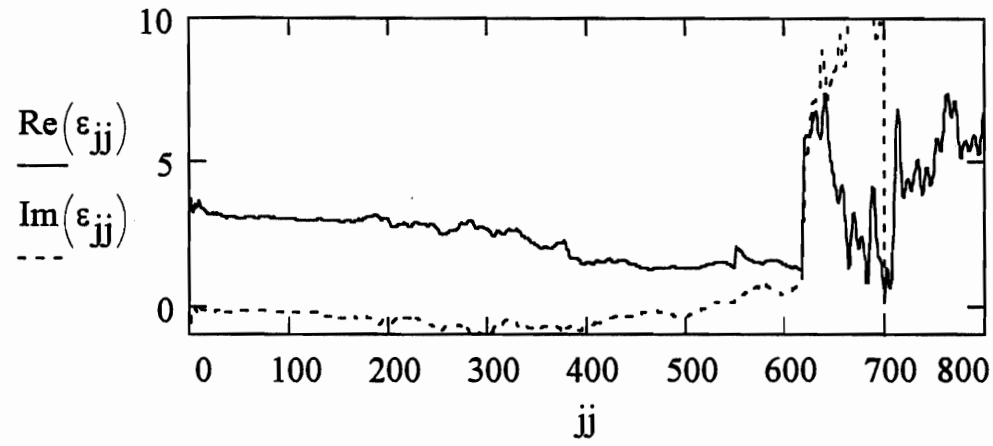

(a)

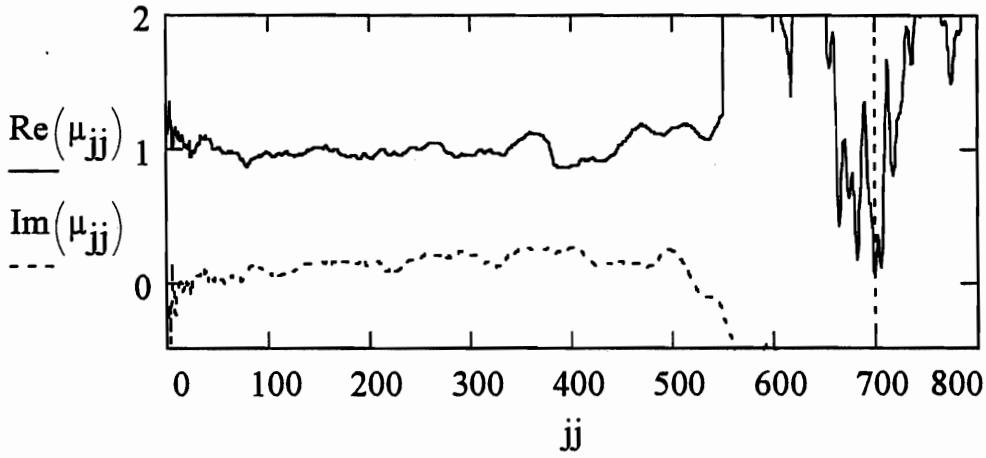

(b)

Figure 17. Measured values of the complex permittivity and permeability of Nylon (specific type unknown): (a) real and imaginary components of the relative permittivity; and (b) real and imaginary components of the permeability.

The material values at selected frequencies of interest are summarized in Table 6.1 below. One notes that for measurements made below $f < 2.5$ GHz, the materials characteristics found are in the range with the published values of Nylon. Measurements at frequencies above this value tended to yield unreasonable values. This could be because the line itself will allow higher order modes, the next allowable mode happens about

$$f_{\substack{Higher\\Order\\Mode}} = \frac{3\times10^8}{\pi(2.7+1.6)}\frac{(100)(2)}{2.54}\frac{1}{10^9} = 1.8\ GHz\,. \qquad \text{(VI.3)}$$

The effects of slight overmoding and the slightly dispersive effects of the line were not calibrated out (note the extreme discontinuity in the transmission coefficient shown in Figure 16). Furthermore, the loss values for both the permittivity and the permeability seem high. This could be due to the loss in the metal surfaces of the coaxial test fixture itself.

VI.2. Reflection Frequency-Domain Measurements, and the Determination of the Properties of Materials

The transmission and reflection measurements required of the previous method were oftentimes difficult to record with the required precision. Equations II.4 show that the reduction requires rather involved expressions involving both the transmission and scattering parameters. This can result in reduced data that becomes meaningless (as shown in the previous section), especially at the higher frequencies where the correlation between s_{11} and s_{21} is harder to maintain. If one can assume that the relative permeability

Table 6.1 **Measured values of Complex permittivity and permeability for a 1.02 inch sample of Nylon determined from frequency domain transmission and reflection measurements. Recall that we defined the material parameters as:** $\varepsilon_r = \varepsilon_r' + j\varepsilon_r''$ **and** $\mu_r = \mu_r' + j\mu_r''$.

frequency (MHz)	$\varepsilon_r' = \mathrm{Re}(\varepsilon_r)$	$\varepsilon_r'' = \mathrm{Im}(\varepsilon_r)$	$\mu_r' = \mathrm{Re}(\mu_r)$	$\mu_r'' = \mathrm{Im}(\mu_r)$
50	3.24	-0.341	1.10	-0.16
100	3.41	-0.248	1.103	-0.164
250	3.081	-0.253	1.028	+0.062
500	3.065	-0.197	0.910	+0.0132
1000	2.88	-0.456	1.00	+0.145
1500	2.776	-0.562	0.960	+0.144
2000	2.458	-0.629	0.965	+0.149
2500	1.417	-0.8105	0.852	+0.244
3000	1.29	-0.243	1.14	+0.123

of the sample under test is 1 ($\mu_r = 1$), then a single reflection measurement can be used to determine the dielectric properties of the material.

VI.2.1. Theory of Frequency-Domain Reflection Measurements

Consider the geometry depicted in Figure 18. There a coaxial transmission line is shown with a sample material placed at the end of the line, with a short circuit termination. The reflection coefficient observed at the reference plane A (and the one we will ultimately measure) can be shown to be

$$\Gamma_{AA} = \frac{\tanh(j\beta_2 d_2) - \sqrt{\varepsilon_{r2}}}{\tanh(j\beta_2 d_2) + \sqrt{\varepsilon_{r2}}} e^{-j2\beta_0(d_1 + d_{c1})}. \qquad \text{(VI.4)}$$

where the propagation constant in the sample material is β_2, the material permittivity is ε_{r2}, and the sample length = d_2. This equation can be written in a slightly different form that better shows the dependence on the sample permittivity as follows

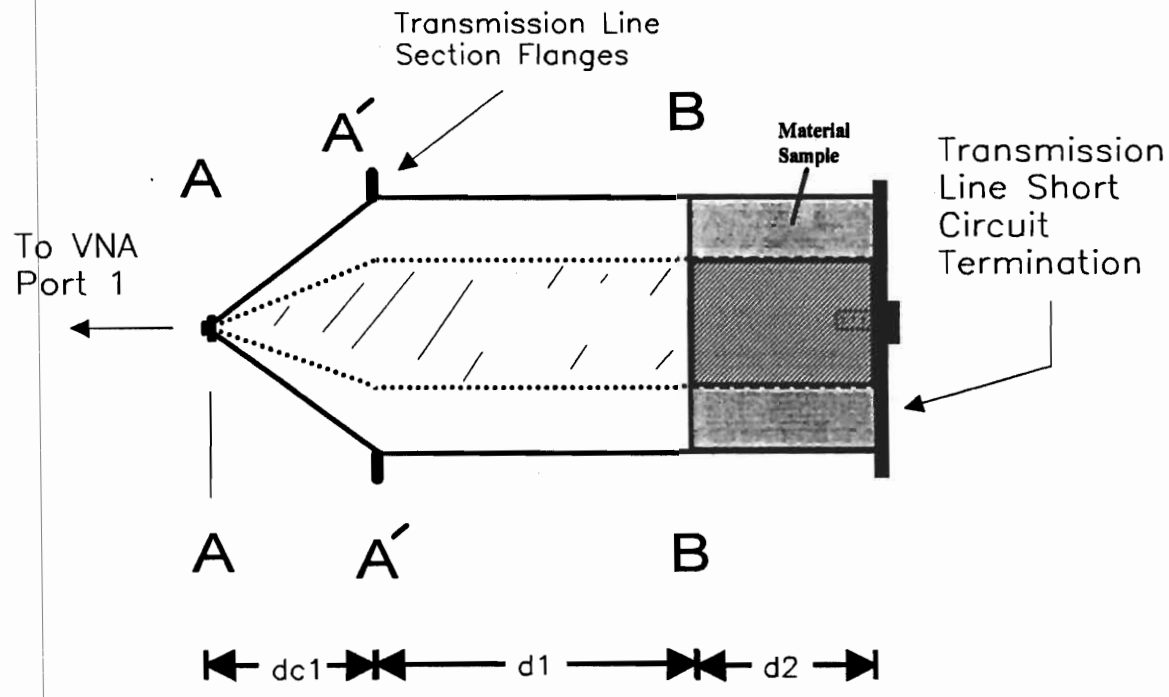

Figure 18. Coaxial test fixture loaded with a material sample. The sample resides with its rear interface coplanar with the end of the line. The coaxial line is terminated with a short circuit.

$$\sqrt{\varepsilon_{r2}} = j\tan\left(\frac{2\pi}{\lambda_0}\sqrt{\varepsilon_{r2}}d_2\right)\frac{1-\Gamma_{AA}e^{+j2\beta_0(d_1+d_{c1})}}{1+\Gamma_{AA}e^{+j2\beta_0(d_1+d_{c1})}}. \qquad \text{(VI.5)}$$

This is a transcendental equation in the unknown sample permittivity. A slight rearrangement

$$f\left(\varepsilon_{r2}\right) = \sqrt{\varepsilon_{r2}} - j\tan\left(\frac{2\pi}{\lambda_0}\sqrt{\varepsilon_{r2}}d_2\right)\frac{1-\Gamma_{AA}e^{+j2\beta_0(d_1+d_{c1})}}{1+\Gamma_{AA}e^{+j2\beta_0(d_1+d_{c1})}} = 0. \qquad \text{(VI.6)}$$

shows that the complex number that solves $f\left(\varepsilon_{r2}\right) = 0$ is the value of the sample permittivity. A complex root-finding solution was developed (see the discussion on the routine given in Section VI.2.3) to solve equations of this type. Note that the reflection coefficient in Eqn. VI.6 is expressed as its value at the plane A, but is multiplied by the exponential $e^{+j2\beta_0(d_1+d_{c1})}$ which transforms this value to the sample interface.

VI.2.2. Frequency-Domain Reflection Measurements and Reduction to Material Characteristics

A short circuit plate was fabricated to fit the coaxial line test fixture described in Section V. The material sample was then loaded into the rear of the test fixture, and the short circuit termination was secured in the manner depicted in Figure 18. Measures of the s_{11} scattering parameter (or reflection coefficient Γ_{AA}) where taken at the plane A, for the frequency range $0.05 \le f \le 5$ GHz. These complex values of the measured reflection coefficient for Concrete Sample No. 3 (length = 6.000 inches, small aggregate) are shown in Figure 19.

The frequency associated with the index (j) now is

$$f_j = \frac{(5-.05)}{800}j + .05\ GHz. \qquad \text{(VI.7)}$$

These values are transformed to the sample's front interface in the manner described above. The transformed reflection coefficient (the measured value multiplied by the exponential $e^{+j2\beta_0(d_1+d_{c1})}$ to transform its value to the sample interface) is shown in Figure 20.

These values were then used in equations of the form Eqn. VI.6 (one for each frequency), and the roots were determined. These roots correspond to the material permittivity, Figure 21 gives the material dielectric properties on Concrete Sample No. 3 found using this method.

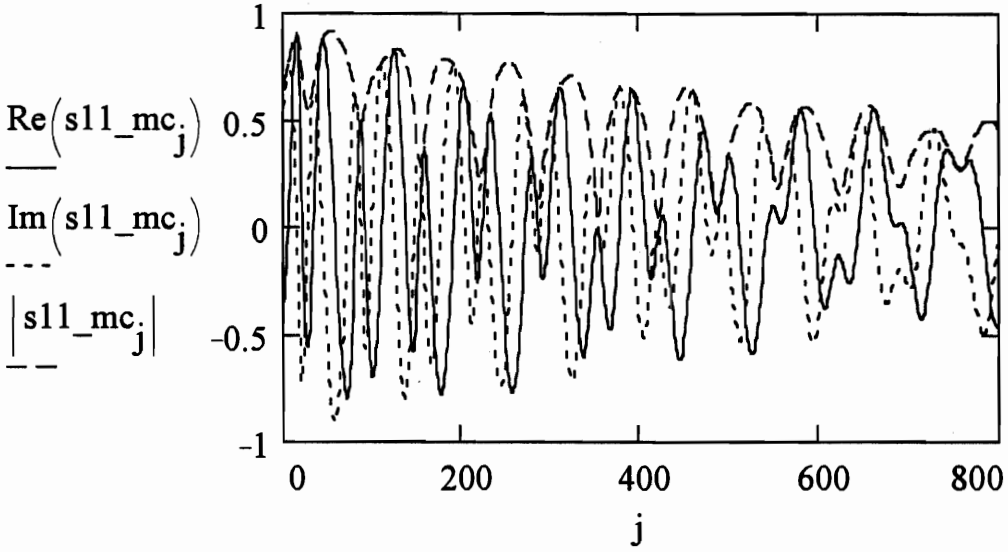

Figure 19. **Measured values at plane *A* of the complex reflection coefficient. The material sample was Concrete Sample No. 3 (length = 6.000 inches, small aggregate).**

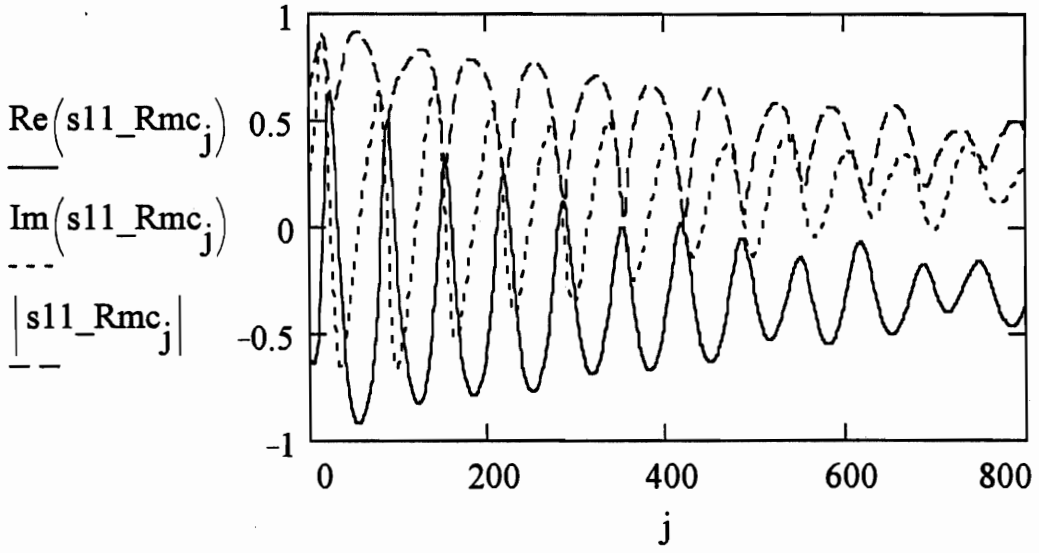

Figure 20. **Measured values at plane *B* (see Figure 18) of the complex reflection coefficient. The material sample was Concrete Sample No. 3 (length = 6.000 inches, small aggregate).**

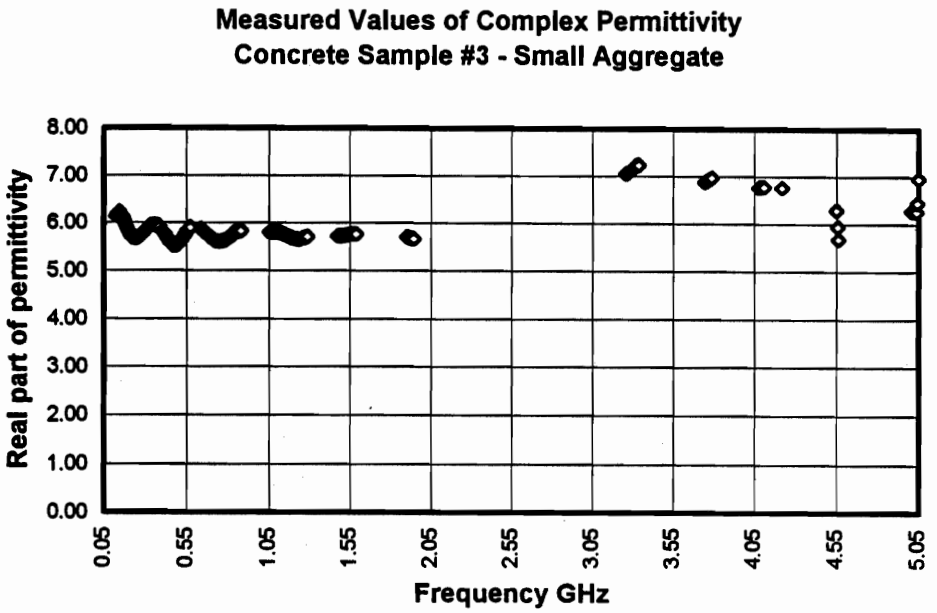

Figure 21a. **Measured values of the real part of the complex dielectric property of Concrete Sample No. 3 (length = 6.000 inches, small aggregate).**

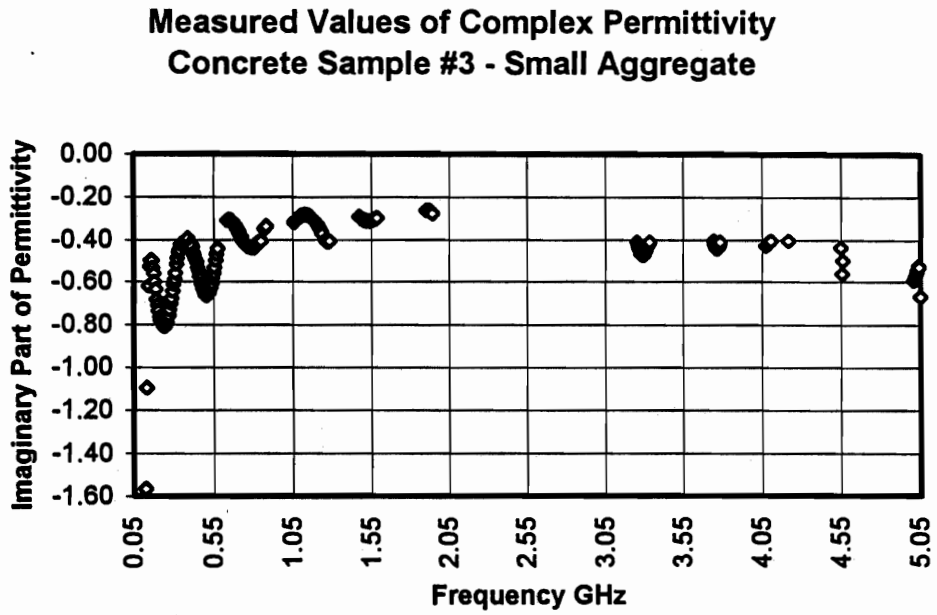

Figure 21b. **Measured values of the imaginary component of the complex dielectric property of Concrete Sample No. 3 (length = 6.000 inches, small aggregate).**

Table 6.2 **Measured values of Complex permittivity for a number of samples were made. The table below associates the figure that depicts its complex dielectric constant versus frequency determined from frequency domain reflection measurements.**

Material	Description	Figure
Concrete Sample No. 3	length = 6.000 inches, small aggregate	Figure 21
Concrete Sample No. 1	large aggregate	Figure 22
Lexan		Figure 23
Nylon		Figure 24
Polypropelyne		Figure 25
Polyvinyl Chloride (PVC)		Figure 26
NORYL		Figure 27
Air	empty line	Figure 28

The values of the complex dielectric constant were measured for a number of other material samples. These values are presented in the following figures. Table 6.2 associates the measured material with the figure that depicts its complex dielectric constant versus frequency.

VI.2.3. Roots of a Function of a Complex Variable

As described above, the short circuit measurement technique requires the location of the zero of a function of a complex variable. An algorithm to extract the complex root of a function, $f(z_0) = 0$, where $f(\cdot)$ is a function of a complex variable was developed. The procedure described in [Ref. 27] has been adapted and coded. As an example, consider the function

$$f(z) = e^{-z/2} - \sin(z). \qquad \text{(VI.8)}$$

This function was submitted to the root finding program, and the iterative results in the domain ($0.0 \le x \le 10.$, $-1.0 \le y \le 1.0$) were as follows:

Iteration Number	estimated root = z_0	$\left\|f(z_0)\right\| = \left\|e^{-z_0/2} - \sin(z_0)\right\|$
1	(9.68443, 0.325391)	1.0414e-07
2	(6.06314, -0.313165)	0.00165172
3	(3.21818, 0.34737)	6.57518e-08
4	(0.5, -0.25)	4.24282e-08

One notes good convergence to the correct value of the root after just four iterations. This routine was used with good success to find the complex roots of the governing equations of the short-circuit material permittivity measurement technique.

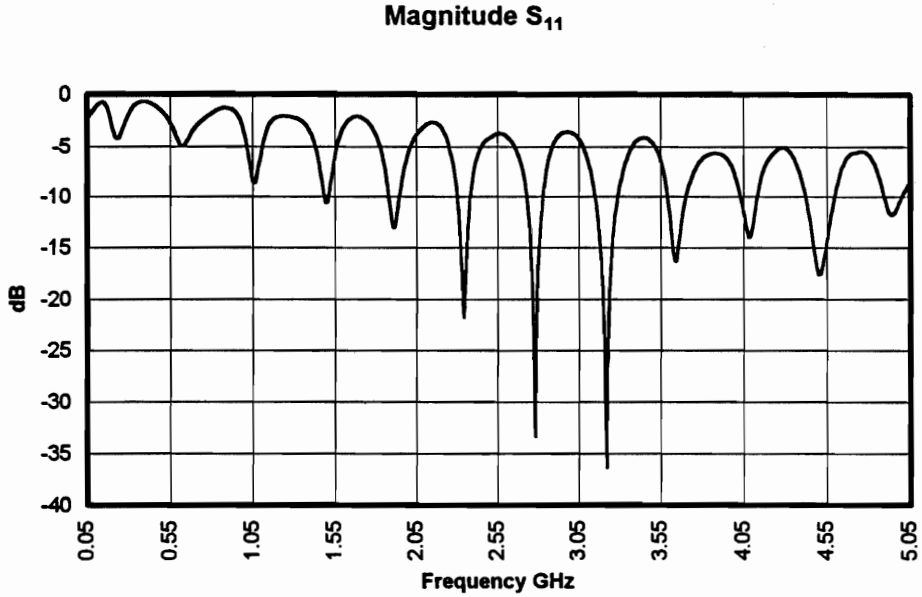

Figure 22a. Measured values of the magnitude of the complex reflection coefficient of Concrete Sample No. 1, large aggregate.

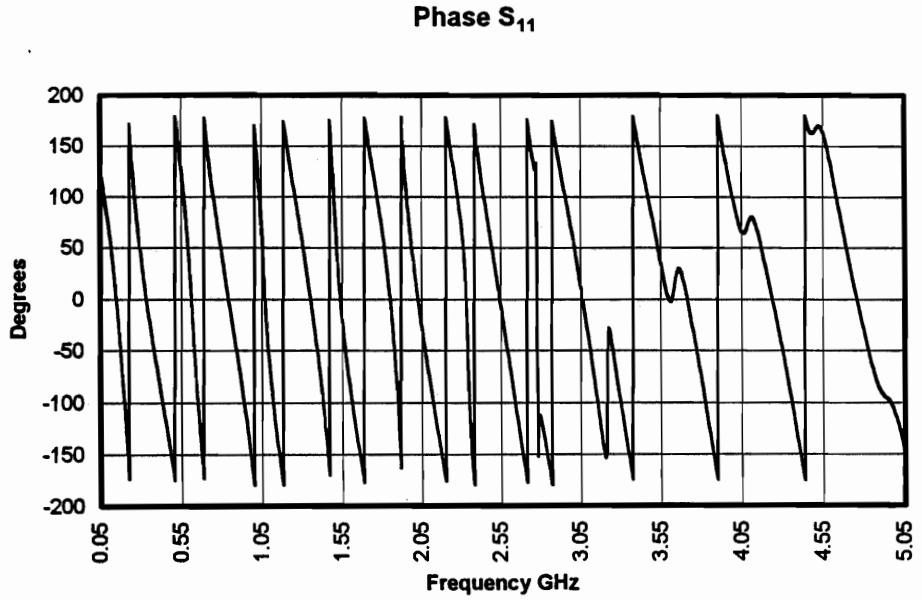

Figure 22b. Measured values of the phase of the complex reflection coefficient of Concrete Sample No. 1, large aggregate.

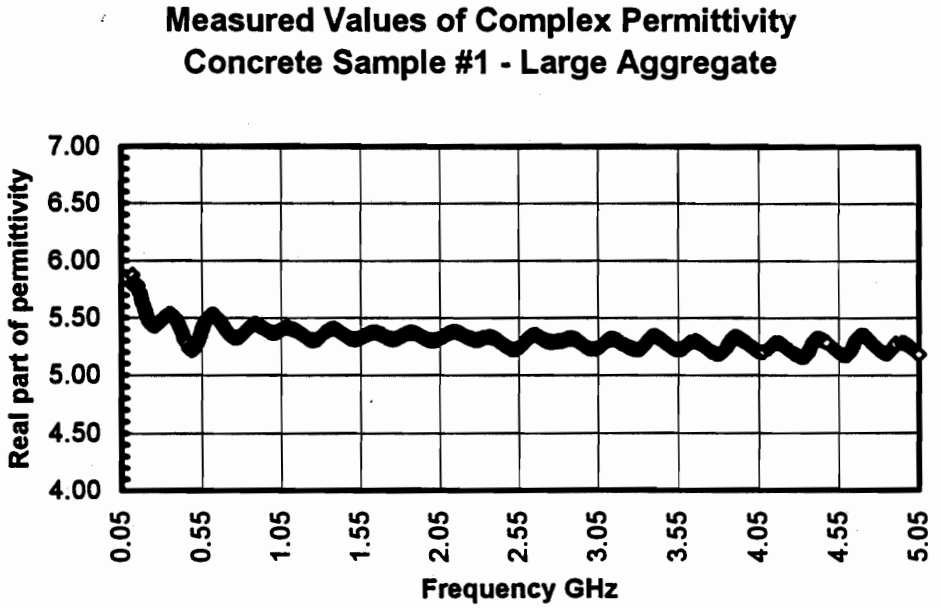

Figure 22c. **Measured values of the real part of the complex dielectric constant of Concrete Sample No. 1, large aggregate.**

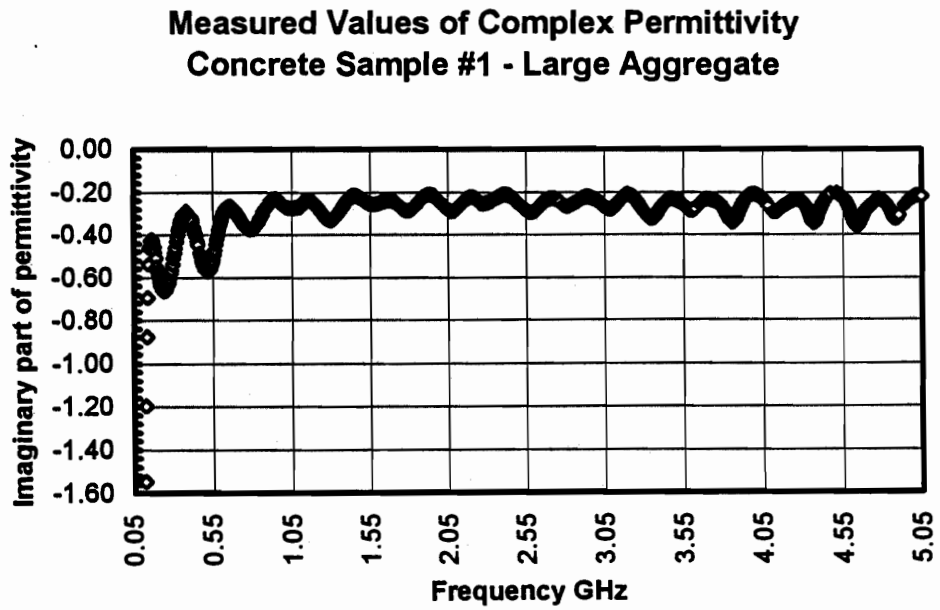

Figure 22d. **Measured values of the imaginary component of the complex dielectric constant of Concrete Sample No. 1, large aggregate.**

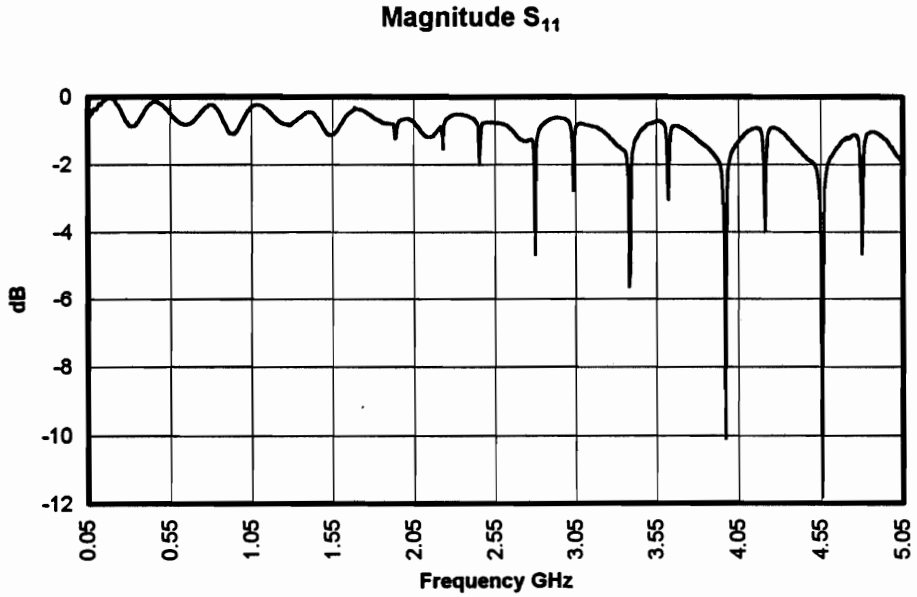

Figure 23a. Measured values of the magnitude of the complex reflection coefficient of Lexan.

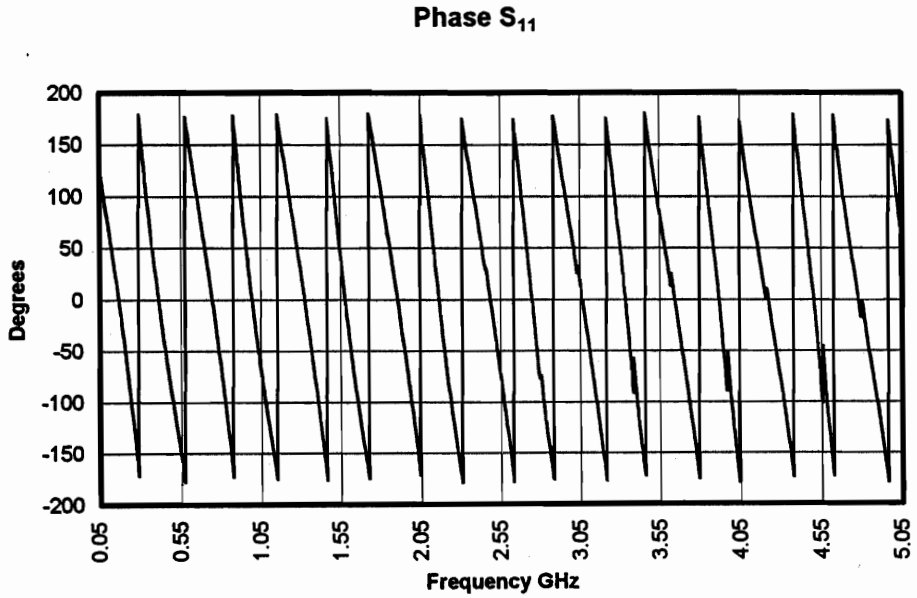

Figure 23b. Measured values of the phase of the complex reflection coefficient of Lexan.

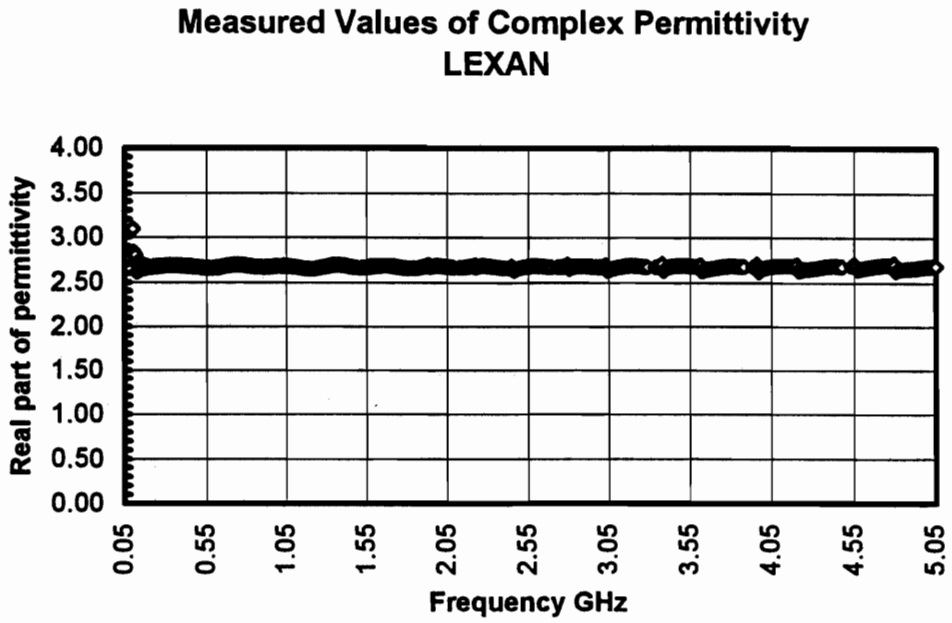

Figure 23c. **Measured values of the real part of the complex dielectric constant of Lexan.**

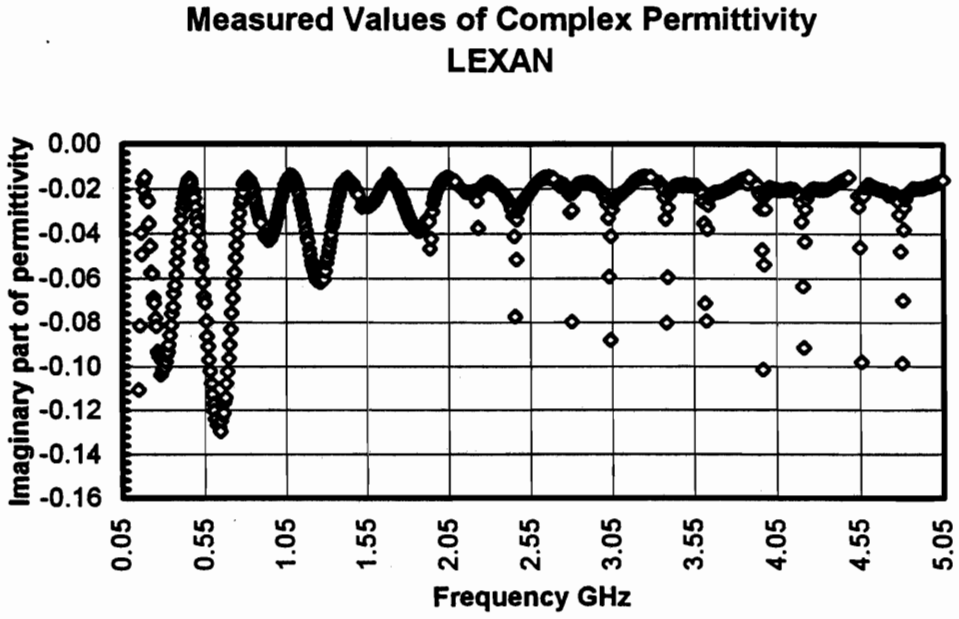

Figure 23d. **Measured values of the imaginary component of the complex dielectric constant of Lexan.**

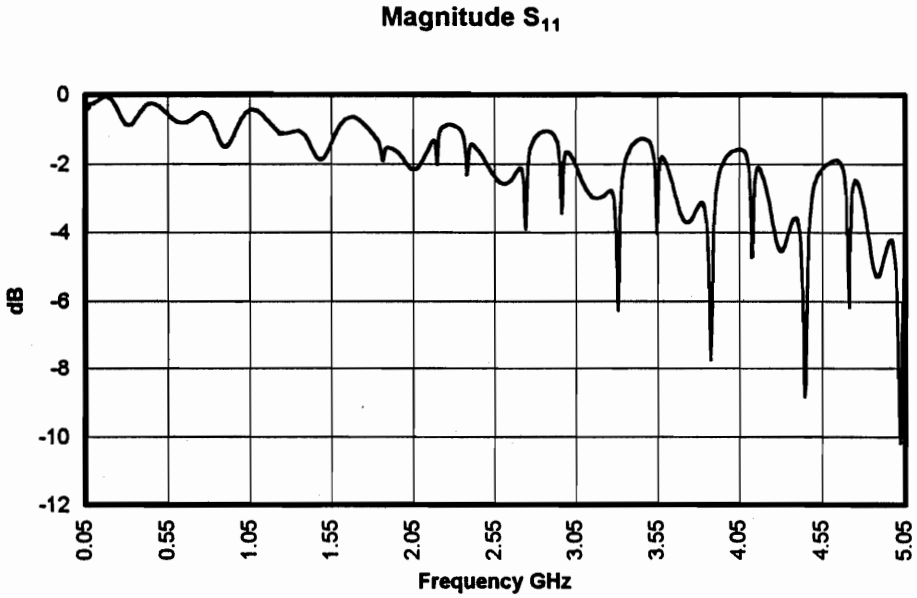

Figure 24a. Measured values of the magnitude of the complex reflection coefficient of Nylon.

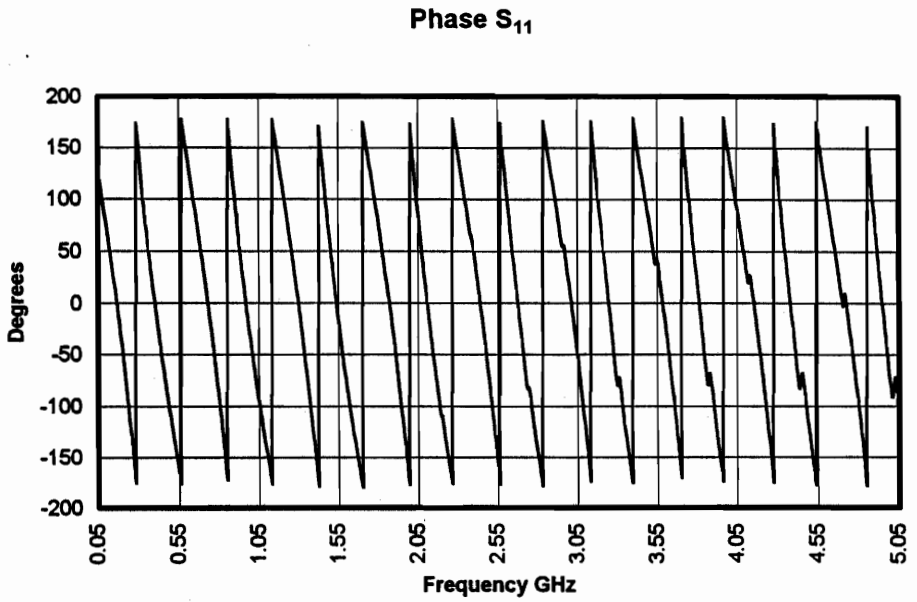

Figure 24b. Measured values of the phase of the complex reflection coefficient of Nylon.

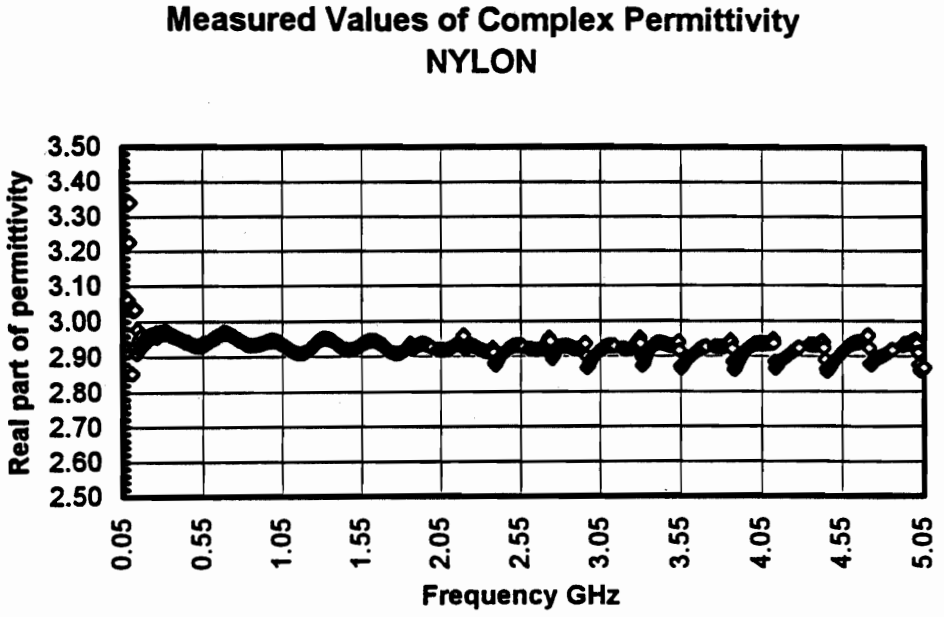

Figure 24c. **Measured values of the real part of the complex dielectric constant of Nylon.**

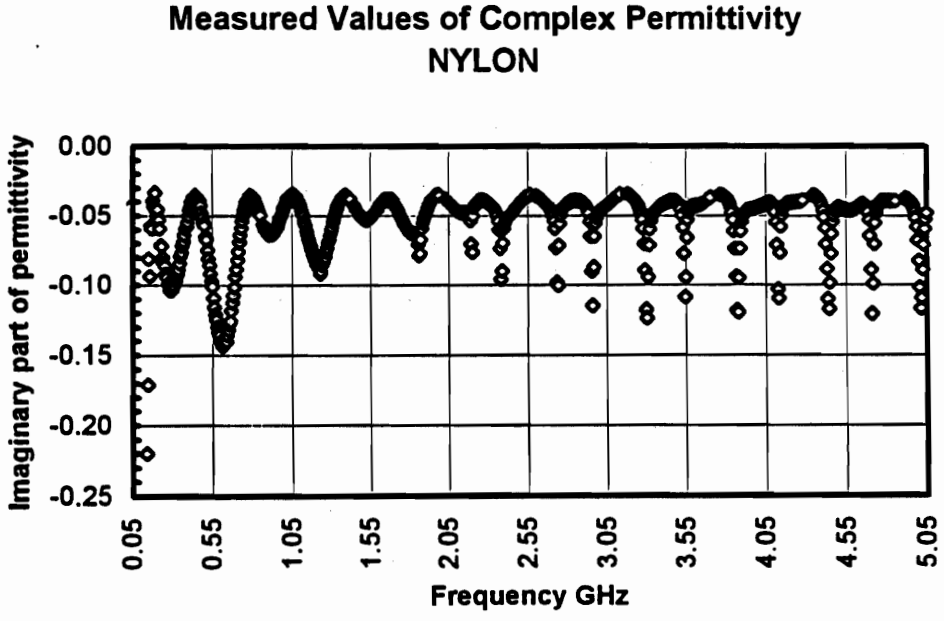

Figure 24d. **Measured values of the imaginary component of the complex dielectric constant of Nylon.**

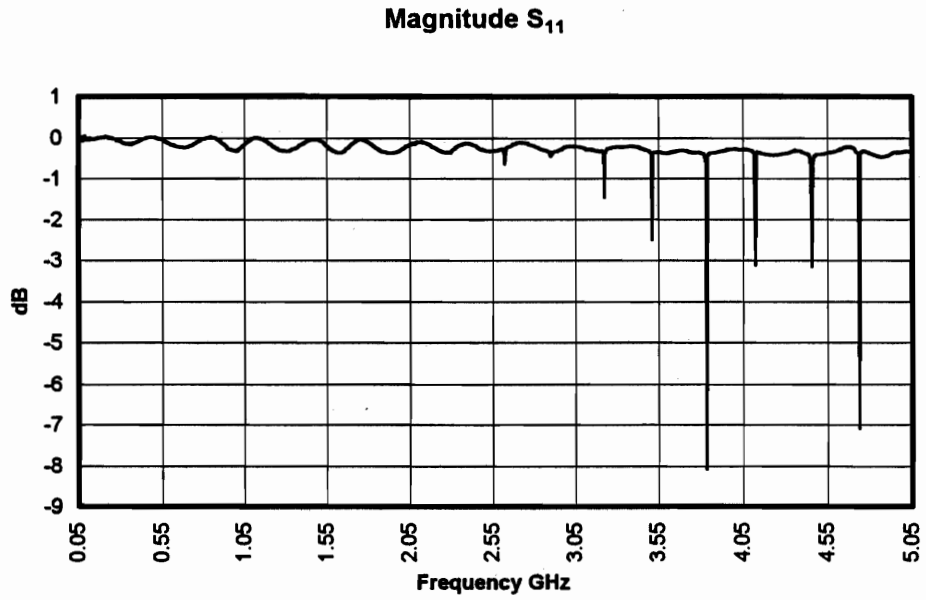

Figure 25a. Measured values of the magnitude of the complex reflection coefficient of Polypropylene.

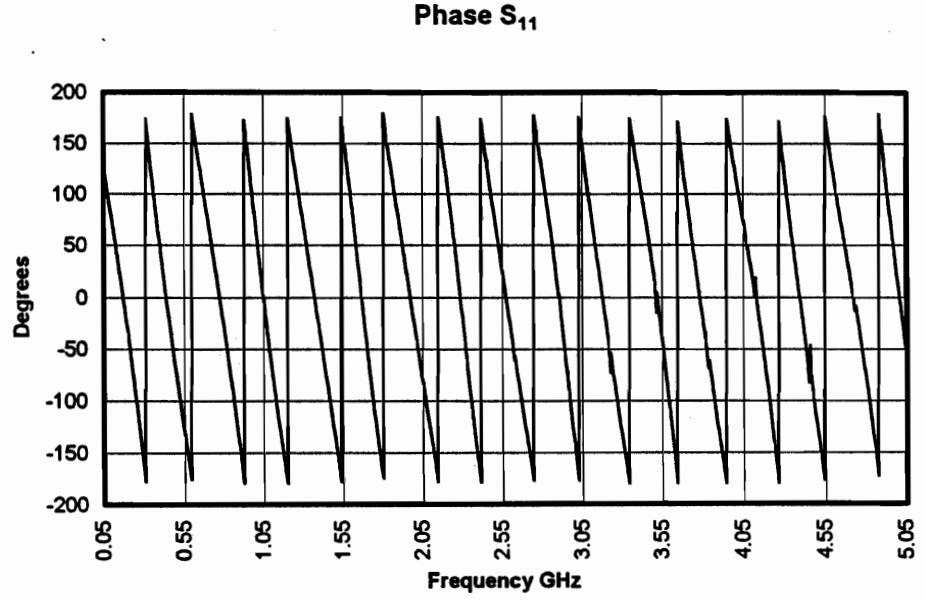

Figure 25b. Measured values of the phase of the complex reflection coefficient of Polypropylene.

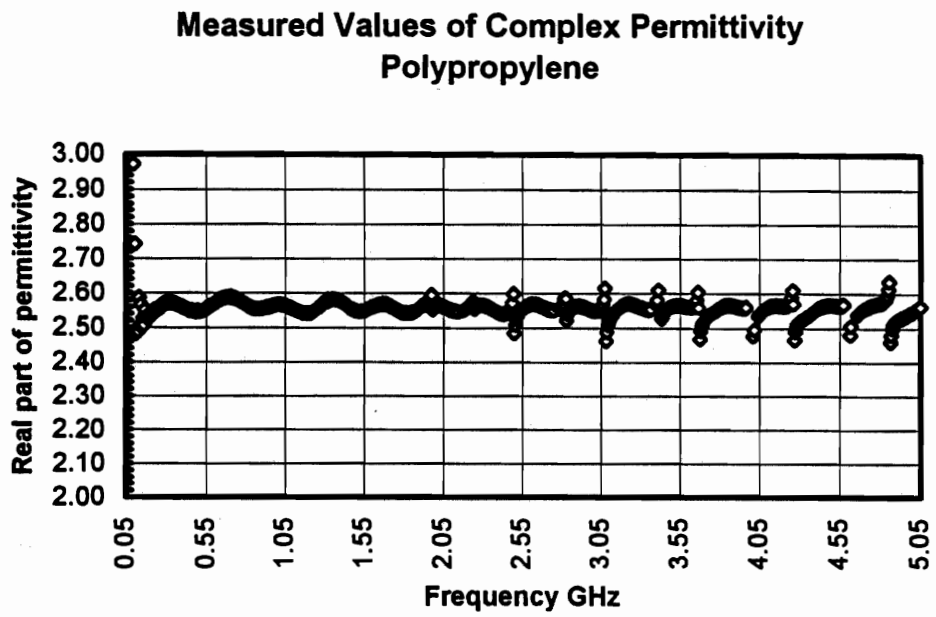

Figure 25c. **Measured values of the real part of the complex dielectric constant of Polypropylene.**

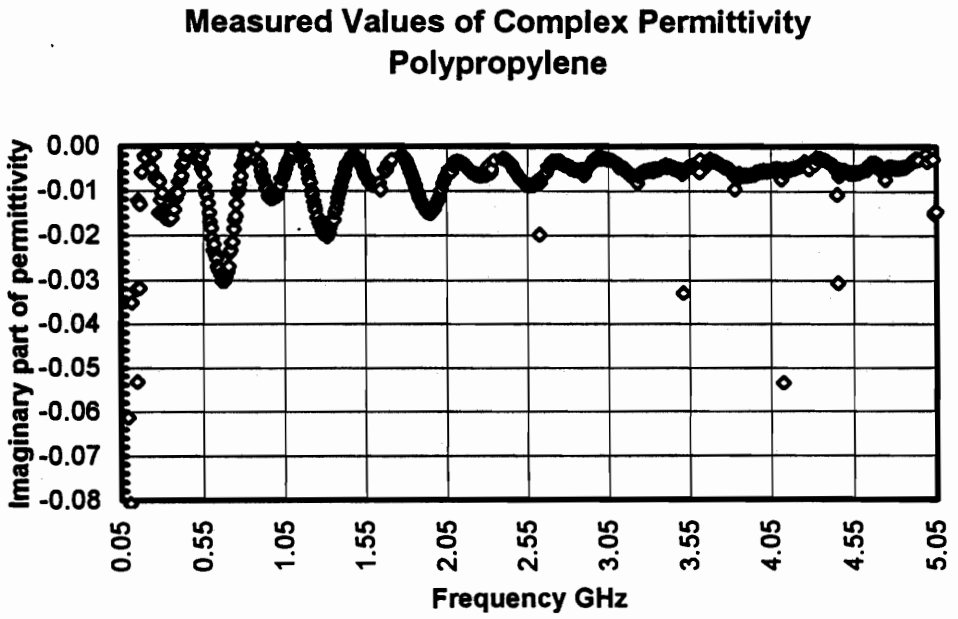

Figure 25d. **Measured values of the imaginary component of the complex dielectric constant of Polypropylene.**

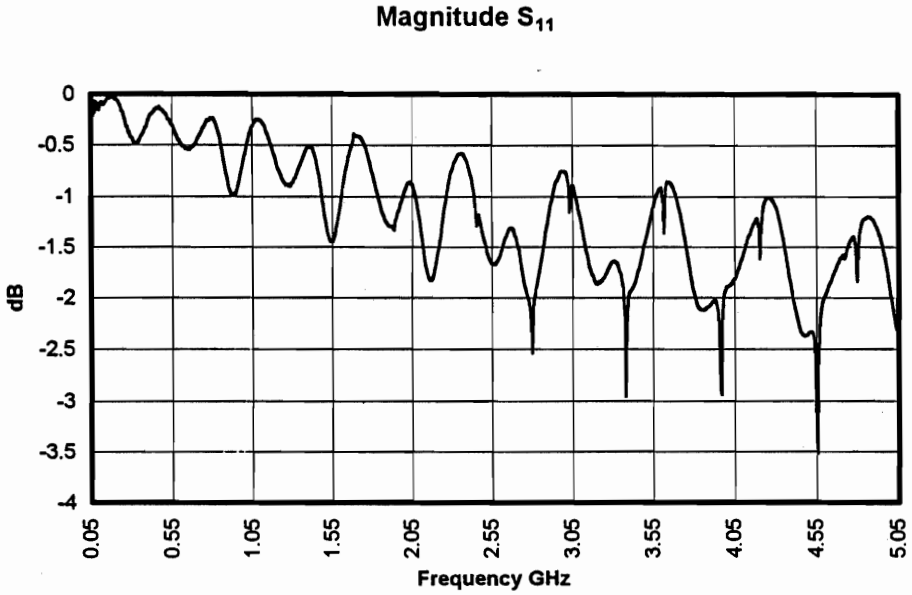

Figure 26a. Measured values of the magnitude of the complex reflection coefficient of Polyvinyl Chloride.

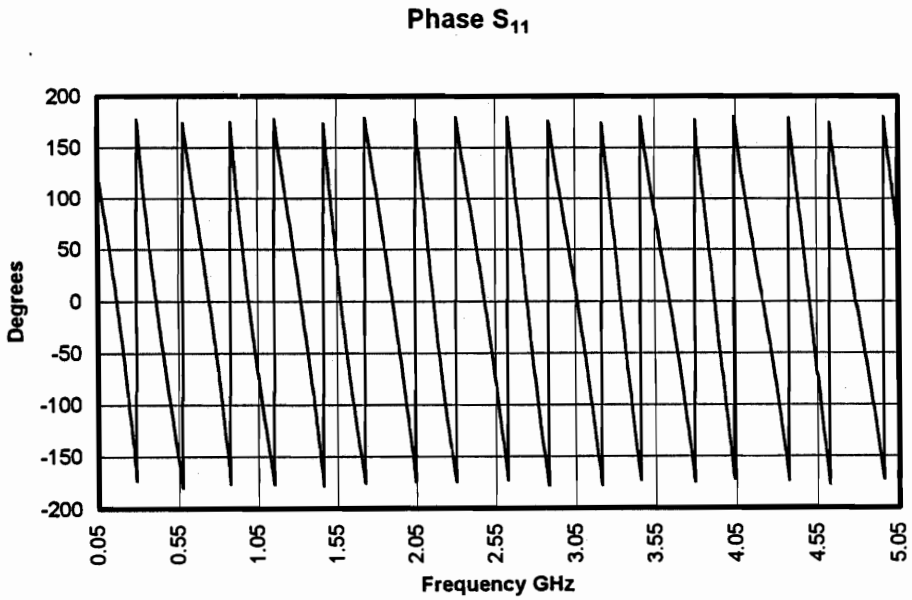

Figure 26b. Measured values of the phase of the complex reflection coefficient of Polyvinyl Chloride.

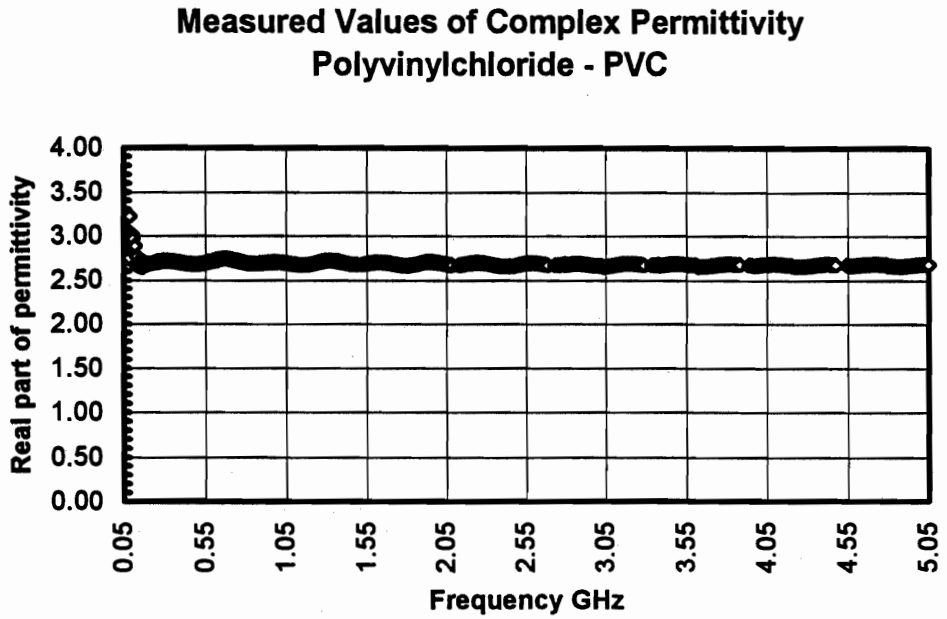

Figure 26c. **Measured values of the real part of the complex dielectric constant of Polyvinyl Chloride.**

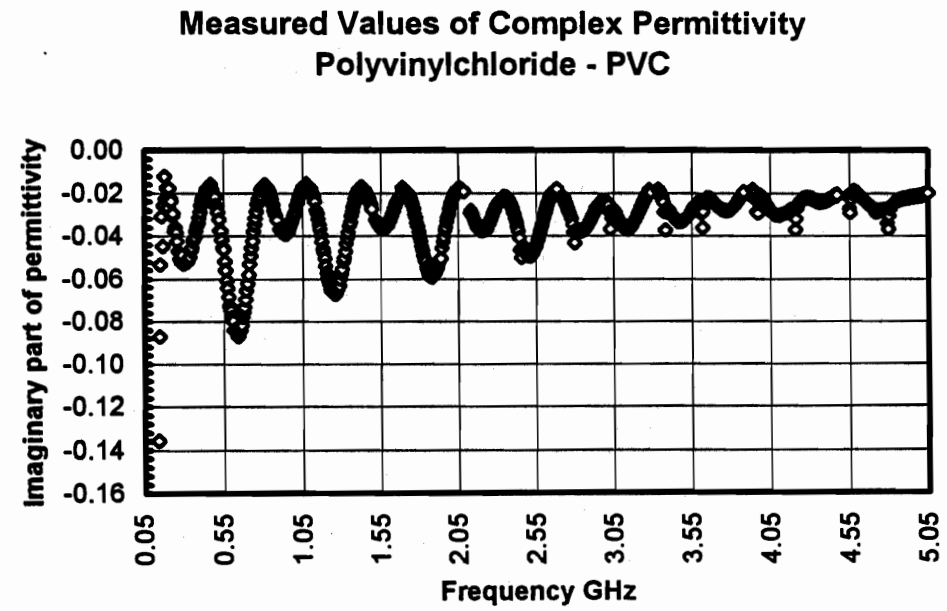

Figure 26d. **Measured values of the imaginary component of the complex dielectric constant of Polyvinyl Chloride.**

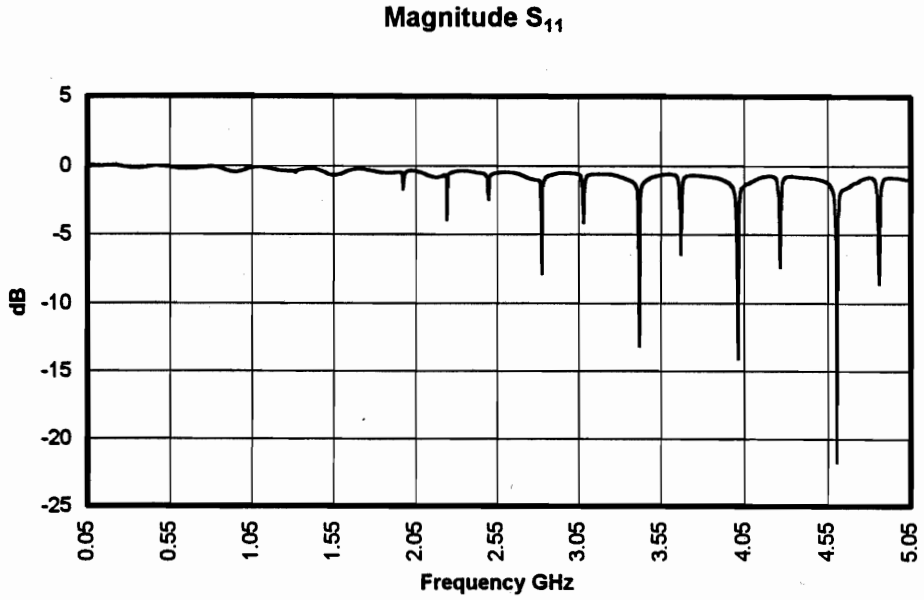

Figure 27a. Measured values of the magnitude of the complex reflection coefficient of Noryl.

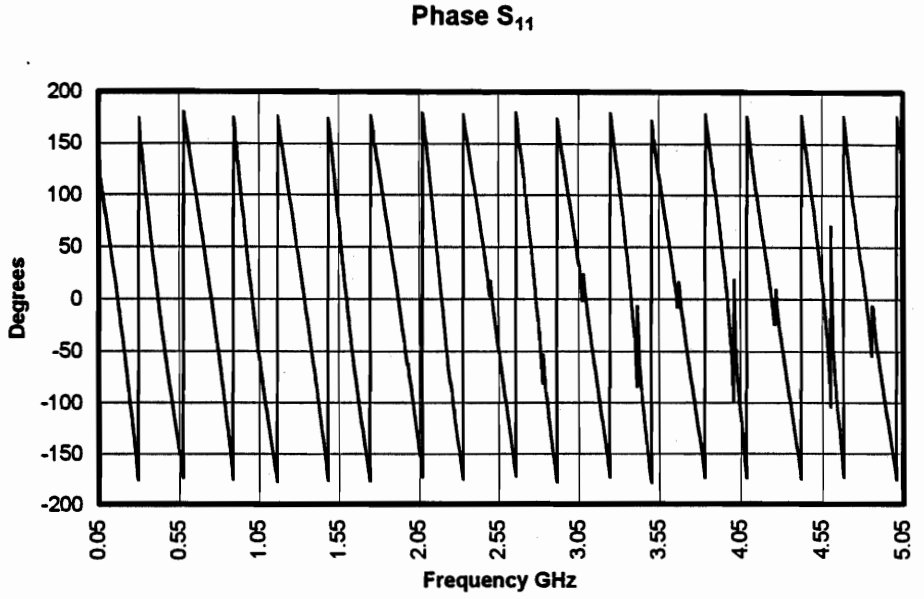

Figure 27b. Measured values of the phase of the complex reflection coefficient of Noryl.

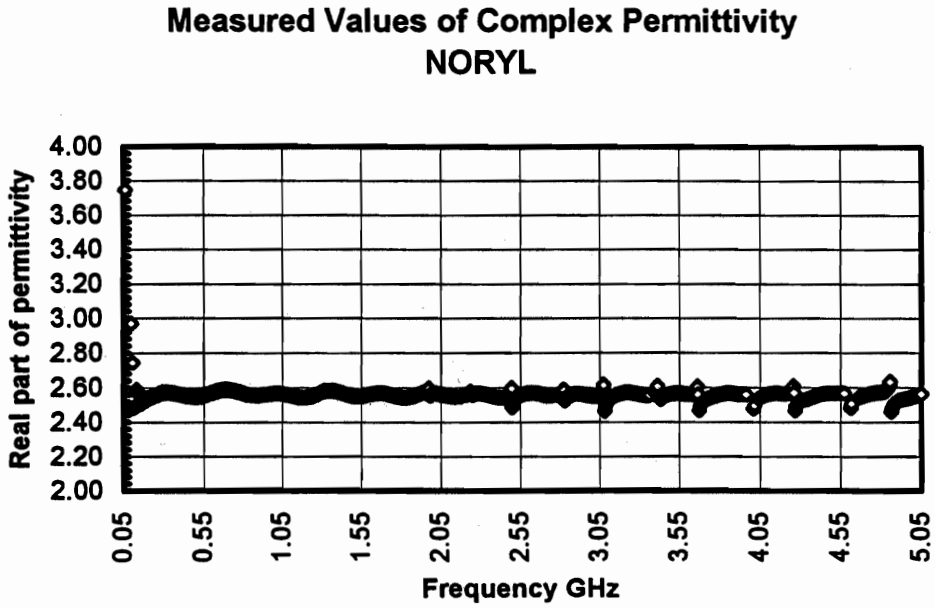

Figure 27c. **Measured values of the real part of the complex dielectric constant of Noryl.**

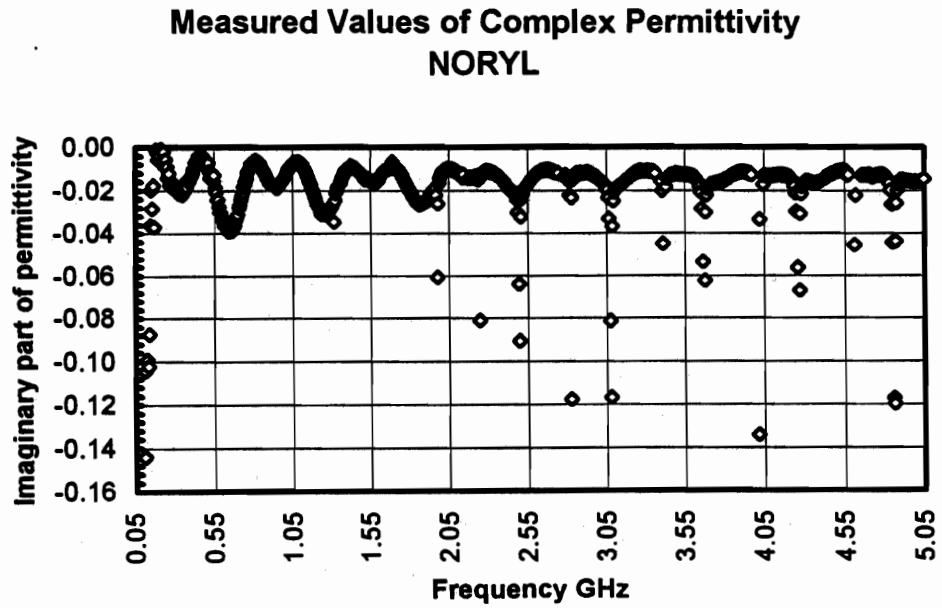

Figure 27d. **Measured values of the imaginary component of the complex dielectric constant of Noryl.**

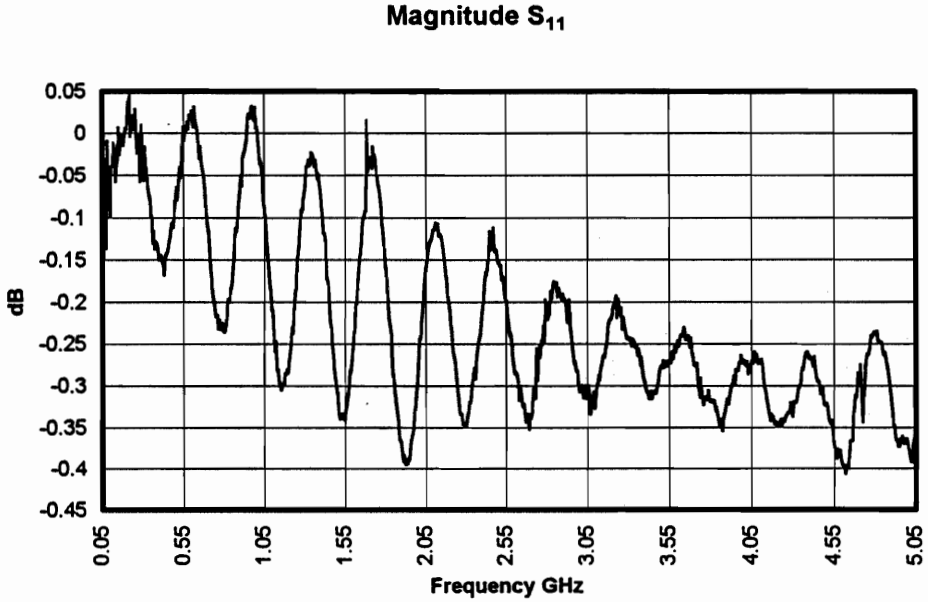

Figure 28a. Measured values of the magnitude of the complex reflection coefficient of Air (empty line).

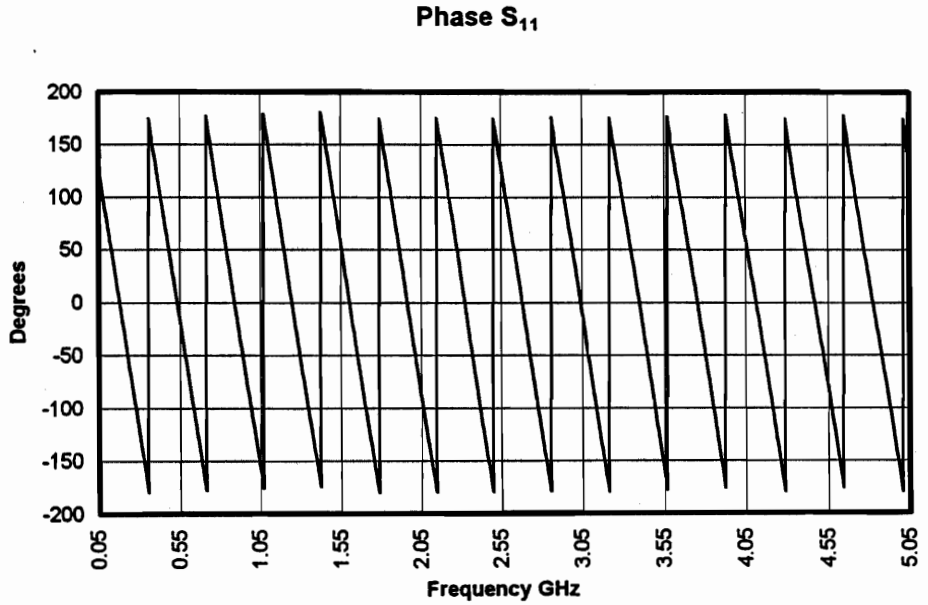

Figure 28b. Measured values of the phase of the complex reflection coefficient of Air (empty line).

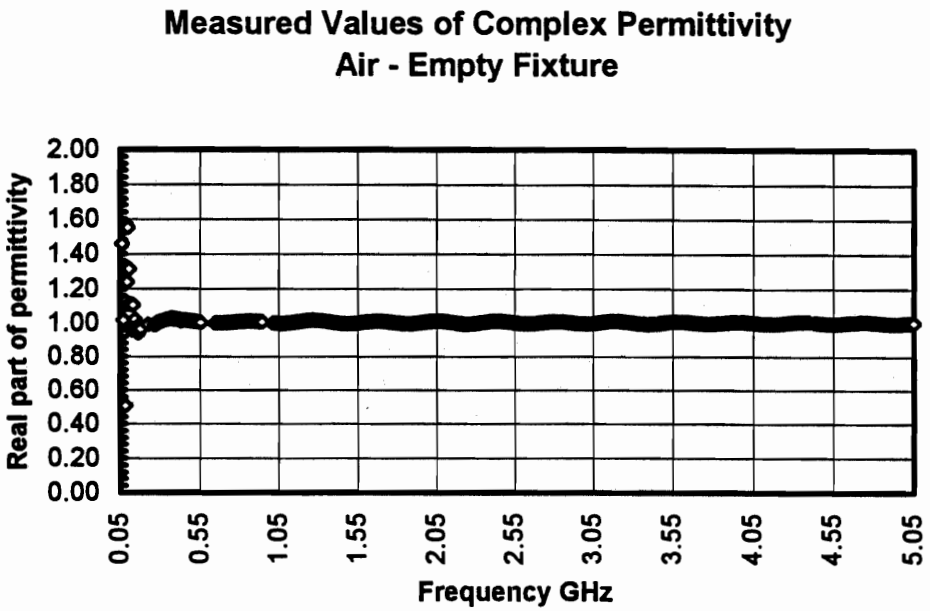

Figure 28c. **Measured values of the real part of the complex dielectric constant of Air (empty line).**

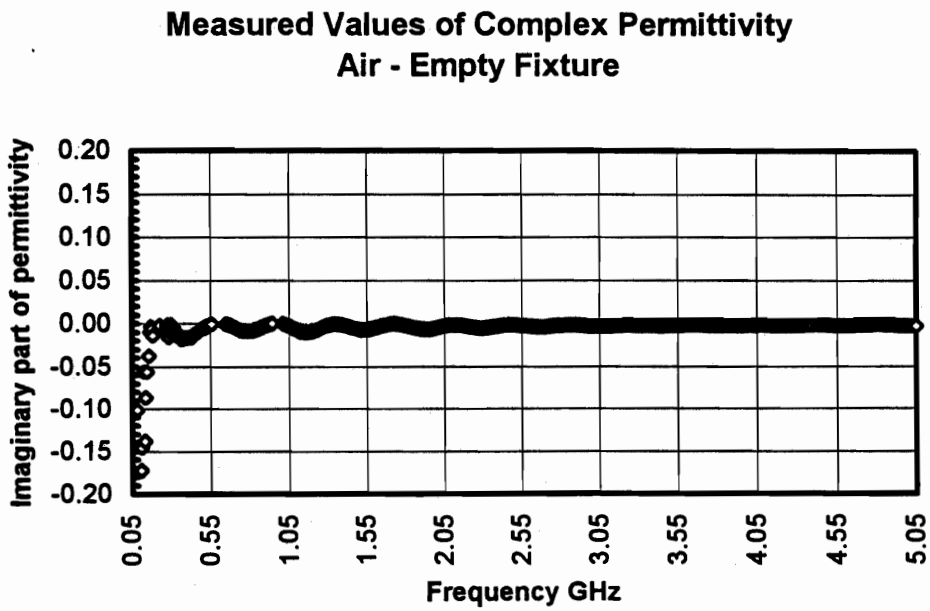

Figure 28d. **Measured values of the imaginary component of the complex dielectric constant of Air (empty line).**

VII. Frequency-Domain, In-Situ Measurement of Material Electromagnetic Properties

The techniques described in earlier sections all required the preparation of a material sample. Specifically, for these measurements the sample was fashioned into a hollow cylinder of a given length (up to 6 inches for the time domain measurements), with inner and outer diameters consistent with the dimensions of the coaxial test fixture. Sample preparation can be a time consuming and costly process, especially for materials like concrete. A measurement technique is needed which allows in-situ, or in-place, measurement of the dielectric properties of the material of interest. The theory and computations related to techniques that utilize coaxial probes which lie on the surface of the material have been describe in the literature [Refs. 14 - 26]. One such direct measurement technique is described below, and the preliminary results of these investigations is reported.

VII.1. Theory of Frequency Domain, In-Situ Measurements of the Dielectric Constant of Materials

Consider a coaxial line which opens through a ground plane. The geometry of Figure 29 depicts such a configuration. The admittance of the probe (Y_L) when in intimate contact with the material is a function of the material in the right half plane, it can be shown to be

$$Y_L = \frac{j2\omega\varepsilon_0\varepsilon_{r2}}{\left[\ln(b/a)\right]^2}\left\{I_1 - \frac{k^2}{2}I_2\right\} \qquad \text{(VII.1)}$$

where the constants I_1 and I_2 are functions of the probe geometry only. They have the following forms

$$I_1 = \int_a^b\int_a^b\int_0^\pi \frac{\cos\varphi'}{\left[\rho^2+\rho'^2-2\rho\rho'\cos\varphi'\right]^{1/2}}\, d\varphi'\, d\rho'\, d\rho, \qquad \text{(VII.2a)}$$

and

$$I_2 = \int_a^b\int_a^b\int_0^\pi \cos\varphi' \left[\rho^2+\rho'^2-2\rho\rho'\cos\varphi'\right]^{1/2}\, d\varphi'\, d\rho'\, d\rho. \qquad \text{(VII.2b)}$$

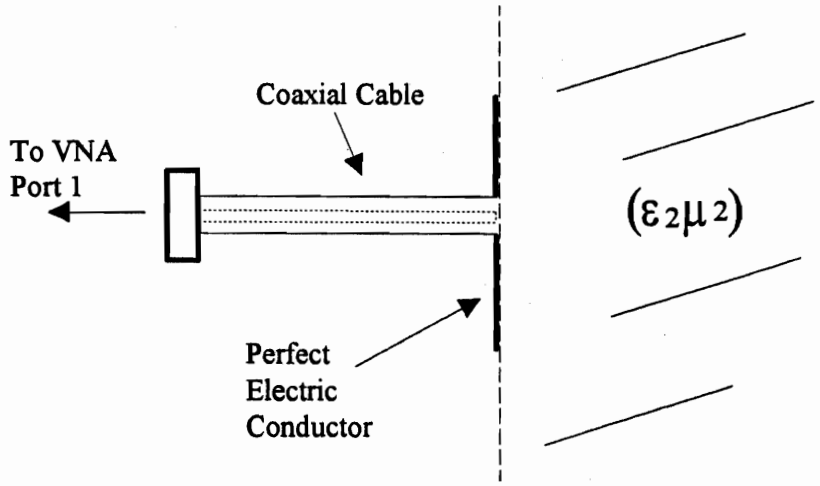

Figure 29. **A coaxial cable, with inner and outer radii *a* and *b*, opens through a ground plane (large compared with the outer diameter of the cable. The ground plan abuts the material in Region 2 characterized by material properties (ε_{r2},μ_0). Reflection coefficient (s_{11}) data is taken by a vector network analyzer.**

The dependence on the dielectric characteristic of the right half plane is shown in Eqn. VII.1. The idea is then to: (1) measure the input admittance of the coaxial probe; (2) compute the values of the constants I_1 and I_2 which are functions of the probe geometry; and (3) solve Eqn. VII.1 for the material dielectric constant. The measurement of the reflection coefficient is accomplished in the usual way, but the terms I_1 and I_2 must be numerically integrated.

The term I_2 is evaluated in a straight forward manner since its integrand is not singular anywhere within the domain of the integration. Unfortunately, this is not the case for I_1. The integrand has a $1/R$ - type singularity (but integrable), which can be removed using the properties of the Complete Elliptic Integral of the First Kind, but this introduces a log-type singularity. To completely remove the singular behavior of the integration, we must express I_1 as the following.

$$I_1 = \int_a^b\int_a^b\int_0^\pi \frac{\cos\varphi' - 1}{\left[\rho^2 + \rho'^2 - 2\rho\rho'\cos\varphi'\right]^{1/2}}\, d\varphi'\, d\rho'\, d\rho + 2\int_a^b\int_a^b \left\{ \frac{K(m)}{\rho+\rho'} + \frac{\ln\left|8\rho(\rho-\rho')\right|}{2\rho} \right\} d\rho'\, d\rho$$
$$+ \int_a^b \frac{1}{\rho}\left\{ (b-a) + \rho\ln\left|\frac{\rho-b}{\rho-a}\right| - b\ln\left|8\rho(\rho-b)\right| + a\ln\left|8\rho(\rho-a)\right| \right\} d\rho \qquad \text{(VII.3)}$$

where $K(m)$ is the Complete Elliptic Integral of the First Kind with modulus m. These equations have been coded, and the computations made for a number of common coaxial

geometries. These results are presented in Tables 7.1 and 7.2 below, and compared with results previously reported in the literature. The first and second columns give the probe dimensions (inner and outer diameter), the third column gives the values reported in the literature, the fourth column gives the result of the computation using adaptive Gaussian Quadrature, and the fifth column reports the value computed using the "removal of the singularity technique."

These results demonstrate the ability to correctly compute the numerical quantities required of this in-situ measurement procedure. The next section details the measurement and reduction of data taken using this procedure.

Table 7.1 **Comparison of the computed values of the constant I_1. Three values are reported for each geometry: (1) the value reported in the literature; (2) the value obtained using standard Gaussian Quadrature; and (3) the value obtained using "removal of the singularity (RTS)."**

a(cm)	b(cm)	I_1 (* 10^{-3}) : MISRA	I_1 (* 10^{-3}) : Gaussian Quad	I_1 (* 10^{-3}) : RTS
.3102	.7145	5.88293048	6.042628	6.048
.1520	.35	2.88055348	2.958763	2.962
.1124	.362	4.21373732	4.316997	4.323
.0824	.2655	3.09155881	3.167310	3.172
.0455	.1499	1.77531131	1.819128	1.823
.0255	.0838	0.99058927	1.015034	1.019

Table 7.2 **Comparison of the computed values of the constant I_2. Three values are reported for each geometry: (1) the value reported in the literature; (2) the value obtained using standard Gaussian Quadrature; and (3) the value obtained using "removal of the singularity" (RTS).**

a(cm)	b(cm)	I_2(* 10^{-9}) : MISRA	I_2(* 10^{-9}) : Gaussian Quad	I_2(* 10^{-9}) : RTS
.3102	.7145	-103.784060	-103.760769	-103.7591
.1520	.35	-12.194870	-12.192136	-12.19194
.1124	.362	-17.5606001	-17.561016	-17.56049
.0824	.2655	-6.92967372	-6.929838	-6.929628
.0455	.1499	-1.26188826	-1.261919	-1.26188
.0255	.0838	-.22018405	-.220189	-.2201831

Note: Underlined value is closer to that reported in the literature.

VII.1.1. Probe Fabrication, In-Situ Measurements and Results

A prototype probe was fabricated from 0.25 semi-rigid coaxial cable. This probe consisted of 0.25 in semi-rigid cable terminated on one end with an SMA connector and opening through and flush-mounted with a ground plane (approximately 4 inches square) on the other.

A material sample of polypropylene was prepared. This sample was a solid cylinder approximately 8 inches in diameter, and 12 inches long. This physical size insured that the probe ground plane was completely covered and thick enough that the sample appeared infinite in extent (a requirement of the analysis and reduction routines).

The input reflection coefficient of the probe was measured, at the plane of the connector on the rear of the probe, using a vector network analyzer. This value was rotated to the reference plane of the probe's ground plane as

$$s_{11}(\omega)\big|_{\substack{ground\\plane}} = s_{11}(\omega)\big|_{connector}\, e^{+j\omega\tau}, \qquad \text{(VII.4)}$$

where $\tau = 2.382$ ns is the measured round trip transit time from the probe's SMA connector to the ground plane. The measured values of the input reflection coefficient are graphed as shown in Figure 30.

The probe input admittance is determined though the relation

$$Y_L = Y_c \frac{1 + s_{11}(\omega)\big|_{\substack{ground\\plane}}}{1 - s_{11}(\omega)\big|_{\substack{ground\\plane}}}, \qquad \text{(VII.5)}$$

where $Y_c = 0.02$ S is the characteristic admittance of the probe's cable. These values where then substituted into an equation of the form

$$-\frac{j\omega^3\varepsilon_0^2}{\left[\ln(b/a)\right]^2} I_2\left(\varepsilon_{r2}\right)^2 + \frac{j2\omega\varepsilon_0}{\left[\ln(b/a)\right]^2} I_1\left(\varepsilon_{r2}\right) - Y_L = 0 \qquad \text{(VII.6)}$$

which is a quadratic equation in the unknown permittivity of the sample material. A complex quadratic solver was developed which accepts the measured values of the probe admittance, and yields values for the material permittivity of the sample material. These values are shown in the graph of Figure 31.

One notes the results given in Figure 31 are very unsatisfactory (see Figures 25c,d).

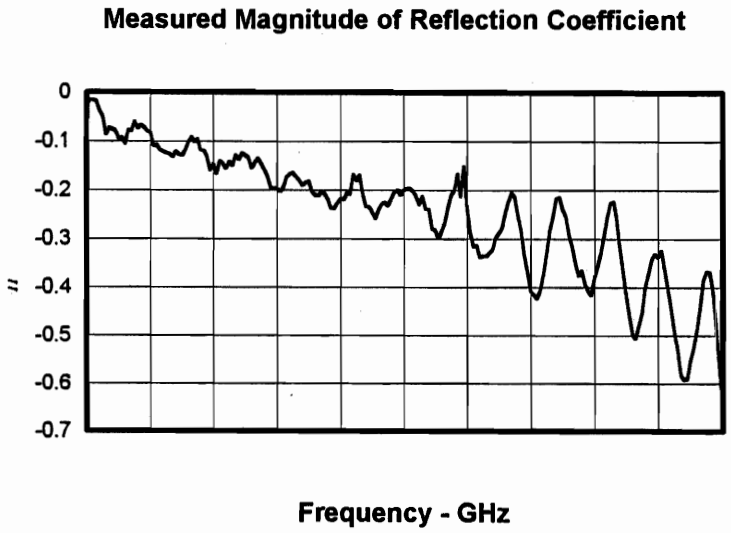

(a)

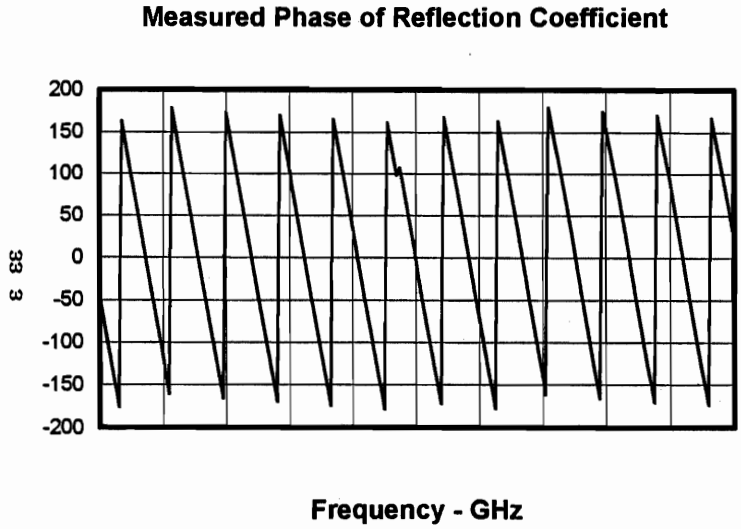

(b)

Figure 30. **The measured values of the input reflection coefficient of the coaxial probe: (a) magnitude; and (b) phase. These values have been transformed back to the ground plane.**

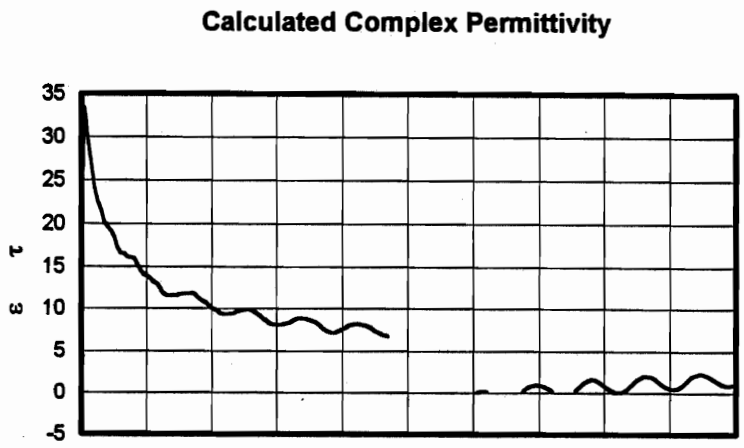

(a)

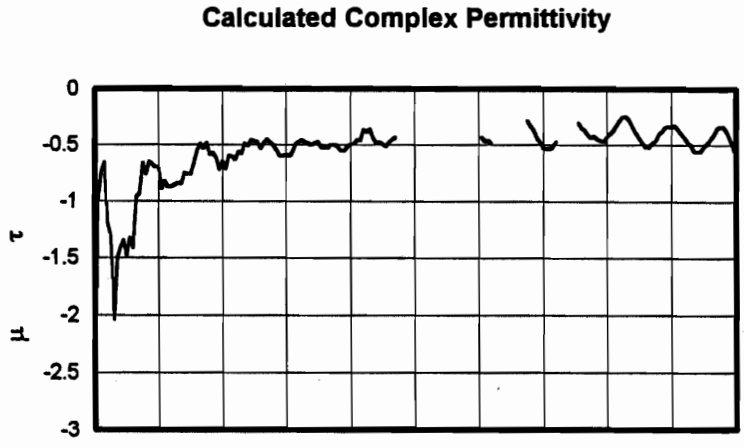

(b)

Figure 32. **The values of sample material (polypropylene) permittivity determined by the In-Situ measurement method described: (a) real component of the complex permittivity; and (b) imaginary component of the complex permittivity.**

Insight may be gained into the reason for these initial poor results with the following exercise. Assume a value for the dielectric constant of the sample material, we let this be $\varepsilon_{r2} = 2.2 - j0.002$. Next, we compute the expected theoretical values of the resulting input admittance (using Eqn. VII.1). The real and imaginary components of the resulting reflection coefficients are shown in Figures 32a and b, along with the actual measured values. One notes almost complete agreement in the values, at least up to the frequency point where the measured values exhibit a glitch (artifact of the instrument) in its response. Yet these same data sets yielded much different values for the material permittivity. For the fabricated (calculated) values, the quadratic equation solver returned the correct values for the permittivity. Yet the measured data set, when submitted to the same quadratic equation solver resulted in the disappointing values shown in Figure 31. This indicates an extreme sensitivity to the measured values, and may show that the required accuracy of the measurement exceeds that of our current measurement.

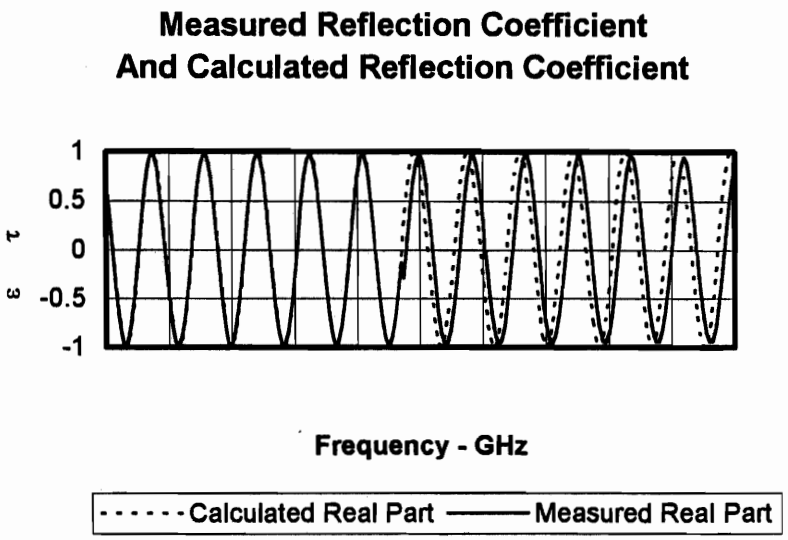

(a)

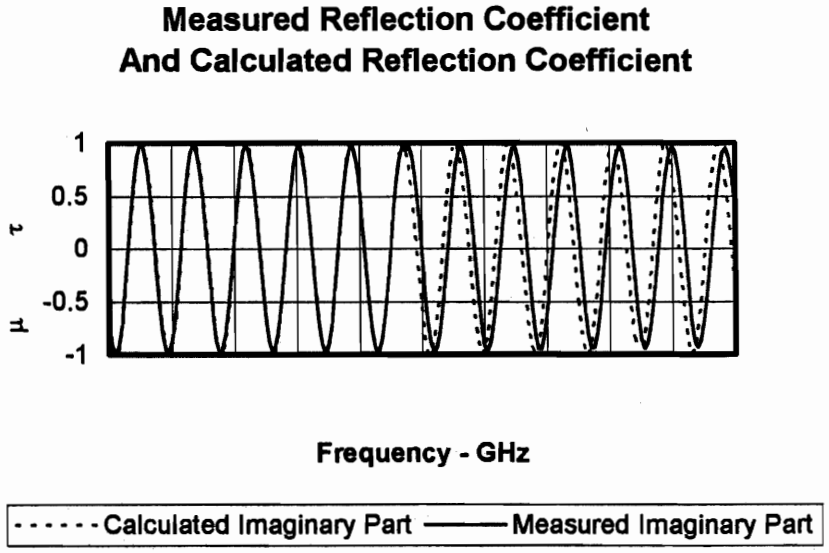

(b)

Figure 32. **The imaginary component of the complex values of the reflection coefficient of the probe: (a) real component of the complex values of the reflection coefficient; and (b) imaginary component of the complex values. Shown are both the actual measured values and the values determined by assuming the material (polypropylene) permittivity and solving for the resulting input reflection coefficient.**

VIII. References

1. Arthur von Hippel, Dielectrics and Waves, Second Edition, ISBN 0-89006-803-8, Artech House, Boston, 1995.

2. Arthur von Hippel, editor, Dielectric Materials and Applications, Second Edition, ISBN 0-89006-805-4, Artech House, Boston, 1995.

3. M. N. Afsar, J. R. Birch, and R. N. Clarke, edited by G. W. Chantry, "The measurement of the properties of materials," Proceedings of the IEEE, vol. 74, no. 1, pp. 183 - 199, January, 1986.

4. A. M. Nicolson and G. F. Ross, "Measurement of the intrinsic properties of materials by time-domain techniques," IEEE Trans. on Instr. and Meas., vol. IM-19, no. 4, pp. 377 - 382, November 1970.

5. A. M. Nicolson, P. G. Mitchell, R. M. Mara, and A. M. Auckenthaler, "Time domain measurement of microwave absorbers," Final Technical Report AFAL-TR-71-353, Air Force Avionics Laboratory, Air Force Systems Command, Wright-Patterson AFB, November 1971, DTIC No. AD-892162.

6. Roger F. Harrington, Time-Harmonic Electromagnetic Fields, ISBN 07-026745-6, McGraw-Hill, New York, 1961.

7. P. G. Lederer, "A transmission line method for the measurement of microwave permittivity and permeability," Memorandum 4450, Royal Signals and Radar Establishment, December 1990.

8. R. V. Churchill and J. W. Brown, Complex Variables and Applications, Fourth Edition, ISBN 0-07-010873-0, McGraw-Hill, New York, 1984.

9. P. A. Rizzi, Microwave Engineering - Passive Circuits, ISBN 0-13-586702-9, Prentice-Hall, Englewood Cliffs, NJ, 1988.

10. R. H. Cole, "Time-domain spectroscopy of dielectric materials," IEEE Trans. on Instr. and Meas., vol. IM-25, no. 4, pp. 371 - 375, December 1976.

11. R. H. Cole, "Evaluation of dielectric behavior by time-domain spectroscopy. I. Dielectric response by real time analysis, II. Complex Permittivity," J. of Phys. Chem., vol. 79, no. 14, pp. 1459 - 1474, 1975.

12. P. S. Neelakanta, Handbook of Electromagnetic Materials, pg. 42, ISBN 0-8493-2500-5, CRC Press, Boca Raton, FL, 1995.

13. K. Knoop, Infinite Sequences and Series, pg. 46, Dover Publications, Inc., New York, 1956.

14. Afsar, J. Birch and R. N. Clarke, "The measurement of the properties of materials," Proceedings of the IEEE, vol. 74, no. 1, pp 183 - 199, January 1986.

15. Katie F. Staebell and Devendra Misra, "An Experimental Technique for In Vivo Permittivity Measurement of Materials at Microwave Frequencies," IEEE Trans. Microwave Theory Tech., vol. 38, pp. 337-339, March 1990.

16. Devendra Misra, "A quasi-static analysis of open-ended coaxial lines," IEEE Trans MTT, vol. MTT-35, no. 10, pp. 925 - 928, October 1987.

17. Siqi Fan, K. Staebell, and Devendra Misra, "Static analysis of an open-ended coaxial line terminated by layered media," IEEE Trans Instrum. Meas., vol. 39, pp. 435 - 437, April 1990.

18. Devendra Misra, Mohinder Chabbra, Benjamin R. Epstein, Mark Mirotznik, and Kenneth R. Foster, "Noninvasisve Electrical Characterization of Materials at Microwave Frequencies Using and Open-Ended Coaxial Line: Test of an Improved Calibration Technique," IEEE Trans. Microwave Theory and Tech., vol. 38, pp. 8-14, Jan. 1990.

19. Hongming Zheng and Charles E. Smith, "Permittivity Measurements Using a Short Open-Ended Coaxial Line Probe," IEEE Microwave and Guided Wave Letters, vol. 1, pp. 337-339, Nov. 1991.

20. Gordon Kent, "Nondestructive Permittivity Measurement of Substrates," IEEE Trans Instrum. Meas., vol. 45, pp. 102-106, Feb. 1996.

21. Gregory B. Gajda and Stanislaw S. Stuchly, "Numerical Analysis of Open-Ended Coaxial Lines," IEEE Trans. Microwave Theory Tech., vol. MTT-31, pp. 384, May 1983.

22. Stuchly, M. Brady, Stanislaw S. Stuchly, and Gregory B. Gajda, "Equivalent circuit of an open-ended coaxial line in a lossy dielectric," IEEE Trans. Instrum. Meas., vol. IM-31, pp. 116 - 119, June 1982.

23. Juan R. Mosig, Jean-Claude E. Besson, Marianne Gex-Fabry, and Fred E. Gardiol, "Reflection of an Open-Ended Coaxial Line and Appliation to Nondestructive Measurement of Materials," IEEE Trans. Instrum. Meas., vol. IM-30, pp. 56-51, March 1981.

24. Teodoridis, T. Sphicopoulos, and Fred E. Gardiol, "The reflection from an Open-Ended Rectangular waveguide terminated by a layered dielectric medium," IEEE Trans. MTT., vol. MTT-33, no. 5, pp. 359-366, May 1985.

25. Li and K. Chen, "Determination of electromagnetic properties of materials using flanged open-ended coaxial probe - full wave analysis," IEEE Trans. Instrum. Meas., vol. 44, no. 1, pp. 19 - 27, Feb. 1995.

26. Nelson L. Buck, "Calibration of Dielectric Constant Probes Using Salt Solutions of Unknown Conductivity," IEEE Trans. Instrum. Meas., vol. 45, pp. 84-88, Feb. 1996.

27. B. K. Singaraju, D. V. Giri, and C. E. Baum, "Further Developments in the Application of Contour Integration to the Zeros of Analytical Functions and Relevant Computer Programs," Math Note (MaN) 42, pp. 52-61, March 1976, Air Force Weapons Laboratory.